Thermal Stability and Corrosivity of Bio-oil Blends for Co-processing Applications

by

Haoxiang Wang

A thesis submitted in partial fulfillment of the requirements for the degree of

Doctor of Philosophy

in

Materials Engineering

Department of Chemical and Materials Engineering
University of Alberta

Abstract

Bio-oil (BO) is a promising and renewable energy source that could alleviate dependence on fossil fuels, but its direct use faces challenges due to low thermal stability and high corrosiveness. Co-processing BO with vacuum gas oil (VGO) in existing refineries offers a solution without requiring additional capital investment. However, the unique characteristics of BO, such as changes during storage and transportation, corrosion risks, and low miscibility with petroleum intermediates, necessitate thorough evaluation before integration.

This thesis investigates three crucial aspects of BO derived from pinewood through fast pyrolysis: thermal stability, corrosiveness to steel, and miscibility with VGO at temperatures up to 80 °C. Firstly, accelerated aging experiments with methanol addition revealed a positive correlation between aging rate and temperature, highlighting the stabilizing effect of methanol. Later, corrosion evaluations demonstrated significant corrosion in BO for carbon steel, while stainless steel exhibited minimal corrosion. Adapted electrochemical methods effectively assessed steel corrosion in the low-conductivity BO environment. Gas chromatography analysis identified gases generated during BO aging and steel corrosion, unveiling comprehensive mechanisms behind corrosion processes and BO internal reactions. The study proposed mechanisms explaining the interactions between BO and steel. In addition, to enhance miscibility with VGO, surfactants were utilized, resulting in stable BO/VGO emulsions at 50 °C with a 2 wt% surfactant addition.

Overall, the findings presented in this thesis contribute significantly to BO co-processing operations by enhancing understanding of BO characteristics, providing advanced electrochemical techniques for corrosion assessments, proposing mechanisms for BO-steel interactions, and

optimizing blending processes with BO/VGO emulsions. Insights on optimal preheating temperature and materials compatibility offer valuable guidance for efficient, reliable, and safe BO co-processing.

Preface

Chapter 1 includes partial contents from the publication of X. Han, **H. Wang**, Y. Zeng, J. Liu. "Advancing the Application of Bio-oils by Co-Processing with Petroleum Intermediates: A Review." *Energy Conversion and Management: X*. 10 (2020) 100069. **H. Wang** served as the second author and contributed equally to the first author. The contents included in this chapter were originally drafted by **H. Wang** and edited by other co-authors.

Chapter 3 has been published as **H. Wang**, A. Gross, J. Liu. "Influence of Methanol Addition on Bio-oil Thermal Stability and Corrosivity." *Chemical Engineering Journal*. 433 (2021) 133692.

Chapter 4 has been published as **H. Wang**, J. Liu. "Electrochemical Corrosion Study of Carbon Steel in Bio-oil Environments." *Renewable Energy*. 221 (2024) 119823.

Chapter 5 has been submitted for publication as **H. Wang**, J. Liu. "Corrosion-Induced Changes in Bio-oil Aging: A Gas Chromatography Exploration"

Chapter 6 has been published as **H. Wang**, J. Liu. "Emulsification and Corrosivity Study of Bio-oil and Vacuum Gas Oil Mixtures with A Novel Surfactant System." *Fuel*. 333 (2023) 126460.

H. Wang served as the first author of the publications **from Chapter 3 to Chapter 6**. Dr. J. Liu extensively helped with all aspects of these research works.

Dedication

I feel lucky to have the opportunity to pursue this degree.

I feel lucky to be engaged in a research project aimed at making a meaningful contribution to the environment.

I feel helpless every time I hear about people who suffer from wars, suffer from hunger, and suffer in pain.

My heart is with them, and I wish this world would be a better place for them.

This thesis is dedicated to them.

Acknowledgements

I would like to express my deepest appreciation to my supervisor, Dr. Jing Liu, who involved me in this amazing research project, let me explore my research interests freely, and always treated me kindly. Her consistent trust, support, and guidance helped me to complete this degree.

I am extremely grateful to my supervisory committees, Dr. Weixing Chen and Dr. Anthony Yeung, who provided me with so much advice and help for my research. Thanks should also go to my examination committees, Dr. Charles Chunbao Xu, Dr. Amit Kumar, and Dr. Xuehua Zhang, for their generous help and advice.

I would like to thank the former and current group members in Dr. Jing Liu's lab for their help, companionship, and kind input for my research. I am also grateful to my former supervisors, Dr. Zhehui Jin and Dr. Na Jia, who inspired me to do research.

I could not have undertaken this journey without the support and love of my dearest friends and family. Thank you for always being by my side and believing in me. Special thanks to my puppy, Cola, who greets me at the door every day and makes me his whole world.

Table of Contents

List of Tables

List of Figures

List of Symbols

A	Surface area
Angle_cal	Calculated phase angle
Angle_msd	Measured phase angle
β_a	Anodic Tafel slope
β_c	Cathodic Tafel slope
CR_{EM}	Corrosion rate calculated from electrochemical measurement
CR_{IE}	Corrosion rate calculated from immersion experiment
EW	Equivalent weight
h	Hours
i_{corr}	Corrosion current density
L	Inductance due to chelation
Δm_{loss}	Mass loss
mm/y	Millimeter per year
ρ	Density
Q	Capacitance modelled by a constant phase element
R_2	Resistance against corrosion reactions
R_{ct}	Charge transfer resistance
R_f	Resistance associated with the chelate complex exchanging layer
R_p	Polarization resistance
R_s	Solution resistance
T	Temperature

χ^2 Chi-square

$|Z|$ Overall impedance

$|Z|\_cal$ Calculated impedance

Z_{im} Imaginary impedance

$|Z|\_msd$ Measured impedance

List of Abbreviations

AC	Acetic acid
BE	Binding energy
BO	Bio-oil
CE	Counter electrode
CR	Corrosion rate
CS	Carbon steel
CFS	Clean Fuel Standard
CI	Carbon intensity
CPE	Constant phase element
DI	Deionized
ECM	Equivalent circuit model
EDL	Electrical double layer
EDS	Energy-dispersive X-ray spectroscopy
EIS	Electrochemical impedance spectroscopy
EM	Electrochemical measurement
FCC	Fluid catalytic cracking
FID	Flame ionized detector
FT-IR	Fourier-transform infrared spectroscopy
GC	Gas chromatography
GC–MS	Gas chromatography–mass spectrometry
GHG	Greenhouse gas

HDO	Hydrodeoxygenation
HLB	Hydrophilic-lipophilic balance
HTL	Hydrothermal liquefaction
IE	Immersion experiment
KWHT	Kruskal-Wallis H Test
MOC	Material of construction
MWUT	Mann-Whitney U Test
LPR	Linear polarization resistance
ME	Methanol
OCP	Open circuit potential
OM	Optical micrograph
PDP	Potentiodynamic polarization
RE	Reference electrode
SEM	Scanning electron microscopy
SP	Span 80
SS	Stainless steel
ST	Mixture of Span 80 and Tween 80
STM	Mixture of Span 80, Tween 80, and methanol
TAN	Total acid number
TCD	Thermal conductivity detector
TGA	Thermogravimetric analysis
TW	Tween 80
VGO	Vacuum gas oil

WE	Working electrode
WS	Working sense
XPS	X-ray photoelectron spectroscopy
XRD	X-ray diffraction

Chapter 1. Introduction

1.1. Overview of Bio-oil (BO)

Sustainable and renewable energy resources are getting more attention due to the gradual depletion of fossil fuels, the deterioration of the environment, and serious climate change [1, 2]. Societies around the world are on the verge of a profound and urgently necessary transformation in the way they produce and use energy. Shifting society's dependence away from petroleum to renewable resources (such as biomass) is generally viewed as a significant contributor to the development of a sustainable industrial society and effective management of greenhouse gas (GHG) emissions. Biomass utilization offers an optimum solution to waste management. It is estimated that the biomass waste generated from agricultural and forestry industries is in the order of 140 Gt on an annual basis [3, 4]. Traditional handling of biomass residues such as burning in the open-air leads to severe environmental pollution. These agricultural and forestry wastes can be used as low-cost biomass sources for energy generation while providing solutions for biomass waste management [5].

Raw biomass materials, such as wood and forestry residues, crops and crop residues, marine products and bio-wastes, are abundant renewable energy sources that can be converted to a liquid product commonly referred to as bio-oil (BO) [6-9]. There are two important thermochemical conversion methods including fast pyrolysis and hydrothermal liquefaction (HTL) to produce BOs from biomass [10, 11]. Fast pyrolysis oil is collected from vapor condensation (vapor residence time 0.5–5 s) after rapidly heating (heating rate > 1000 °C/min) small (< 5 mm) dried (< 10% water) biomass particles under anaerobic conditions to a temperature of about 500 °C at atmospheric pressure [12]. During the fast pyrolysis process, large molecules of biomass feedstock

break into chemical "building blocks" followed by reformation [13]. Approximately 60–75 wt% of biomass is converted to liquid BO during the fast pyrolysis process. By-products such as combustible solid char (15–25 wt%) and non-condensable gaseous (10–20 wt%) are mainly used for energy input to the system. In comparison, HTL is commonly used for converting high-water content feedstock like microalgae or wastewater sludge into BOs in water or water-containing solvents at mild temperatures (250–375 °C) and elevated pressures (4–22 MPa) [14]. Since the production of HTL BO is still under development and has not been commercialized, BO produced by fast pyrolysis will be the target BO for this thesis.

BOs are carbon-neutral since they release the same amount of carbon dioxide when combusted as biomass absorbs in growing [15]. Consequently, the application of BO can effectively mitigate the burden of GHG emissions arising from fossil fuel combustion [16]. In addition, since BOs contain a relatively low level of sulfur, they have minimal contribution to sulfur-related environmental problems (e.g., acid rain) [17]. Meanwhile, government policies regarding the development of biomass-derived renewable energy encourage refineries to expand their BO production. The European Union set a goal of increasing the percentage of renewable energy in total energy consumption to 20%, and the BO incorporation in transportation fuels to 10% by 2020 [18, 19]. In Canada, the government of British Columbia implemented a low-carbon fuel standard to reduce the provincial carbon intensity (CI) of fuels. The set CI limits for Diesel Class Fuel and Gasoline Class Fuel decreased from 86 CO_2e/MJ and 80 CO_2e/MJ, respectively, in 2020 to 76 CO_2e/MJ and 70 CO_2e/MJ, respectively, in 2030 [20]. In the US, California's low carbon fuel standard aims to reduce 20% CI by 2030 through enhanced consumption of bio-renewable fuels [21]. Overall, BO will foreseeably play a significant role in the future renewable energy supply.

1.2. Bio-oil (BO) Characterizations

1.2.1. Bio-oil (BO) Physical/Chemical Properties

Crude BOs are dark and viscous fluids consisting of over 400 components, and their compositions vary by feedstock and conversion processes [12, 22]. The polarities of compounds in BO are quite different. High-polar compounds (e.g., water), non-polar compounds (e.g., hexane), and less-polar compounds (e.g., ester) in BO are not completely mutually soluble. In general, most BOs visually appear as homogeneous liquids [23]. Microscopically, BO is a complex colloidal system consisting of solid particles and structured materials (agglomerates) dispersed in a continuous BO medium. **Table 1.1** compares some properties of BO and vacuum gas oil (VGO), a petroleum intermediate commonly used as a feedstock for the fluid catalytic cracking (FCC) process. Due to the existence of many polar compounds, BOs are not miscible with non-polar petroleum fuels.

Table 1.1. Properties of BOs and VGO [17].

Oil property	BO	VGO
Water content, wt%	15-30	0.1-0.6
pH	2-3.2	-
Specific gravity	1.1-1.3	0.85-0.94
Viscosity @ 50°C, cP	40-100	180
Calorific value, MJ/kg	16-23.6	40
Elemental composition, wt%		
C	54-58	85-87.5
H	5.5-7.0	11-12.4
O	35-40	0.3-1
N	0-0.4	0.04-0.3
S	0-0.05	0.08-2.02
Ash	0-0.85	0.1

1.2.2. Bio-oil (BO) Aging and Thermal Stability

BOs are not as stable as conventional petroleum fuels as they contain plenty of oxygenated

compounds and low-boiling volatiles. As a liquid product by rapid cooling or quenching from high temperatures, BOs are not at thermodynamic equilibrium [24]. During storage, the chemical composition of BO shifts toward thermodynamic equilibrium resulting in poor storage stability. During storage at the ambient temperature, BOs react with oxygen resulting in BO polymerization and consequently heavy compounds sedimentation. The main chemical reactions include esterification and etherification between components having hydroxyl, carbonyl, and carboxyl groups, and polymerization of double-bonded constituents [25]. These reactions cause a decline in volatility, and slow increases in viscosity, molecular weight, and water content of BO. As this process progresses with time, it is referred to as aging. At elevated temperatures, accelerated aging reactions take place that greatly alter the properties of BO such as a rapid increase in viscosity and phase separation [26, 27].

BOs contain a large amount of water (15–30 wt%) coming from free water in biomass and condensation reactions during production [28]. Water content builds up during aging by undergoing chemical reactions such as esterification that turns alcohols and organic acids into esters and water [24]. High water content in BO is associated with its unfavorable lower heating value compared to fossil fuels [26]. Studies have found that phase separation would occur when the water content in BO exceeds 30 wt% [29, 30]. BOs can be separated into water-soluble and water-insoluble fractions via centrifugation [23]. The upper layer has lower water, solid and ash contents, but contains more methanol-insoluble materials with higher viscosity and calorific value. The bottom layer acts oppositely with overall physicochemical properties similar to those of the whole BO. Although the increase in water content partially offsets viscosity growth, the formation of high-molecular-mass materials is more detrimental to fuel performance [26].

BOs contain 8–10 wt% organic acids such as acetic, formic, glycolic and propionic acids and have a pH value of 2–3 and a total acid number (TAN) of 50–100 mg KOH/g [25, 31]. The TAN is defined as the amount of potassium hydroxide (KOH, in mg) required to neutralize the acids in 1 g of BO. Studies have shown that the viscosity of BO was negatively correlated with its water content [32], yet was not correlated with the TAN and pH value [33]. Oasmaa et al. [31] reported that there was no correlation between BO acidity and aging time. Meanwhile, crude BOs contain less than 1 wt% solid consisting of coke, char and impurities such as dust and ash [34]. Solid particles have negative influences on the storage stability and combustion performance of crude BOs [29]. During storage, char particles tend to agglomerate forming large particles. Besides, char particles can act as catalysts to accelerate BO aging. Solid particles can adsorb pyrolysis lignin to form gummy tars resulting in the plugging of feed lines. Besides, they are also responsible for the erosion of the fuel injection systems. Ash, as an inorganic part of solids such as metals, is contained in BOs ranging from 0.1–0.4 wt% depending on biomass feedstock [25]. BOs derived from straw and grasses contain more alkali metals than wood-derived BOs. Alkali metals may form molten salts in the combustion environment to corrode gas turbines.

1.2.3. Stabilizing Bio-oil (BO) by Adding Solvents

It has been approved that blending a small portion of solvents (up to 20 wt%) such as methanol, acetone, and ethyl acetate into BO led to promising results in reducing the aging rate (i.e., viscosity increase rate) of BO [35, 36]. In recent years, composite additives have been investigated to improve the stability of BOs [37-40]. However, these composite additives are expensive and contain nitrogen or sulfur that produce undesirable gases during BO upgrading and combustion. Alcohols, as additives, have great potential considering their accessibility, pricing, and toxicity to

the environment, and can also be produced from biomass.

Several mechanisms have been proposed to explain how adding methanol reduced the BO aging rate [35]. Firstly, adding alcohol can slow the BO internal reactions by physical dilution. Besides, monofunctional alcohols (e.g., methanol) can react with acidic oligomers to form oligomeric esters which can further react with alcohols to form lower-molecular-weight methyl esters through transesterification reactions. These chain termination reactions of oligomers slow down the aging rate of BO by making fewer reactive sites available for polymerization reactions. Alcohols also consume aldehyde groups to produce acetals, which reduces their availability for polymerization reactions.

Diebold and Czernik [35] performed accelerated aging tests of BO at 90 °C to examine the effect of adding additives such as methanol, ethanol, and acetone on BO aging. They concluded that methanol (10 wt%) was the most adequate stabilizer where the BO/methanol blend was maintained as a single phase after 96 h exposure to 90 °C. Oasmaa et al. [41] conducted accelerated aging tests with BO/alcohols (e.g., methanol, ethanol, and isopropanol) mixtures at 80 °C for up to 24 h. They found that adding alcohol instantly improved the homogeneity, decreased the viscosity and density, lowered the flash point, and increased the heating value of BO. During storage, adding alcohols slowed the viscosity and molecular mass increasing rates of BO. They also concluded that methanol had the best performance in reducing the BO aging rate. Mei et al. [42] investigated the storage stability of pinewood-derived BO with a methanol addition of 3–15 wt% at 25 °C for 35 days. They found that as the methanol concentration increased, BO viscosity and water content increasing rates declined. Besides, the pH value of BO slightly increased during storage when the

6

methanol content was above 6 wt%. Ding et al. [43] developed modified mixing rules to predict the viscosity of BO/alcohol blends. They suggested that adding 20 wt% methanol was the most optimal strategy for reducing the aging rate of BO while being economically feasible.

1.3. Corrosion Challenges of Structural Alloys in Bio-oil (BO) Environments

1.3.1. Immersion Experiments

Although BOs have good combustion characteristics, they are compositionally distinct from petroleum fuels. One critical issue of using BOs is their high acidity. Therefore, materials in contact with BOs must be tested for compatibility. The corrosivity of BOs remains uncertain and has attracted lots of research studies as follows.

Aubin and Roy [44] studied the corrosion of wood-derived pyrolysis BOs on carbon steel and stainless steels AISI 304 and AISI 316 at 25 and 45 °C. They reported that stainless steels were corrosion-resistant to BOs, yet carbon steel corroded severely in BOs. Oasmaa et al. [32] tested the corrosion behaviors of various metal alloys in hardwood-derived pyrolysis BO at up to 80 °C for 6 weeks. The results showed that carbon steel AISI 01 corroded obviously at 60 °C. It was found that the performance of AISI 316 was better than AISI 304, which was attributed to a small amount of molybdenum existing in AISI 316 steel making it more resistant to corrosion in non-oxidizing acids, stress corrosion, and localized corrosion induced by aggressive halogens.

Darmstadt et al. [45] studied the corrosion of stainless steel AISI 316 by softwood bark residue–derived BO at 80 °C. The BO was artificially separated into two layers: a water-soluble layer (bottom layer, 82.7 wt%) and a water-insoluble layer (top layer 17.3 wt%) [46]. Corrosion tests

7

were conducted with whole BO and the upper and the bottom layers of BO in closed glass containers for 12–168 h. The results showed that AISI 316 was corrosion-resistant to BO due to chromium species migrating from the bulk toward the surface of the steel forming a protective chromium oxide layer after iron species being leached from the metal surface.

Keiser et al. [47, 48] studied the corrosion of various metal alloys (carbon steel, 2.25Cr-1Mo steel, and AISI stainless steels 304L, 316 L, and 409) by pyrolysis BO at 50 °C for a total of 1000 h. Two types of metallic specimens including flat coupons and U-bend samples were used for the experiments. Specimens were immersed in liquid BO and placed in the vapor space above the BO. Argon was used to isolate the system from the surrounding environment. The results showed that there were significant weight losses in carbon steel and 2.25Cr-1Mo steel, and their corrosion in the vapor phase was nonnegligible but generally less than that in the liquid phase. The calculated corrosion rates cannot be tolerated for structural materials to last for years. Besides, corrosion forms were different for the vapor phase (pitting) and the liquid phase (uniform attack) [49]. Hydrated iron formate was identified by X-ray diffraction as a corrosion product on the surface. There was minimal weight loss shown on the stainless steel specimens. For U-bend samples, cracks were found in alloys with low chromium content. Steels that have higher chromium content were found more corrosion-resistant to BOs [49].

1.3.2. Electrochemical Measurements

Electrochemical techniques have been widely used to study corrosion behaviors of metals in a variety of media. Compared to immersion experiments, electrochemical measurements are simpler, faster, and less expensive [50]. Linear polarization resistance (LPR), potentiodynamic

polarization (PDP), and electrochemical impedance spectroscopy (EIS) are commonly used as electrochemical approaches. Polarization measurements are conducted by varying the potential of the working electrode and monitoring the corresponding current change [51]. The polarization resistance (R_p) is defined as the slope of the potential–current density curve. Low R_p values are associated with higher corrosion current density and higher corrosion rates. EIS measures the impedance of a system dependent on the frequency of the alternating current supply to obtain information on corrosion processes occurring on the electrode surface [52, 53]. An equivalent circuit model is often used to fit the Nyquist and Bode plots obtained from EIS measurements to determine the charge transfer resistance (R_{ct}) of metal samples, which is inversely proportional to their corrosion rates [54].

Jun et al. [55, 56] investigated the corrosivity of organic constituents such as lactobionic acid, formic acid, and catechol for 2.25Cr-1Mo and 9Cr-1Mo steel steels, and AISI stainless steels 201, 316L, 410, and 430 by conducting electrochemical tests. Simulated BOs were composed of a base solvent (85 wt% deionized water and 15% methanol) and 0.1 M solute. Ni-mesh and mercury surface electrodes served as counter and reference electrodes, respectively. Each alloy was also tested in 0.1 M NaCl solution for comparison. Open circuit potential (OCP) was measured before EIS, and PDP was conducted after the EIS measurement and OCP delay. The resistance against corrosion reactions, R_2, was obtained for each steel by fitting an equivalent circuit model to EIS spectra. Stainless steels exhibited high R_2 values indicating passive states, whereas 2.25Cr-1Mo steel showed low R_2 values associated with active corrosion. The steel 9Cr-1Mo was corrosion-resistant to only the simulated BO containing catechol but not to the others. Steels in the simulated BO containing lactobionic acid had lower R_2 values than those in other simulated BOs, which

suggested that lactobionic acid was more aggressive to passive films. They also concluded that stainless steels with critical Cr levels of around 11 wt% would be corrosion-resistant to organic acids by forming a Cr-rich passive film.

1.4. Fluid Catalytic Cracking (FCC) Processes

The breakdown of long-chain hydrocarbons into light compounds via interacting with catalysts (e.g. zeolite) at high temperatures is known as FCC. FCC is one of the most important oil upgrading techniques in a refinery converting low-quality oils into drop-in fuels. This process is carried out in an FCC unit and there are over 400 active FCC units worldwide producing 500 million tonnes of gasoline per year [57, 58]. In an oil refinery, crude oil extracted from the ground is firstly processed by atmospheric distillation to be separated into various distillation cuts, among which heavy fractions are further processed by vacuum distillation. The typical feed used for FCC is VGO produced from vacuum distillation units. The FCC process can handle a wide range of feedstock and its operating conditions can be varied to maximize yields [59]. The conversion of VGO in an FCC unit depends on several parameters such as feed composition, temperature, pressure, catalyst type, and the catalyst-to-oil ratio [57].

The FCC unit has two core components namely the reactor and regenerator. The reactor has two main parts including the riser where the cracking of feed takes place and the separator at which the separation of cracked products from the deactivated catalyst is carried out. Meanwhile, activation of spent catalysts by removing coke is carried out in the regenerator. The most common catalysts used for FCC operations are zeolites and their variants and the typical catalyst-to-oil ratio ranges from 4 to 10 [60]. Carbon steel is commonly used as the construction material for the FCC

unit, whereas stainless steel is used for components such as feeding nozzles [58].

During the FCC process, VGO is preheated to 260–372 °C and then introduced into the riser (about 550 °C) through the injection system, where it contacts with hot catalysts (677–732º C) coming from the regenerator and cracked into light products [58, 61]. The yield products are separated from the catalyst and sent for further treatment to a fractionation column, while the catalyst is sent back to the regenerator by gravity motion. During the FCC process, the deposition of heavy compounds (i.e., coke) would result in the deactivation of catalysts. The coke formed onto the catalyst is burned off by passing hot air through the catalyst bed in the regenerator [62]. The residue heat is further used for feed preheating.

1.5. Bio-oil (BO) Upgrading via the Co-processing Strategy

Due to the low thermal stability and high corrosivity of BO, upgrading is a "Must" to convert crude BO into drop-in biofuels. There are other available biofuel options, but their properties and availability restrain for wide applications. For instance, ethanol, as an alternative biofuel, has drawn much attention, but the low energy density (around 70% of gasoline) hinders its application for heavy trucks or aircraft. Although bigger alcohols like n-butanol and i-butanol are more energy-intensive, the low productivity makes the production not economically viable. Fatty oils have been also considered to produce transportation fuels such as biodiesel. However, such a strategy is unlikely to be implemented on a large enough scale to meet fuel demand due to the requirement for land to grow the crops.

The essence of BO upgrading is to produce chemicals similar to petroleum-based fuels such as

gasoline, jet fuel and diesel. There are various upgrading techniques to improve the properties of crude BO [63]. For instance, hydrotreating can catalytically remove problematic oxygen from crude BOs by adding hydrogen. However, the hydrotreating process requires dedicated equipment and a massive amount of hydrogen, implying large capital and operational costs. In addition, due to the wide size distribution of molecules in hydrotreated BOs, a few follow-up operation units such as fractionation, cracking and isomerization are needed to obtain engine-level fuels, which further increases the complexity and thus the cost of the bio-refinery.

BO can also be upgraded by FCC. Upgrading crude BOs by direct catalytic cracking causes severe char and coke formation due to the hydrogen-deficit nature and instability of crude BOs [64, 65]. Co-processing BOs with petroleum intermediates provides a promising solution [66]. The co-processing process utilizes the existing FCC units without or with minor modifications for the infrastructure providing a more convenient, faster and ready-to-use pathway toward biofuel implementation on the market [67]. In the riser of a FCC unit, vaporized BOs contact with catalysts to produce higher quality transportation fuels such as diesel, gasoline and jet fuels [68, 69]. Meanwhile, the oxygenates in BOs are converted to water, CO_2 and CO [70]. Compared to a standalone biorefinery, upgrading biomass-derived oils using co-processing BOs with petroleum intermediates in the existing refining infrastructure can save about 20% cost [71]. Research indicated that 92% of U.S. petroleum refineries could co-process 5–20 wt% crude BO without triggering major permitting requirements. Every year approximately 1.9 billion gallons of gasoline-equivalent of renewable fuel can be potentially produced, corresponding to 1.4% of U.S. gasoline consumption in 2018 [72].

1.6. Upgrading Bio-oil (BO) by Emulsification

Many works have been done on upgrading BO by emulsification. BOs are blended into liquid fuels such as diesel or biodiesel with the assistance of surfactants, during which no chemical reactions are required, and all BO components are used as fuel resources [73-77]. An emulsion can be understood as a mixture of two immiscible fluids in which one liquid (dispersed phase) as droplets are dispersed in the other (continuous phase). An emulsion has a droplet size in the range of 1–10 µm, whereas it can be referred to as a microemulsion when the droplet size is between 1 nm and 100 nm [78]. Although emulsification can stabilize BOs, reduce their corrosivity and obtain more reliable fuel ignition characteristics [79], the stability of the resultant emulsion and the consumption of surfactants are two major concerns for this upgrading method. Leng et al. [80] produced microemulsions of BO derived by hydrothermal liquefication (< 5 wt%) and diesel, but with high consumption of surfactant (~ 40 wt% of BO). Prakash et al. [81] assessed the feasibility of emulsifying wood pyrolysis BO (5–15 vol%) in methyl ester of jatropha. Although the fuel properties of the produced emulsions were comparable to diesel, the surfactant consumption was as high as 4 vol%. Adding additives such as ethanol can reduce the usage of surfactants [82]. Chiaramonti et al. [83] successfully used polymeric surfactants (< 1 wt%) with short-chain additives to produce BO (up to 25 wt%) and diesel emulsions.

Lu et al. [84] investigated the corrosion of mild steel Q235A, and stainless steel AISI321 by rice husk–derived pyrolysis BO and its emulsions with diesel (10 and 30 wt% BO). Both emulsions contained a 1.5 wt% surfactant that assisted BO droplets to be dispersed into the continuous phase (diesel). The stability tests showed that the emulsions were stable for over 10 days at room temperature. Although the fuel properties of BO/diesel emulsions improved compared to pure BO,

their pH value did not change accordingly. Metal strips were immersed in glass bottles containing BO at 25, 50, and 70 °C for up to 120 h. The experimental results concluded that mild steel was susceptible to both BO and BO/diesel emulsions. Loosely attached corrosion materials on mild steel could be completely washed out easily. Stainless steel was corrosion-resistant to the tested solutions. Increased Cr_2O_3 and NiO were detected on the surface of stainless steel after immersion experiments. The authors argued that the underlying metal was protected by the compact Cr_2O_3 passive film. Overall, BO emulsions were less corrosive compared to pure BO.

So far, limited work has been done on creating BO/VGO emulsions. The successful examples of BO/diesel emulsions provide a promising expectation for BO/VGO emulsions for co-processing in FCC units. It is expected that the miscibility of BO would be reduced after being emulsified with VGO. Injecting the BO/VGO emulsion as a single-phase fluid would reduce the risk of plugging the feeding lines, eliminate the modification requirement of the FCC injection system, and maximize the hydrogen transfer from hydrogen-rich VGO to hydrogen-deficit BO to increase the efficiency of the FCC processes.

1.7. Research Objectives

As discussed above, it is essential to upgrade BO to drop-in fuels to expand the use of renewable bio-resources. BO co-processing with VGO in existing FCC infrastructures shows great promise for BO upgrading. Before implementing this upgrading strategy, it is crucial to comprehend the properties and corrosion risks associated with BO to ensure safe operations. This thesis outlines four primary objectives.

Objective 1: Evaluating and improving the thermal stability of BO. BOs are inherently unstable, particularly at elevated temperatures due to the presence of numerous oxygenated compounds. To ensure the flowability and quality of BO, it is critical to slow down the aging process of BO during its storage, transportation, and pre-heating processes. Objective 1 involves monitoring the physical and chemical properties of BO and various BO/methanol mixtures after undergoing accelerated aging.

Objective 2: Investigating the corrosion of structural alloys in BO environments. Corrosion risks of BO to common FCC construction materials must be assessed to ensure the safety of the co-processing operation. Within this objective, immersion experiments, as the most direct way for corrosion evaluation, are conducted for alloys in BO blends. Meanwhile, electrochemical measurements, as a non-destructive and quick corrosion assessment method, are developed to suit the use for corrosion studies of metals in low-conductive BO environments.

Objective 3: Assessing the evolved gases after BO aging and immersion experiments and evaluating the effect of steel corrosion on BO aging. Various gases are generated during BO aging. There are also gas products as a result of BO corrosion to metals. Moreover, steel corrosion would affect the aging rate of BO and promote BO internal reactions releasing gases. It is important to qualitatively and quantitatively understand the gases generated during BO operations. Objective 3 concentrates on evaluating the gas byproducts evolved from BO aging and immersion experiments via GC analysis and examines how steel corrosion would affect BO aging.

Objective 4: Enhancing the miscibility of BO with VGO via emulsification. The limited

miscibility of BO with VGO hinders the injection of BO/VGO mixtures as a homogeneous single-phase fluid. Objective 4 focuses on improving the miscibility of BO with VGO through emulsification. Surfactants are employed to create BO/VGO emulsions. The emulsion quality is assessed based on its stability, corrosivity, and surfactant-to-BO ratio.

1.8. Thesis Outlines

Chapter 1 introduces the characteristics and upgrading strategy of BO and outlines the research objectives of this study. **Chapter 2** elaborates on the methodologies adopted to accomplish the research objectives. **Chapter 3** discussed the impact of methanol addition on BO aging and steel corrosion. **Chapter 4** presents a corrosion assessment of steels in BO utilizing modified electrochemical techniques. **Chapter 5** focuses on analyzing the gas products during BO aging and steel corrosion. **Chapter 6** showcases the development of stabilized BO/VGO emulsions employing an innovative surfactant system. **Chapter 7** summarizes experimental findings and provides recommendations for future research.

Chapter 2. Methodologies

2.1. Bio-oil (BO) Aging Experiments

The bio-oil (BO) used for this thesis was produced from pinewood by fast pyrolysis. Pure BO and mixtures of BO blended with 5, 10, 15, and 20 wt% methanol (ME) were used for aging experiments. BO samples were sealed in glass jars and stored for 24, 96 and 168 h in an oven at temperatures of 50 and 80 °C. The neck finishes of these jars were wrapped with Teflon™ tapes to minimize weight loss. The jars were weighed before and after testing to ensure weight loss was less than 1 wt%.

2.2. Bio-oil (BO) Characterizations

A battery of analytical tests was proposed to examine the properties of BO that were liable to change during the aging process. After aging experiments, the BO mixtures were characterized through viscosity, density, water content and pH measurements. Water content was measured using a Coulomat AG-H titrant. Before measuring water content, BO was diluted 100 times using ME. The true water content of BO was calculated from the measured value of the diluted solution after subtracting the trace amount of water found in ME. Ash content was measured by burning 15 mg of BO and holding it at 775 °C for 20 minutes in a crucible with flowing air. All measurements were conducted at room temperature at least 3 times or until results stabilized. Thermogravimetric analysis (TGA) was performed on BO samples in a flowing argon atmosphere (50 mL/min). The weight losses of BO samples were tracked as they were being heated from 30 to 750 °C at a constant rate of 10°C /min. Elemental analysis was performed to determine the carbon, hydrogen, nitrogen, and sulfur content in BO, and the oxygen content was calculated by difference. The heating value for BO was calculated from Dulong's formula based on its elemental composition.

Besides, the functional groups within BO were determined by Fourier-transform infrared spectroscopy (FT-IR) tests using Thermo Nicolet 8700 with an attached Continuum FT-IR microscope. To observe changes in chemical composition during BO aging, Gas chromatography–mass spectrometry (GC–MS) was performed using the Agilent 5977A Series GC/MSD System with an HP-5MS column (30 m length × 250 μm inner diameter × 0.25 μm thickness). The MS library search results were obtained using NIST11. In each measurement, 0.1 μL of BO sample was injected. The oven temperature was programmed to increase from 40 °C (held for 5 min) to 290 °C (held for 5 min) at a rate of 10 °C/min. Helium was used as a carrier gas at a flow rate of 3 mL/min. **Table 2.1** lists the equipment used for BO characterizations.

Table 2.1. BO characterization methods.

Property	Equipment
Viscosity	Brookfield DV-III™ Ultra Rheometer
Density	Anton Paar DMA 35 Density Meter
Water content	Mettler Toledo C10S Coulometric KF Titrator
pH value	Thermo Scientific™ Orion Star A211
Ash content	Muffle furnace
Elemental analysis	Thermo Scientific™ FLASH 2000 CHNS/O Analyzers
FT-IR	Thermo Nicolet 8700
GC-MS	Agilent 5977A Series GC/MSD System with an HP-5MS column
TGA	Thermo Cahn TherMax 300

2.3. Bio-oil (BO) Corrosivity Assessments

2.3.1. Immersion Experiments

Carbon steel (CS) and two grades of stainless steel, 304L and 316L, were used for immersion experiments. Each metal was etched to reveal grains and observe microstructures. The immersion

tests followed the procedures of ASTM G31. Metal strip coupons with dimensions of 1×1/4×1/16 in^3 were polished to a 600-grit finish. Before immersion experiments, metal coupons were cleaned with ME in an ultrasonic bath for 10 minutes, and then rinsed with deionized (DI) water. The immersion experiments were performed by putting metal coupons anchored with PTFE holders in glass jars filled with pure BO and its blends with ME. The immersion experiments were conducted at 50 and 80 °C for 168 h and repeated 4 times. After immersion, Q-tips were used to gently remove corrosion products on metal surfaces. The metal coupons were then cleaned in an ultrasonic bath with ME and acetone for 10 minutes each. Finally, they were rinsed in DI water and dried. The coupon weights were recorded before and after the immersion tests to calculate the corrosion rate.

2.3.2. Electrochemical Measurements (EMs)

The electrochemical measurements (EMs) were performed with CS at 20 and 50 °C. The surface of the metal coupons was ground to a 600-grit SiC finish. The electrolytes used for this study included BO and BO blended with 10 and 20 wt% ME. Additionally, 0.1M acetic acid in DI water was used for comparison.

The potentiostat used for EMs was a Princeton Applied Research Versastat 4 potentiostat. A four-electrode cell was used including a CS specimen mounted in epoxy resin with an exposed surface area of 0.4 cm^2 serving as the working electrode, a platinum mesh as the counter electrode, a RE-7 non-aqueous reference electrode (Ag/Ag$^+$) (0.345 V vs. Ag/AgCl saturated KCl electrode), and a working sense electrode. A water bath was connected to a water-jacketed cell to control the electrolyte temperature. All EMs were conducted in a Faraday shield to minimize electromagnetic interference outside of the system.

The EMs were conducted as follows: (1) Open circuit potential (OCP) measurements were carried out for at least 1 h to let the system reach a steady state; (2) Electrochemical impedance spectroscopy (EIS) measurements were conducted afterwards. The frequency range and amplitude for EIS measurements were set as 0.1Hz–1000 Hz and ±5 mV against OCP, respectively; (3) Potentiodynamic polarization measurements were performed from -0.25 V vs. OCP up to +1.6 V vs. OCP with a scan rate of 0.167 mV/s; and (4) Tafel scans were performed individually with new CS samples from -0.15V vs. OCP to +0.15 V vs. OCP with a scan rate of 0.167 mV/s. Parallel immersion experiments were conducted for CS strip coupons in the electrolytes mentioned above.

2.4. Metal Surface Characterizations

Optical microscopy and scanning electron microscopy with energy-dispersive X-ray spectroscopy were used to observe the surface morphology of metal coupons and analyze the elemental composition of the corrosion products on the metal surfaces after immersion experiments. X-ray diffraction was performed on post-corrosion metal coupons to identify the corrosion products. X-ray photoelectron spectroscopy was conducted to examine the bonding between components in steel and BO.

2.5. Gas Analysis by Gas Chromatography (GC)

Gas chromatography (GC) was used to characterize the evolved gases during BO aging experiments and CS immersion experiments. The GC equipment was the Agilent 8890 series GC system with an Agilent J&W capillary GC column (15 m length×320 μm inner diameter×5 μm thickness). An autoclave was used for the aging and immersion experiments. A digital pressure

gauge was connected to the autoclave to monitor the pressure. The autoclave was heated by a heating mantle, and the temperature was monitored by a thermocouple. For each trial, 100 mL of BO contained in a PTFE container was placed inside the autoclave. For the immersion experiment, two CS strip coupons were immersed in BO (similar to **Section 2.3.1.**). The aging and immersion experiments were carried out at 80 °C for 168 h. After the experiments, the autoclave was cooled overnight to reach room temperature. The remaining gases were collected by aluminum foil bags via the outlet of the autoclave. Then collected gases were analyzed by GC. Two thermal conductivity detectors (TCDs) in GC were used to detect non-hydrocarbon gases. One of the TCDs was used for detecting H_2 using N_2 as the carrier gas. The other TCD was used to detect nonhydrocarbon gases such as CO and CO_2 using H_2 as the carrier gas. The flame ionized detector (FID) was used to detect hydrocarbon gases, where N_2 was used as the carrier gas. The GC oven temperature was programmed to increase from 60 °C (held for 1min) to 190 °C (held for 10min) at a rate of 20 °C/min. The FID and TCD were set at 250 °C.

2.6. Bio-oil (BO) Emulsification

2.6.1. Making the BO/VGO Emulsions

A typical vacuum gas oil (VGO) produced in Alberta, Canada was used in this study. BO/VGO emulsions were made by a homogenizer with a BO concentration of 20 wt%. Three surfactants with different hydrophilic-lipophilic balance (HLB) values were used in this study including Span 80 (SP), Tween 80 (TW) and a mixture of the two (ST) with an HLB value equals to 8. The ST was prepared by mixing 65.4 g of SP and 34.6 g of TW and stirring for 60 min. ME was used as a co-surfactant to further stabilize emulsions. The homogenizer ran at 10,000 rpm for 10 min. The total weight of 100 g emulsion was made each time in a wide-mouth jar. Before homogenizing,

BO and VGO were heated to 50 °C. Surfactants and ME were gradually dropped into BO/VGO mixtures during the homogenization process. The surfactant and ME concentrations were 10 wt% of BO.

2.6.2. Emulsion Stability Characterizations

The stability of BO/VGO emulsions was evaluated from two aspects—aging of emulsions determined by TGA and phase separation time of emulsions revealed by X-ray imaging. For aging experiments, emulsions were contained in a water-jacketed beaker to maintain their temperatures at 50 °C while being stirred at a rate of 400 rpm to keep from phase separation. Emulsion samples, taken at the beginning (*i.e.*, 0 h) and after aging for 24, 96, and 168 h were conducted for TGA. To evaluate the phase stability of emulsions, X-ray equipment was employed to image emulsions at a time interval of 10 min. Emulsions were stored in a glass vial which was then put inside a plastic jar coated with a silicone heating tape. The temperature inside the jar was kept at 50 °C. A thermocouple was inserted into the glass vial for monitoring the temperature of emulsions. Optical micrographs of emulsions were also taken to elucidate the effect of emulsion microstructures on the stability of emulsions. In parallel, immersion experiments were conducted with CS coupons in the emulsions to elucidate the effect of emulsification on BO corrosivity.

Chapter 3. Influence of Methanol Addition on Bio-oil Thermal Stability and Corrosivity

Abstract

Bio-oil (BO) has been considered to be upgraded via co-processing with petroleum intermediates in existing fluid catalytic cracking (FCC) units to produce drop-in fuels. However, the low stability and high corrosivity of BO are two major obstacles preventing further advances in BO upgrading processes. Previously, efforts have been made to improve BO stability through the use of additives, with methanol as a promising candidate. Yet, the effect of these additives on BO corrosivity has not been fully understood. In this study, both the stability and corrosivity of BO with methanol addition are analyzed. BO was blended with methanol at concentrations of 5–20 wt%. These mixtures were subject to accelerated aging at 50 and 80 °C up to 168 h. Fourier-transform infrared spectroscopy, gas chromatography–mass spectrometry, and thermogravimetric analyses were conducted to identify functional groups, chemical components, and thermal behaviors of BO, respectively. Viscosity, density, water content and pH value were also measured to track the physical/chemical property changes of BO and BO/methanol mixtures during aging. Alongside, immersion experiments with common FCC structural materials such as carbon steel (CS) and stainless steels (SS) 304L and 316L were conducted in BO and BO/methanol mixtures, at 50 and 80 °C for 168 h. The viscosity-increasing rate of BO was dramatically lowered by adding methanol, especially at 80 °C, indicating that adding methanol was effective in stabilizing BO. For corrosivity investigation, CS corroded severely in tested BO mixtures. At 50 °C, it was found that CS immersed in BO mixtures with higher methanol content corroded at a more significant rate; whereas at 80 °C, the corrosion rate of CS initially increased with methanol concentration in BO and then declined. SS 304L exhibited moderate corrosion rates at 80 °C, while SS 316L showed

minimal corrosion at the tested conditions. It has been observed that CS accelerated the viscosity increase rate of BO, especially after being aged at 80 °C for 168 h (2125 cP without CS vs. 64,500 cP with CS). After immersion experiments, abnormally high C, O, and N content were identified on rigorously cleaned metal coupon surfaces. A combination of viscosity measurements and surface characterization suggested that chelation between organic compounds and metal atoms/ions played a significant role in the corrosion of steels in BO. A mechanism has been proposed to justify the corrosion behavior of steels in BO/methanol mixtures.

Keywords: Bio-oil, Thermal Stability, Corrosion, Methanol Addition, Co-processing, Steels

3.1. Introduction

In recent decades, human activities have greatly accelerated the emission of greenhouse gases (GHG). CO_2, accounting for the majority of GHG emissions, results in a magnified planetary warming effect. In response, countries around the world have implemented policies to limit carbon emission by incentivizing cleaner fuel and energy options. For instance, in Canada, the Clean Fuel Standard (CFS) is designed to accelerate the use of clean technologies and low carbon fuels to reduce GHG emissions and is to be fully implemented by 2022 [85]. The CFS requires corporations to reduce the carbon intensity of liquid fuels by 13% over the next decade. The Government of Canada has also passed the Greenhouse Gas Pollution Pricing Act in 2018, with the objective of taxing carbon emission [86]. Due to the ever-increasing motivation for lower carbon emissions and cleaner energy options, BO is becoming an attractive fuel option.

Raw biomass materials, such as wood and forestry residues, crops and crop residues, marine

products, and bio-wastes, are abundant renewable energy sources that can be converted to liquid fuels commonly referred to as bio-oil (BO) [6-9]. BOs are considered to be carbon-neutral and contain a relatively low level of sulfur, so using BOs would reduce net CO_2 emission and mitigate the sulfur-related environmental problems (e.g., acid rain) [15, 87]. Despite the advantages of using BO, the stability and corrosivity of BO remain uncertain, which may lead to issues during BO production, subsequent processing, storage, transport, and upgrading. On one hand, BOs are not as stable as conventional petroleum fuels due to the presence of a large number of oxygenated compounds and low-boiling volatiles [88]. Organic compounds having hydroxyl, carbonyl, and carboxyl groups can react with each other and form larger molecules through reactions such as esterification and etherification [25]. At high temperatures (> 50 °C), the viscosity of BO rapidly increases, which leads to BO polymerization, phase separation, and coke formation [26]. On the other hand, BOs contain a considerable amount of water and organic acids. The ash in biomass, mainly composed of alkali and alkaline earth metals, influences the stability of BO by promoting water and acids formation during pyrolysis [89]. These undesirable metallic species however can be removed via leaching pre-treatments, thus reducing the water content yield and improving the stability of BO [90]. The pH value and total acid number of BO can be as low as 2 and up to 100 mgKOH/g, respectively [25, 31]. These high levels of acidity in BO can cause corrosion problems on many common structural materials.

Previous studies have indicated that carbon steel (CS) has unfavorable corrosion resistance to BOs, whereas stainless steels (SS) have shown acceptable corrosion resistance [32, 45, 84]. Steels with higher Cr content were found to be more corrosion-resisting to BOs [49]. Aubin and Roy [44] studied the corrosion of wood pyrolysis oils on steels at 25 and 45 °C. They reported that SS

performed well but CS corroded severely in pyrolysis oils. Oasmaa et al. [32] worked on the corrosion of various metals in hardwood pyrolysis oil at temperatures up to 80 °C for 6 weeks. It was found that the performance of 316 SS was better than 304 SS, which was attributed to a small amount of Mo alloying element. Darmstadt et al. [45] studied the corrosion of 316 SS in softwood bark residue vacuum pyrolysis oil at 80 °C and concluded that the 316 SS was corrosion-resistant to the pyrolysis oil. They proposed that after Fe contents were leached from the metal surface, Cr migrated from the bulk toward the surface of the steel substrate and formed a protective Cr oxide layer. Keiser et al. [47, 48] studied the corrosion of various steels in pyrolysis oils at 50 °C for a total of 1000 h. They found that there was significant weight loss in CS such that the calculated corrosion rates cannot be tolerated as the structural materials intended to last for years. Minimal weight loss was identified on the SS specimens under the same experimental conditions.

It has been proved that blending a small portion of alcohols (such as methanol and ethanol) into BO could reduce the aging rate and improve the thermal stability of BO [35, 36]. Several mechanisms have been proposed to explain these effects [35]. Firstly, adding alcohol can slow the BO internal reactions by physical dilution. Besides, monofunctional alcohols (e.g., methanol) can react with acidic oligomers to form oligomeric esters which can further react with alcohols to form lower-molecular-weight methyl esters through transesterification reactions. These chain termination reactions of oligomers slow down the aging rate of BO by making fewer reactive sites available for polymerization reactions. Alcohols also consume aldehyde groups to produce acetals, which reduces their availability for polymerization reactions. Diebold and Czernik [35] performed accelerated aging tests for BO at 90 °C to exam the effect of additives such as methanol, ethanol, and acetone on BO aging. They concluded that methanol (10 wt%) was the most adequate stabilizer

since the BO/methanol blend was maintained as a single-phase after 96 h exposure to 90 °C. Oasmaa et al. [41] conducted accelerated aging tests with BO/alcohol (methanol, ethanol, and isopropanol) mixtures at 80 °C for up to 24 h. They found that adding alcohol instantly decreased the viscosity and density of BO. During storage, alcohols slowed the viscosity and molecular mass increasing rates of BO. Mei et al. [42] investigated the storage stability of pinewood-derived BO with methanol addition of 3–15 wt% at 25 °C for 35 days. They found that as the methanol concentration increased, the BO viscosity and water content increasing rates declined. Furthermore, the pH value of BO slightly increased during storage when the methanol content was above 6 wt%. In recent years, composite additives have been investigated to improve the stability of BO [37-40]. However, these composite additives contain nitrogen or sulfur which can lead to the production of undesirable gases during BO upgrading and combustion.

Although various additives have been advanced to stabilize BOs, little effort has been made to investigate the effect of these additives on BO corrosivity. To produce drop-in biofuels, crude BOs need to be further upgraded. Co-processing BOs with petroleum intermediates such as vacuum gas oil in existing fluid catalytic cracking (FCC) units provides a promising solution [66, 91, 92]. The corrosion behavior of FCC structural steels in contact with BOs needs to be further understood to ensure the safety of BO processing [19]. In this study, the effects of methanol addition (5–20 wt%) on the thermal stability and corrosivity of BO were investigated. A series of aging and parallel corrosion experiments were conducted at 50 and 80 °C for up to 168 h. The thermal stability of BO was evaluated by tracking the BO physical and chemical properties such as viscosity, density, water content, and pH value during aging tests. Steel coupons of CS, 304L SS, and SS 316L were used for immersion experiments. Weight changes of these coupons were recorded for corrosion

rate calculations.

3.2. Experimental Setup

3.2.1. Bio-oil (BO) Characterization

Pinewood-derived BO (BTG Bioliquids) by fast pyrolysis was used in this study. **Table 3.1** lists some basic properties of the BO and equipment used to measure these properties. Water content was measured using a Coulomat AG-H (HYDRANAL™) titrant. Before measuring water content, BO was diluted 100 times using methanol. The true water content of BO was calculated from the measured value of the diluted solution after subtracting the trace amount of water found in methanol. Ash content was measured by burning 15 mg of BO and holding it at 775 °C for 20 minutes in a crucible with flowing air. Elemental analysis was performed to determine the carbon, hydrogen, nitrogen, and sulfur content in BO, and the oxygen content was calculated by difference. The heating value for BO was calculated from Dulong's formula [93] based on its elemental composition. Besides, the functional groups within BO were determined by Fourier-transform infrared spectroscopy (FT-IR) tests using Thermo Nicolet 8700 with an attached Continuum FT-IR microscope.

Table 3.1. Basic properties of the BO used in this study and characterization methods.

Property	Value	Equipment
Viscosity[a]	171.5 cP	Brookfield DV-III™ Ultra Rheometer
Density[a]	1.20 g/mL	Anton Paar DMA 35 Density Meter
Water content[a]	24.7 wt%	Mettler Toledo C10S Coulometric KF Titrator
pH Value	2.83	Thermo Scientific™ Orion Star A211
Ash content	0.05 wt%	Muffle furnace
Heating Value[b]	17.4 MJ/Kg	
Elemental analysis (wt%)		Thermo Scientific™ FLASH 2000 CHNS/O Analyzers
C (45.88), H (7.17), N (0.24),		
S (0), O[c] (46.71)		

[a]Measured at room temperature for multiple times until stabilized; [b]Calculated by Dulong's formula; [c]By difference

3.2.2. Aging Experiments

Pure BO and mixtures of BO blended with 5, 10, 15, and 20 wt% methanol additions (99.9% purity, Fisher Chemical™ BPA4544) were used for aging tests. BO samples were sealed in 125 mL glass jars (Fisherbrand™ WW014214) and stored for 24, 96 and 168 h in an oven (Heratherm™) at temperatures of 50 and 80 °C. The neck finishes of these jars were sealed with Teflon™ wrap to minimize evaporation. Jars were weighed before and after testing to ensure evaporation loss was less than 1 wt%. After aging tests, BO mixtures were characterized through viscosity, density, water content and pH measurements. All measurements were conducted at room temperature at least 3 times or until results stabilized. To observe changes in chemical composition during BO aging, Gas chromatography–mass spectrometry (GC–MS) was performed using the Agilent 5977A Series GC/MSD System with a HP-5MS column (30 m length × 250 μm inner diameter × 0.25 μm thickness). The MS library search results were obtained using NIST11. In each

measurement, 0.1 µL of BO sample was injected. The oven temperature was programmed to increase from 40 °C (held for 5 min) to 290 °C (held for 5 min) at a rate of 10 °C/min. Helium was used as a carrier gas at a flowrate of 3 mL/min. Thermogravimetric analysis (TGA) was performed on BO samples in a flowing argon atmosphere (50 mL/min) using Thermo Cahn TherMax 300. The mass losses of BO samples were tracked as they were heated from 30 to 750 °C at a constant rate of 10°C /min.

3.2.3. Immersion Experiments

Three steels, including CS (A36), SS304L, and SS316L, were used for immersion experiments, and the corresponding chemical compositions are indicated in **Table 3.2**. A36 is commonly used in structural applications, while SS 304L and 316L are used in key parts such as injection nozzles. Each metal was etched to reveal grains and observe microstructures, as illustrated in **Fig. 3.1**. CS is composed of a mixture of ferrite and pearlite, while 304L and 316L SS have an austenite matrix with ferrite clusters. Immersion tests followed the procedures of ASTM G31 [94]. Metal strip coupons with dimensions of $1 \times 1/4 \times 1/16$ in^3 were polished to a 600-grit finish. Before immersion, metal coupons were cleaned with methanol in an ultrasonic bath for 10 minutes, then rinsed with deionized (DI) water. Immersion experiments were performed by putting metal coupons anchored with PTFE holders in glass jars filled with pure BO and BO/methanol mixtures. The immersion experiments were conducted at 50 and 80 °C for 168 h and repeated 4 times. After immersion, Q-tips were used to gently remove loosen corrosion products on metal surfaces. The metal coupons were then cleaned in an ultrasonic bath with methanol and acetone for 10 minutes each. Finally, they were rinsed in DI water and dried. The coupon weights were recorded prior to and after immersion to calculate the corrosion rate. Scanning Electron Microscopy (SEM) with Energy

Dispersive X-Ray spectroscopy (EDS) analysis (Tescan Vega3) was used to observe the surface morphology of corroded metal coupons and analyze the elemental composition of corrosion products on the metal surfaces after immersion experiments.

Table 3.2. Chemical compositions (wt%) of steels used in this study.

	Fe	C	Cr	Cu	Mn	Mo	Ni	P	Si	S	Other
A36	Bal.	0.2	0.05	0.04	0.74	0.006	0.01	0.007	0.008	0.008	V: 0.002
304L	Bal.	0.025	18.28	0.5	1.61	0.34	8.06	0.03	0.34	0.0012	N: 0.06
316L	Bal.	0.024	16.57	0.55	1.45	2.03	10.06	0.028	0.37	0.0013	N: 0.037; Co: 0.41
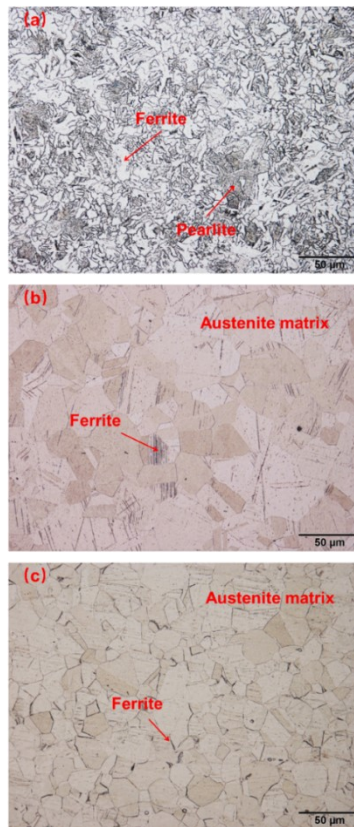
Fig. 3.1. Optical micrographs of etched metal specimens: (a) carbon steel; (b) 304L SS; and (c) 316L SS.

3.3. Results and Discussion

3.3.1. Bio-oil (BO) Aging Experiments

The FT-IR spectrum of BO used in this study is shown in **Fig. 3.2**. The O–H stretching vibration at 3409 cm^{-1} was associated with O–H bonds of water [95]. Due to the effect of hydrogen bonds, a broad absorbance was observed near the frequency of 3409 cm^{-1}. Aliphatic groups were identified at the absorbance frequencies of 2961, 2939, 1453, and 1374 cm^{-1} indicating there was a considerable amount of long carbon-chain compounds [38]. In the double bonds region (1500–2000 cm^{-1}), at 1716 cm^{-1}, the identified C=O stretch might belong to aldehydes, ketones, and organic acids in BO [42]. Besides, aromatics were shown to exist based on aromatic C=C ring breathing and aromatic ring vibrations at 1603 and 1516 cm^{-1}, respectively. In the fingerprint region (500–1500 cm^{-1}), various skeletal vibrations such as C–C and C–O were found indicating the existence of organic compounds such as alkanes, alcohols, phenols, ethers, and lipids. It is difficult to distinguish single chemical compounds from the FT-IR spectrum, as it can only identify a cluster of organic matters with similar functional groups. To obtain further details in the chemical composition of BO, GC–MS was employed.
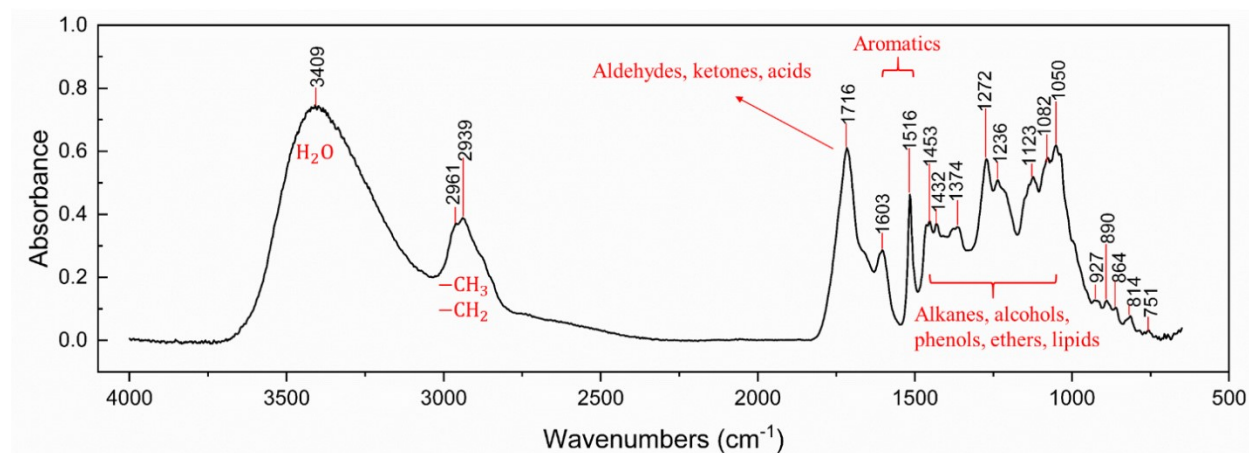
Fig. 3.2. FT-IR spectrum of the BO used in this study.

Fig. 3.3 presents a quantitative analysis of the major chemical compounds (#1–#14) detected in unaged BO and aged BO samples by GC–MS, with molecular weight increasing from left (#1, 124 g/mol) to right (#14, 345 g/mol). The unaged BO was mainly composed of sugar (#4, 37%), phenols (#1–#3, #5, and #6, 50%), ester (#7, 5%), and other chemical compounds, which were converted from cellulose, hemicellulose, and lignin in wood biomass [96]. The detected chemicals in unaged BO have also been reported elsewhere [97, 98]. After aging for 24 h at 50 °C, a phenolic compound, eugenol (#5) occupied more than 35% of the total BO composition, and a large carboxylic acid appeared (#9, 4%). When extending the aging time to 168 h, it was observed that heavier components (#10 and #14) with multiple carbon cyclic compounds accounted for around 15% of the total chemicals. For BO samples aged at 80 °C, more complex chemical compounds emerged (#8 and #11–#13) [99], with less low-molecular-weight phenols. During the aging process, light BO fractions were gradually transformed into high-molecular-weight compounds by internal chemical reactions [100], which was later also confirmed by TGA tests.
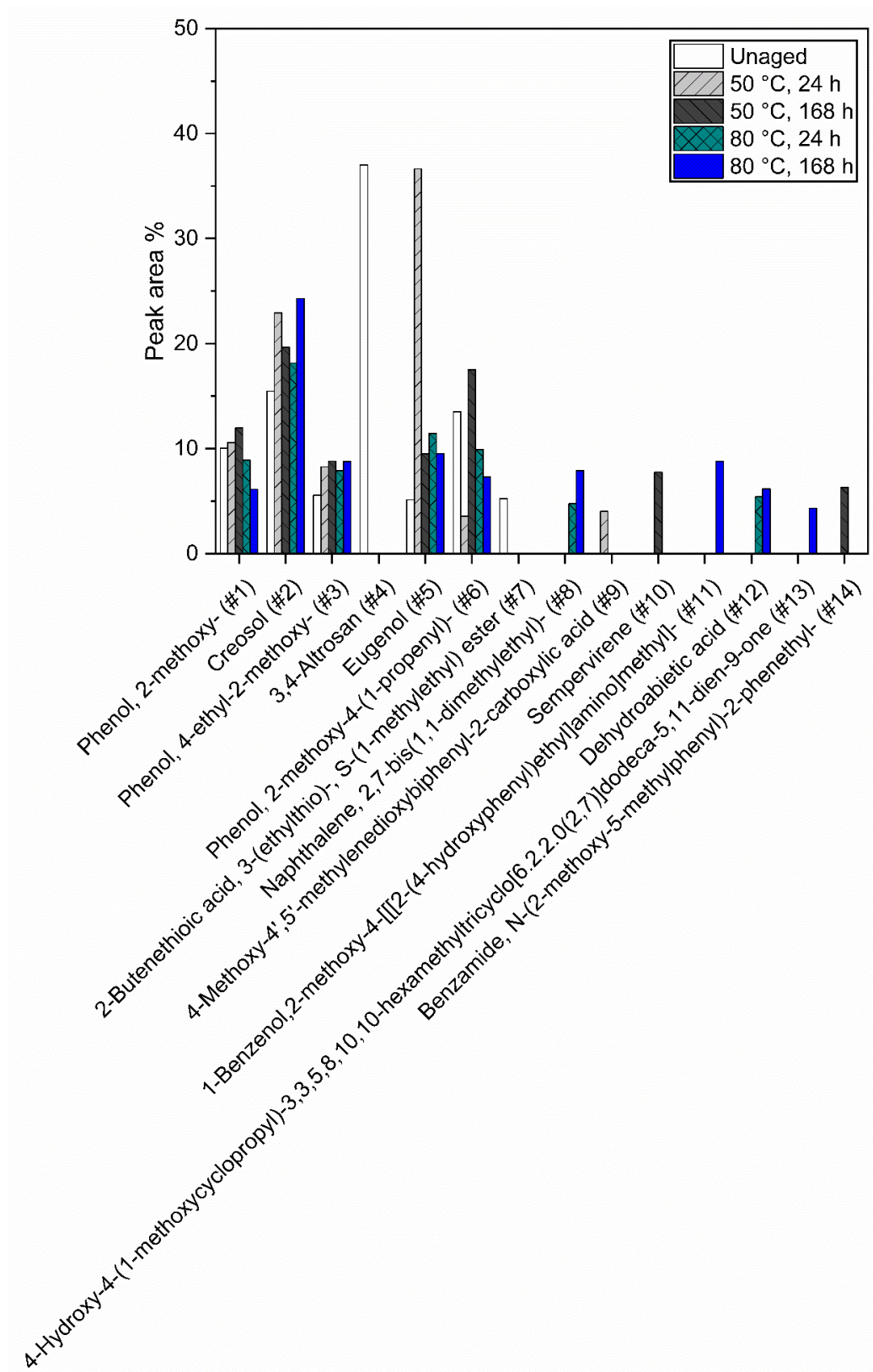
Fig. 3.3. Peak area% of major components in pure BO samples detected by GC–MS.

TGA tests were performed on unaged BO and aged BO samples to obtain the relationship between BO mass loss and temperature in an inert atmosphere (i.e., Argon). As shown in **Fig. 3.4**, the remaining weight percentage (denoted as TG) was plotted against temperature for unaged BO and the BO samples after aging for 24 and 168 h at 50 and 80 °C. Compared to unaged BO, the TG curves for aged samples shift to the upper right, indicating that the light fractions of BO transformed to high-molecular-weight compounds during aging. The distance between the TG curves of "blank" and "50 °C, 24 h" is larger than that between "50 °C, 24 h" and "50 °C, 168 h" (as shown by the dashed arrows). This indicates that the majority of the aging process at 50 °C had already completed after 24 h. For BO samples aged at 80 °C, the TG curves shift further to the upper right. Even though only aged for 24 h at this temperature, the TG curve of "80 °C, 24 h" is still higher than that of "50 °C, 168 h" manifesting that temperature plays a more significant role than aging time in BO aging. The rate of mass loss versus temperature, represented as DTG, was obtained by taking the first derivative of the TG curve. For clarity, only the DTG curves for unaged BO and BO aged for 168 h at 80 °C were plotted here. As indicated in **Fig. 3.4**, the valley for the DTG curve of unaged BO appears near 100 °C, which is attributed to the presence of a large amount of water in BO (24.7 wt%). The lowest valley of the "80 °C, 168h" DTG curve shifts to a temperature near 300 °C due to the formation of heavy organic matter. The GC–MS and TGA results confirmed that the light fraction of BO was gradually converting into heavy compounds during aging.
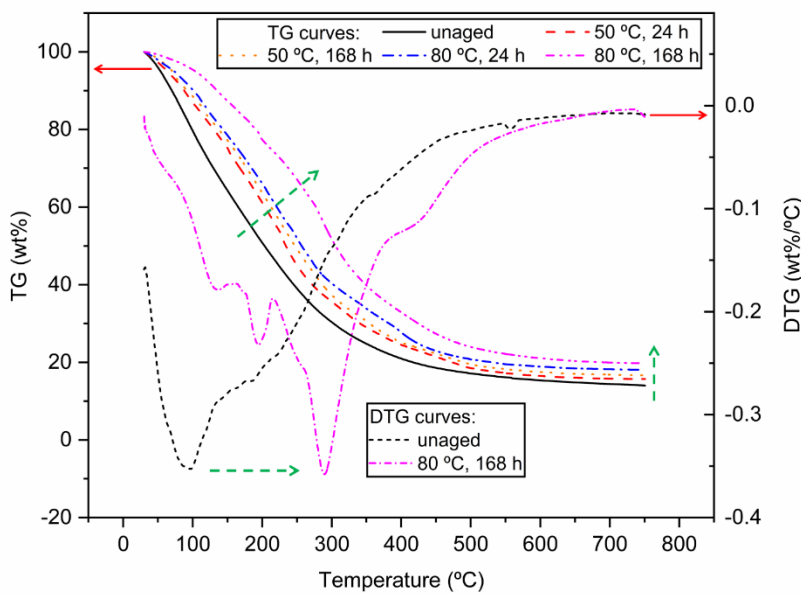
Fig. 3.4. TG and DTG curves of pure BO samples heated from 30 to 750 °C. Solid arrows indicate the corresponding Y-axis; dashed arrows present the shift due to aging.

In order to slow down BO aging, methanol was added, and its performance is discussed in the following. Changes in physical and chemical properties of BO samples during aging were tracked over time. Indicated in **Fig. 3.5** and **Fig. 3.6** are viscosity, density, water content, and pH values which were compared at different methanol concentrations and aging times at both 50 and 80 °C. The error of these measurements was less than 0.5%. After adding methanol, the viscosity, density, and water content of BO were instantaneously lowered by physical dilution as methanol has lower viscosity and density than BO and only contains a trace amount of water. The pH value of BO increased after blending methanol due to the dilution of acidic components. The effect of physical dilution increased with the increase of methanol concentration. Prior to aging, the rate at which viscosity was lowered by dilution declined as methanol concentration increased, while rates for density, water content and pH value changes were relatively linear.

36
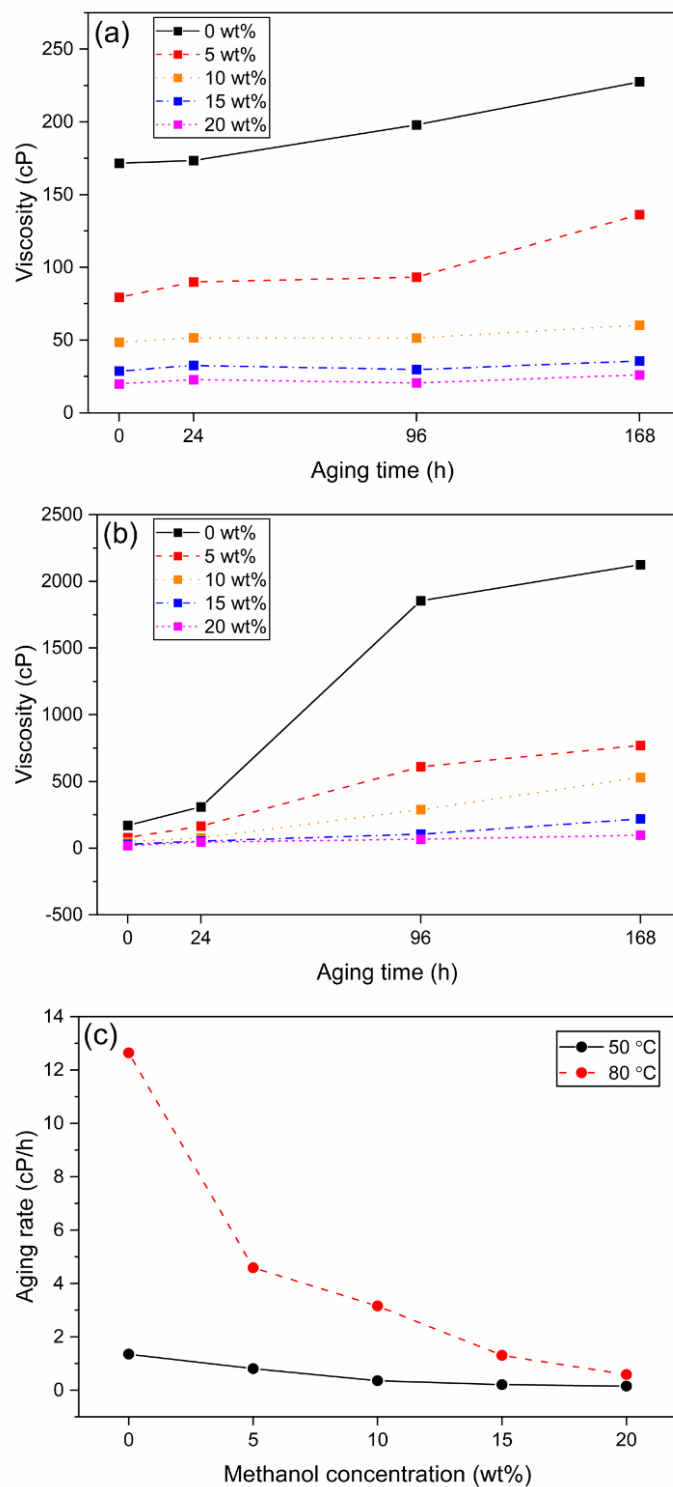
Fig. 3.5. Viscosity changes of pure BO and BO/methanol mixtures during aging: (a) at 50 °C; and (b) at 80 °C. (c) Aging rate (i.e., viscosity increasing rate) of pure BO and BO/methanol mixtures at 50 and 80 °C.
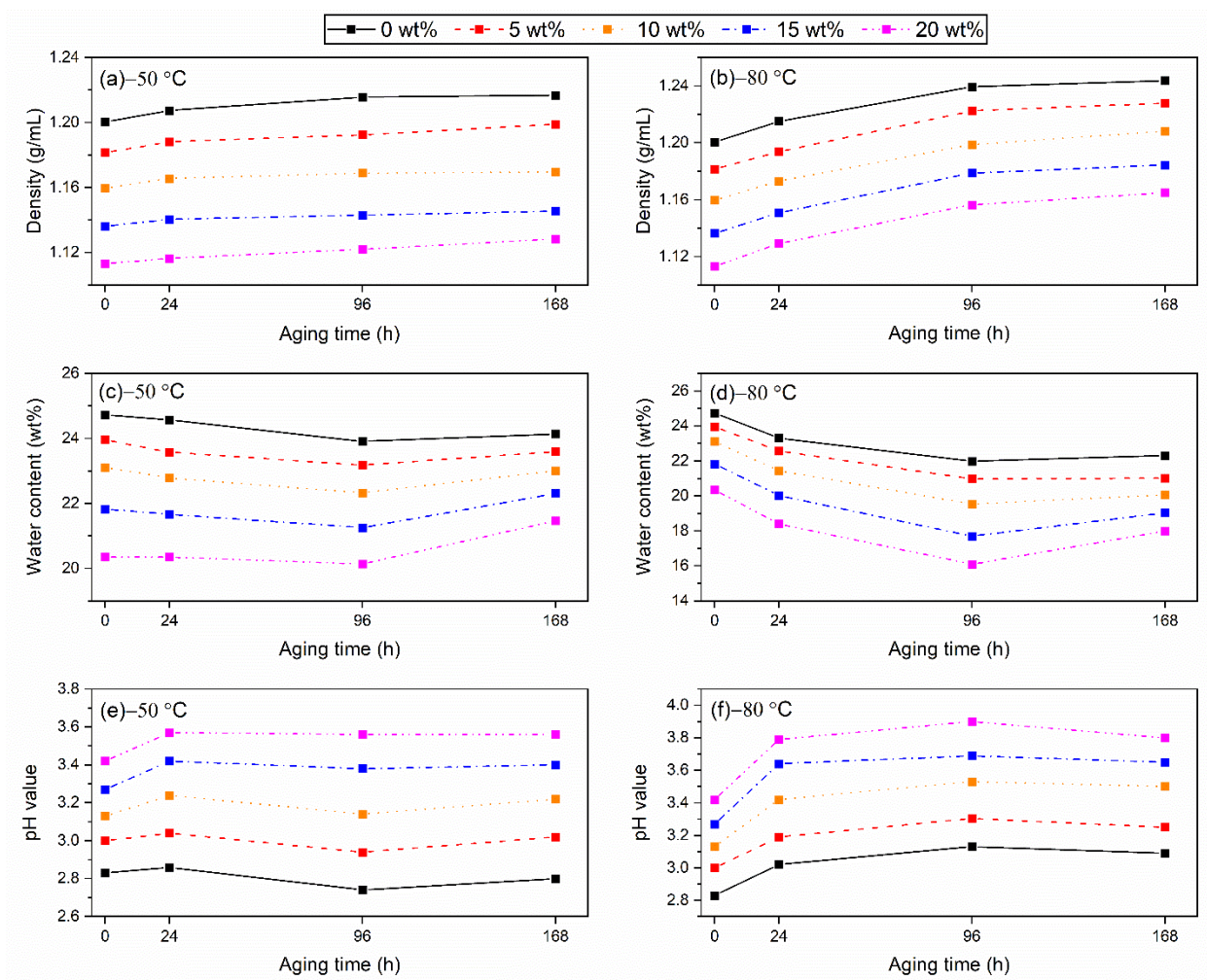
Fig. 3.6. Changes in density, water content, and pH value of pure BO and BO/methanol mixtures during aging: (a) density at 50 °C; (b) density at 80 °C; (c) water content at 50 °C; (d) water content at 80 °C; (e) pH value at 50 °C; and (f) pH value at 80 °C.

It was anticipated that the viscosity of BO would increase during aging due to the formation of high-molecular-weight compounds [35]. Since internal chemical reactions accelerate at higher temperatures, the viscosity increasing rate (i.e., aging rate) at 80 °C was expected to be faster than that at 50 °C [26, 101]. As shown in **Fig. 3.5**, at 50 °C the viscosity of pure BO increased from 171.5 cP (at time 0 h) to 227.5 cP (at time 168 h) with an aging rate of 1.35 cP/h. The aging rate

of BO declined when the methanol concentration was increased [102]. For instance, the BO with a 20 wt% methanol concentration aged at 0.15 cP/h, one order of magnitude lower than that of pure BO, indicating that adding methanol is effective in reducing the aging rate of BO. A combination of chain-termination reactions of acidic oligomers, methanol reactions with aldehydes and an overall deceleration of chemical reactions via dilution are presumed responsible for this reduction of aging rate as methanol concentration increases [35]. At 80°C, the aging rate of each BO sample was one order of magnitude higher than the corresponding mixture at 50 °C. The viscosity of pure BO increased dramatically to 2125 cP after 168 h, with an aging rate two orders of magnitude higher than that of the 20 wt% methanol mixture (12.7 vs. 0.58 cP/h). At 80 °C, a methanol addition of only 5 wt% could reduce the aging rate of BO by approximately 3 times to 4.58 cP/h, although the viscosity of BO after 168 h of aging was still considerably high (770 cP). Given economic consideration for practical applications, a 10 wt% methanol addition may be sufficient for BO storage at 50 °C. However, to maintain a relatively low aging rate of BO at 80 °C, it is necessary to either add at least 20 wt% methanol or limit the aging time of BO to 24 h, while adding at least 10 wt% methanol. The former option may not be economically viable whereas the latter will be more feasible when short periods of preheating and storage are carried out followed by immediate combustion, transportation, or upgrading.

A consistent rise in the density of BO during aging is illustrated in **Fig. 3.6**a–b. Due to accelerated aging at a higher temperature, the rate at which density increases is higher at 80 °C than at 50 °C. The density of pure BO increased by approximately 0.02 g/mL and 0.04 g/mL after aging for 168 h at 50 and 80 °C, respectively. At each aging temperature, the rate of density change appeared to be independent of methanol concentration. During aging, the water content and pH value of BO

fluctuated [38, 42], as denoted in **Fig. 3.6**c–f. Through the first 96 h of aging, water content decreased by less than 1 wt % at 50°C and by approximately 4 wt% at 80 °C. The more dramatic decrease in water content at 80 °C could be caused by greater rates of water-consuming reactions at this temperature. After this initial drop at both 50 and 80 °C, water content increased again until 168 h of aging; this could be explained by the involvement of aldehydes in different water-producing reactions or acids reacting with alcohols to form esters and water [103, 104]. Despite this, net decreases in water content of approximately 0.5 and 3 wt% were yielded for all BO samples aged at 50 and 80 °C, respectively. Furthermore, the pH values of all samples elevated for the first 24 h of aging before stabilizing, with only small changes being measured for the remainder of each test. This fluctuant behaviour in water content and pH can be justified by the nature of the complicated mechanisms that dictate chemical reactions of different oxygenated compounds. Various esterification, homopolymerization and acetalization reactions dominate over the course of the aging process, producing this varying behaviour in BO properties [35].

3.3.2. Metal Coupons Immersion Experiments

As adding methanol increased the pH value of BO, it was anticipated to observe lower corrosion rates of tested materials in BO/methanol mixtures. Ideally, methanol would react with oxidative organic compounds (e.g., carboxylic acids) in the BO to produce less-corrosive matters (e.g., esters). However, increases in the corrosion rate of CS were observed after adding methanol. At 50 °C, as illustrated in **Fig. 3.7**a¸ CS corroded at a rate of 1.5 mm/y when immersed in pure BO. This rate increased almost linearly with methanol concentration, reaching 2.0 mm/y at 20 wt% methanol. **Fig. 3.7**b shows that at 80°C CS corroded much more significantly (e.g., 7.2 mm/y in pure BO) than it did at 50 °C. A parabolic trend in the corrosion rate of CS was observed—the

corrosion rate increased with methanol concentration at first to a maximum value of 8.1 mm/y at 10 wt% methanol and then decreased with a further increase in methanol up to 20 wt% (6.8 mm/y). **Fig. 3.7**c presents the results of blank immersion tests of CS in water/methanol solutions at 80 °C and indicates that methanol itself did not have an adverse effect on CS corrosion. Weight loss of 304L and SS 316L coupons were negligible and not identified at 50 °C. At 80 °C, SS 304L corroded at a rate one order of magnitude lower (0.8 mm/y) than that of CS in pure BO and experienced a steady decrease in corrosion as methanol concentration was increased. SS 316L did not show any significant corrosion (< 0.1 mm/y) at 80 °C regardless of methanol concentration. Comparing the chemical composition of 304L and SS 316L from **Table 3.2**, it is believed that Mo and Ni play a more important role than Cr in resisting BO corrosion [32]. Based on the results of immersion experiments, storage and transportation of BO in CS tanks or pipelines at temperatures above 50 °C are not feasible [47]. SS 304L is commonly used for FCC injection nozzles [105], but experienced moderate corrosion when contacting BO at 80 °C in this study. This would put the serviceability of SS 304L in question when exposing it to BOs at higher temperatures. Although SS 316L showed negligible corrosion at tested temperatures, its performance at FCC feeding temperature (150–400 °C) needs to be further investigated [106, 107].
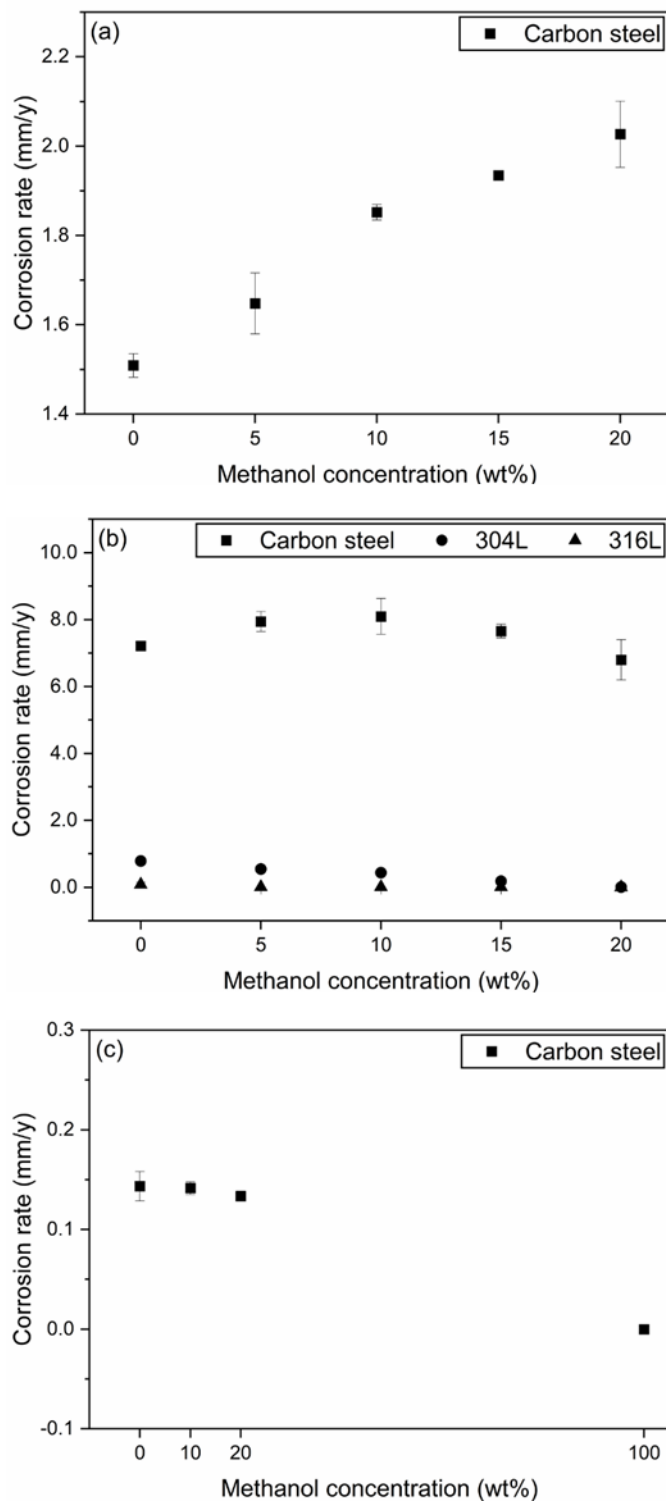
Fig. 3.7. Corrosion rates of metal coupons in pure BO and BO/methanol mixtures for 168 h: (a) carbon steel at 50 °C; and (b) carbon steel, 304L, and 316L at 80 °C. (c) Corrosion rates of carbon steel in water/methanol mixtures at 80 °C.

SEM and EDS techniques were employed to analyze the surface morphology and perform elemental composition analysis of surface products. **Fig. 3.8** depicts SEM surface images of the most corroded CS samples (based on **Fig. 3.7**a–b) from immersion tests at 50 °C (20 wt% methanol) and 80 °C (10 wt% methanol). The corresponding EDS maps of significant elements are also displayed in the bar chart. A rough surface is observed on both CS coupons. The sample immersed at 50 °C has an overall surface composition consisting mainly of Fe and significant amounts of C and O. The surface has several unique regions: a white area (location 1), which occupies most of the image and contains a large amount of Fe (~ 87 wt%), with the remaining composition split by C and O; a grey region (location 2), which contains a very large amount of C (~ 30 wt%) and O (~ 15 wt%), with much less Fe than location 1; and some black spots (location 3), which are scattered throughout the surface, are composed of 50 wt% C. Surprisingly, N was also identified at location 3, accounting for around 7 wt% of the total composition. The CS sample immersed at 80 °C appears very similar to its 50 °C counterpart. A majority of the surface is occupied by light regions (location 4), which are composed of more than 97 wt % Fe. Grey regions (location 5) contain approximately 60 wt% Fe, while the rest is split by C and O. Black areas (location 6) consist of large quantities of C, O and N. Based on the above observations, it is suspected that during immersion experiments, some BO and possibly BO–metal ion complexes were deposited on CS surfaces causing the abnormally high amounts of C and O over the entire areas and even the noticeable amount of N at some spots identified by EDS.
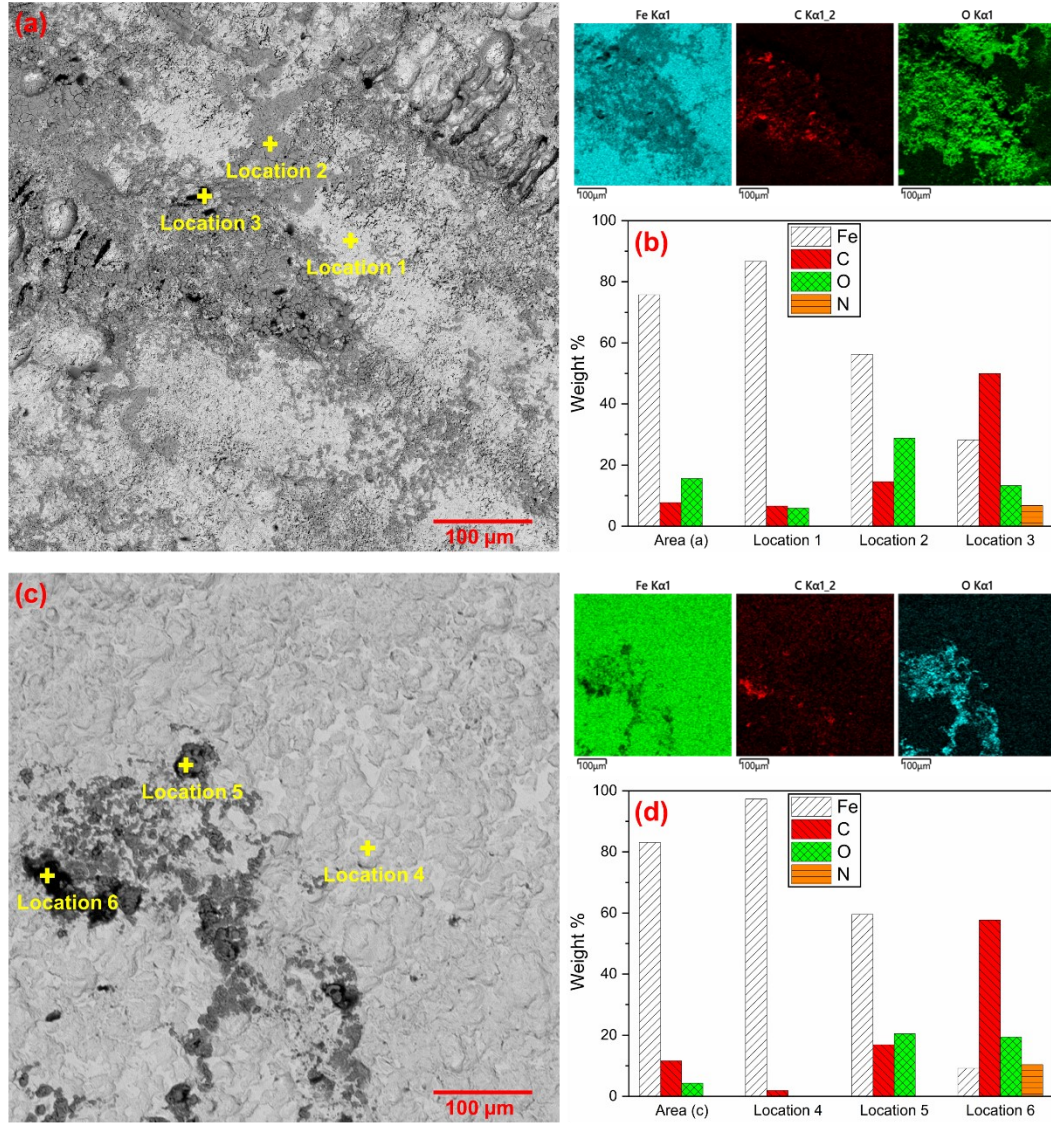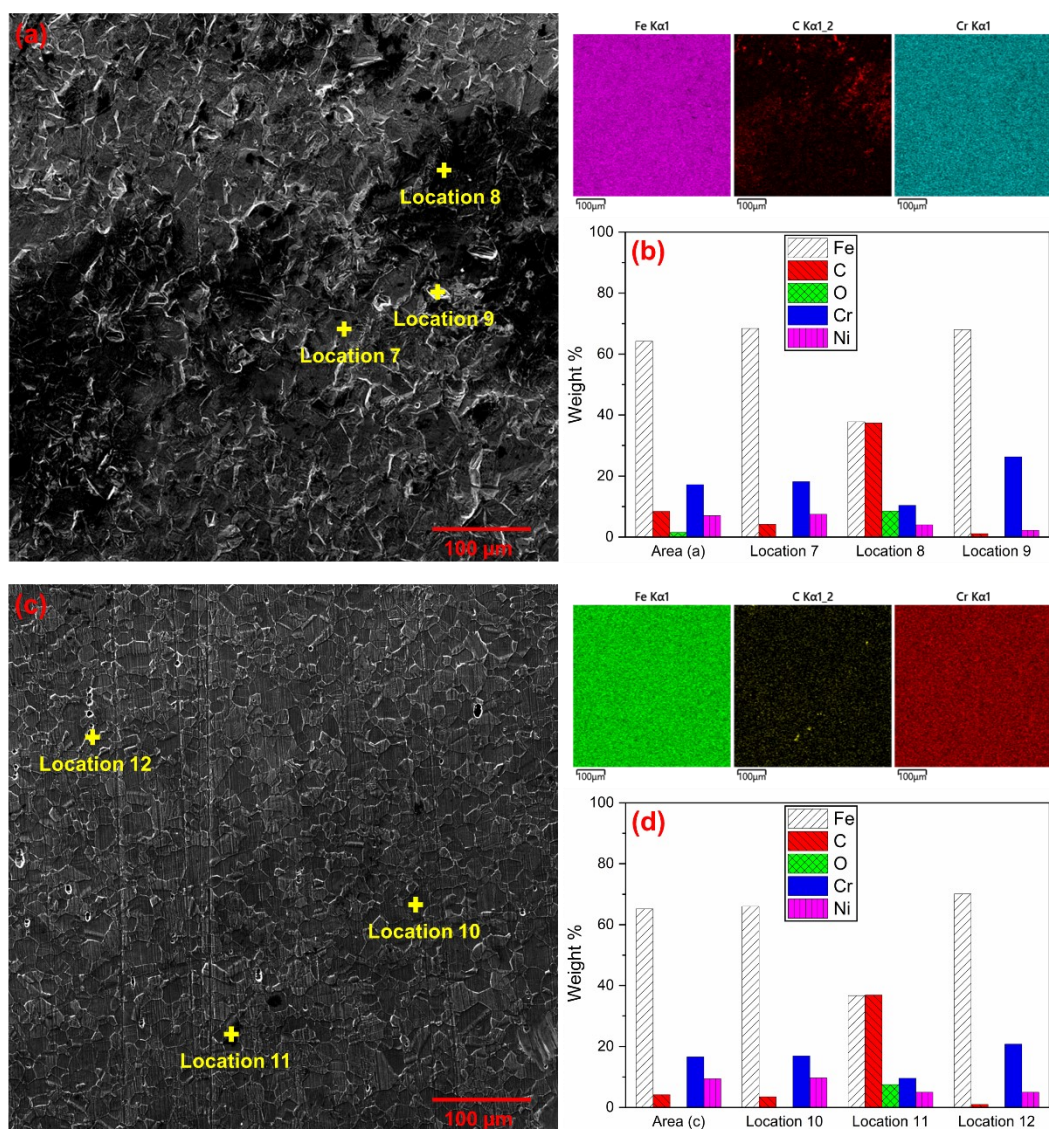
Fig. 3.8. SEM images and compositional mapping by EDS of carbon steel for the case with the highest corrosion rate plotted on **Fig. 3.6**a–b after immersion experiments for 168 h: (a–b) carbon steel in 20 wt% methanol BO mixture at 50 °C; and (c–d) carbon steel in 10 wt% methanol BO mixture at 80 °C.

SEM images, EDS surface maps and compositional charts for the most corroded sample of 304L and SS 316L (pure BO at 80 °C) are shown in **Fig. 3.9**. The surfaces of both SS samples appear smoother than that of CS. It is noticed that the grain boundaries of both samples are revealed in

these images, presumed to be the result of a higher rate of corrosive attacks by organic acids in BO at grain boundaries. Similar surface compositions are measured for 304L and SS 316L after immersion. Their entire surfaces compose mainly of Fe (> 60 wt%), with Cr and Ni at levels consistent with their original chemical compositions from **Table 3.2**. There are increased levels of C on the surface, and small traces of O, with more being measured on the SS 304L sample. This indicates that there were some BO residues deposited on the metal surface. Point compositions are analyzed within grains (locations 7 and 10), grain boundaries (locations 9 and 12) and distinct, dark spots (locations 8 and 11) for both SS samples. Within the grains of both samples (locations 7 and 10), Cr and Ni content are equivalent to their compositions across the entire area. However, large amounts of Cr (26 and 21 wt% for 304L and 316L SS, respectively) are detected along the grain boundaries (locations 9 and 12), whereas C and Ni contents have decreased. Equal amounts of Fe and C (~ 40 wt %) are detected in darker regions (locations 8 and 11), indicating there were some inclusions or carbides.

Fig. 3.9. SEM images and compositional mapping by EDS of stainless steels for the case with the highest corrosion rate plotted on **Fig. 3.6**b after immersion experiments for 168 h: (a–b) 304L in pure BO at 80 °C; and (c–d) 316L in pure BO at 80 °C.

To discriminate the effect of lixiviated metal ions on BO aging, the BO samples used in immersion tests with CS (denoted as immersed BO samples) were compared to BO samples employed in aging tests (denoted as aged BO samples) from the perspective of viscosity change. As indicated in **Fig. 3.10**, at 20 wt% methanol, there was no significant difference in viscosity between

immersed and aged BO samples after 168 h of heating. However, a discrepancy was observed between the viscosity of immersed and aged BO samples at lower methanol concentrations. For instance, after being heated at 50 °C for 168 h (**Fig. 3.10a**), the viscosity of immersed pure BO was 605 cP which is 3 times more viscous than would typically be observed in aged pure BO (227.5 cP). The discrepancy between immersed and aged BO samples declined after adding only 5 wt% methanol (157 vs. 136 cP) and kept decreasing as more methanol was added. For CS immersion tests at 80 °C, BO phase separation was observed in BO samples with below 15 wt% methanol. A thin phase with a viscosity of approximately 20 cP occupied the top layer, while a dense phase with extremely high viscosity settled to the bottom. For instance, after 168 h of aging, the viscosity of immersed pure BO was measured to be 64,500 cP which is one order of magnitude larger than the viscosity of the corresponding aged sample (2125 cP). Although the viscosity gap between immersed BO samples (lower phase) and aged BO samples narrowed with the increase of methanol concentration (0–15 wt%), the viscosity of the former was still one order of magnitude higher than that of the latter at the same methanol concentration (**Fig. 3.10b**). The above findings prove that CS and the corrosion of CS contribute to the overall aging of BO, especially in pure BO.
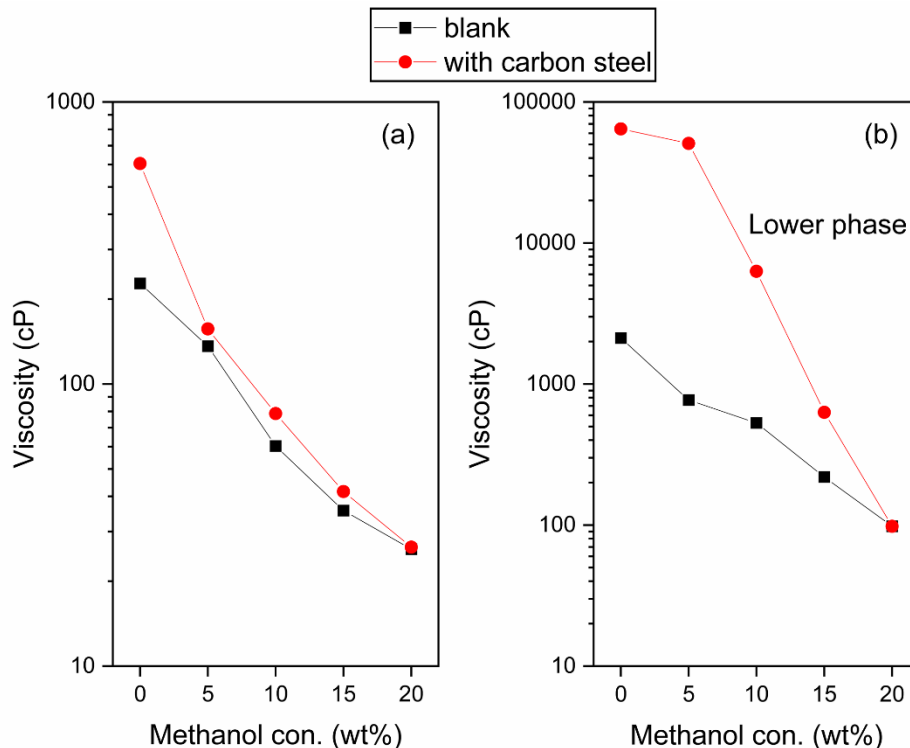
Fig. 3.10. Effect of lixiviated metal ions from carbon steel during immersion experiments on BO aging rate: (a) at 50 °C; and (b) at 80 °C.

Based on the results shown above, two phenomena require further investigation—abnormally high C, O, and N contents identified on metal surfaces; and extremely high viscosity measured for BOs containing CS samples. Chelation can be the potential mechanism to explain these unexpected behaviors. Chelation is a type of bonding composed of chelants (e.g., organic compounds) and a single central atom (i.e., metal atoms/ions) resulting in chelate complexes [108]. Previous studies have shown that large, oxygenated compounds (e.g., lactobionic acid) can form chelate complexes with surface metals and metal oxides that in turn accelerate corrosion [109-111]. Similarly, oxygenated compounds identified in BOs especially after aging (**Fig. 3.3**) could act as chelants to form organic molecule–metal complexes. For instance, hydroxyl groups of alcohols can bond with surface metal atoms via protonation. Besides, carbonyl oxygens of carboxylic acids can donate

lone electron pairs to metal cations near the surface [112]. As a result, a thin layer of chelate complexes tends to deposit and bind to the coupon surface that cannot be removed by rigorously cleaning in an ultrasonic bath, which also explains the increased levels of C, O and N observed in the EDS analysis (**Fig. 3.8** and **Fig. 3.9**). Chelate complexes resulted from surface leaching of metals by oxygenated compounds and bonding between lixiviated metal ions with chelants increased the viscosity of BO (**Fig. 3.10**). It is believed that chelate complexes also affect corrosion rates as discussed in the following.
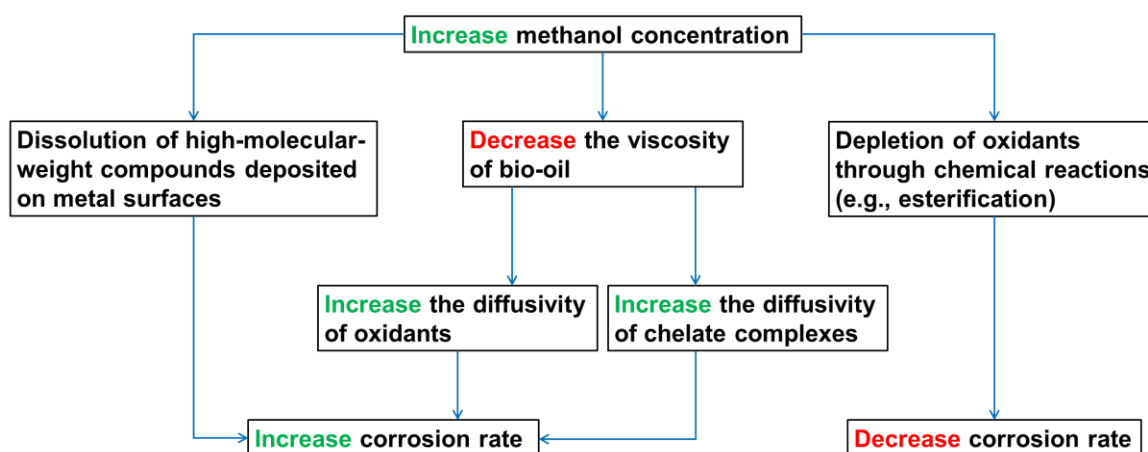
Fig. 3.11. Effects of methanol addition on the corrosion of steels in BO.

A mechanism is proposed and schematically illustrated in **Fig. 3.11** to explain the effect of methanol addition on the corrosion rate of steels in the tested BO samples. As discussed above, CS can substantially accelerate the BO viscosity increasing rate, making the viscosity of BO during CS corrosion a critical factor. An increase in BO viscosity will slow down the diffusivity of organic constituents in BO. For instance, oxidants will not reach the metal surface fast enough and chelate complexes near the metal surface will not be able to diffuse away as quickly from the uncorroded surfaces, both of which will slow down corrosion. During BO aging, a film of polymerized BO

may deposit on metal surfaces, decelerating corrosion. However, adding methanol lowers both the viscosity and the viscosity increase rate of BO, expedites the diffusion of oxidants, and chelate complexes, and allows for the dissolution of high-molecular-weight compound deposits. This explains why the corrosion rate of CS at 50 °C (0–20 wt%) and 80 °C (0–10 wt%) kept increasing as methanol concentration was increased. In contrast, reactions between methanol and oxidants (e.g., organic acids) will lower the concentration of oxidants, leading to a decrease in corrosion rate. For the CS corroding in BOs with 10–20 wt% methanol at 80 °C, the depletion of oxidants dominated over the viscosity effect, so the corrosion rate declined. The same reason can also explain why the corrosion rate of SS 304L decreased as methanol concentration was increased (0–20 wt%) at 80 °C.

3.4. Conclusions

The effect of adding methanol (5–20 wt%) on BO thermal stability was evaluated by performing a series of aging tests at 50 and 80 °C. Both GC–MS and TGA analyses indicated that during the BO aging process, light BO fractions were gradually converted into high-molecular-weight compounds. Adding methanol instantaneously lowered the viscosity, density, and water content, and increased the pH value of BO by physical dilution. Furthermore, the viscosity increasing rate of BO declined after adding methanol, considerably more during the aging at 80 °C than at 50°C, whereas adding methanol did not have a significant effect on the changing rates of density, water content, and pH value of BO.

The corrosivity of BO and BO/methanol mixtures was investigated by performing immersion experiments using common FCC structural steels at 50 and 80 °C for 168 h. Results showed that

CS corroded severely in all BO samples at both tested temperatures. At 50 °C, the corrosion rate of CS increased from 1.5 mm/y in pure BO to 2.0 mm/y in 20 wt% methanol BO, indicating that adding methanol could accelerate the corrosion of CS. At 80 °C, the corrosion rate of CS increased initially (7.2 mm/y in pure BO) until reaching a maximum value at 10 wt% methanol BO (8.1 mm/y) and then decreased (6.8 mm/y in 20 wt% methanol BO). SS 304L did not corrode in BO samples at 50 °C but corroded at a moderate rate at 80 °C (< 1 mm/y). SS 316L was corrosion-resistant to BO samples at both temperatures (< 0.1 mm/y). The immersion experiments concluded that CS is not suitable for storing and processing BOs at temperatures higher than 50 °C, and cautions must be taken when directly exposing SS to BOs, especially at high temperatures.

In summary, although adding methanol generated promising results in improving BO stability, it can be detrimental from the perspective of corrosion. Interestingly, BO mixtures containing CS experienced a phase separation and achieved viscosity values an order of magnitude higher than their aged counterparts. SEM and EDS analysis indicated high levels of C, O and N on CS surfaces after immersion. These results suggest the formation of chelate complexes on CS coupons. Further investigation is necessary to elucidate attack mechanisms and to guide future process optimization and materials selection for BO co-processing.

Chapter 4. Electrochemical Corrosion Study of Carbon Steel in Bio-oil Environments

Abstract

Comprehensive corrosion risk assessments are essential for ensuring the safe and efficient utilization of bio-oil (BO) in industrial applications. In this study, electrochemical measurements (EMs) such as potentiodynamic polarization (PDP) and electrochemical impedance spectroscopy (EIS) were conducted for carbon steel (CS) at BO storage temperatures of 20 and 50 °C. Different electrolytes were used, including BO, BO+10 wt% methanol (10ME), BO+20 wt% methanol (20ME), and 0.1 M acetic acid (0.1AC). To improve data quality in low-conductive environments, various techniques were employed for EMs. Concurrent immersion experiments (IEs) were performed to validate corrosion rate (CR) calculations obtained from EMs. The PDP results revealed uniform corrosion as the prevalent form of CS corrosion in BO environments, while EIS measurements indicated the involvement of adsorption/chelation processes. A well-fit equivalent circuit model was proposed for EIS data. The ratios between CRs obtained from EMs and IEs were around 4.3 and 0.9 at 20 and 50 °C, respectively, for all electrolytes, confirming the reliability of EMs for evaluating CS corrosion in BO environments. This study provides valuable insights into corrosion assessments of structural alloys in BO environments using reliable yet inexpensive EM techniques.

Keywords: Bio-oil; Carbon Steel; Corrosion; Potentiodynamic Polarization (PDP); Electrochemical Impedance Spectroscopy (EIS)

4.1. Introduction

Expanding the utilization of abundant biomass would enhance energy security, reduce energy costs, and mitigate greenhouse gas emissions [113, 114]. Biomass such as agricultural wastes and wood can be converted to liquid bio-oil (BO) via thermochemical processes (e.g., fast pyrolysis and hydrothermal liquefaction) [115-117]. However, BO presents challenges due to its high corrosivity, low heating value and thermal instability, necessitating further upgrading [34, 45, 100]. To address these challenges, co-processing BO with vacuum gas oil (a petroleum intermediate) utilizing existing fluid catalytic cracking units has emerged as a promising and cost-effective approach to convert low-quality BO to renewable drop-in fuels (e.g., gasoline, diesel, and jet fuel) [66, 118-120]. **Fig. 4.1** illustrates the BO co-processing strategy and highlights the corrosion risks posed by BO to structural alloys throughout the BO processing stages. Before implementing BO co-processing, it is crucial to thoroughly understand the corrosion risks associated with BO production, transportation, storage, and upgrading.
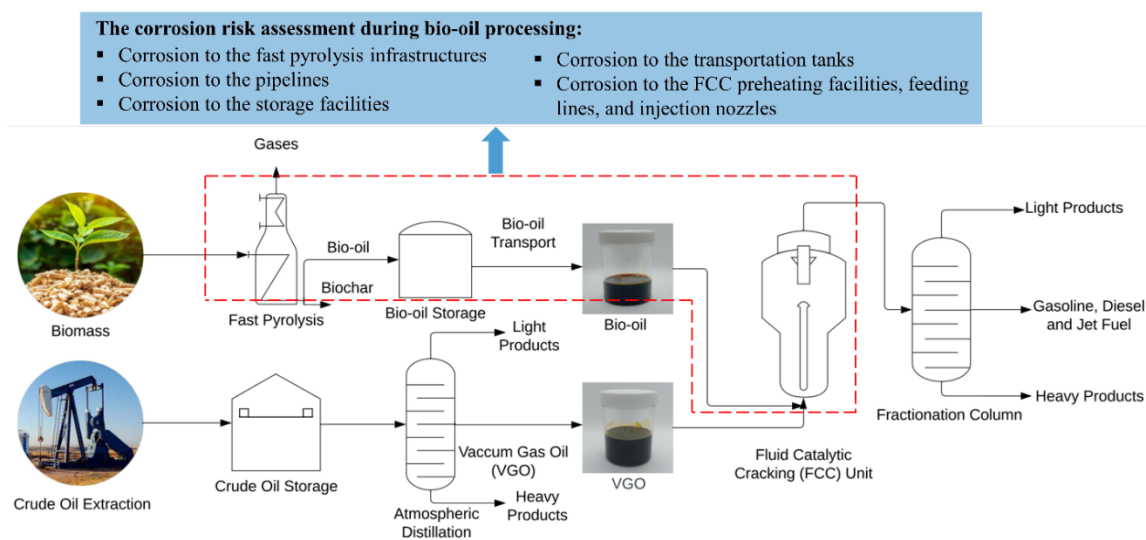
Fig. 4.1. Schematics of the bio-oil co-processing strategy and the corrosion risk assessment during bio-oil processing.

Immersion experiments (IEs) are commonly employed to evaluate metal corrosion by submerging metal coupons in corrosive environments for a period of time and recording the weight change before and after IEs. The corrosion rate (CR) obtained from IEs provides a direct indication of the average intensity of metal corrosion during the immersion period. Extensive research has been conducted to investigate the corrosivity of BO towards structural alloys using IEs under various conditions. For instance, Keiser et al. [47, 48] studied the corrosion of carbon steel (CS), 2.25Cr-1Mo steel, and type 409, 304L, and 316L stainless steels (SS) in BO from various biomass sources at 50 °C. The IE results showed significant weight loss and uniform corrosion for CS and 2.25Cr-1Mo steel (CR > 0.1 mm/y), while minimal weight loss was observed for the SS specimens [49]. Adding methanol into bio-oil has been proven to be effective in mitigating bio-oil aging [35, 36]. Wang et al. [121] conducted IEs for CS and SS 304L and 316L in BO with the addition of up to 20 wt% methanol (ME) at 50 and 80 °C. The results showed that the CR of CS increased with increasing methanol concentration at 50 °C, whereas the CR of CS peaked in BO with 10 wt% methanol at 80 °C. The CRs of CS were over 1 mm/y and 6 mm/y in BO at 50 and 80 °C, respectively. SS 304L experienced a moderate CR (<1 mm/y) at 80 °C, while SS 316L exhibited minimal corrosion (CR< 0.1 mm/y). Therefore, excessive corrosion of CS demands careful attention during BO processing to ensure the safety of the operation. Further investigation is required to understand the mechanisms underlying steel corrosion in BO environments.

Meanwhile, electrochemical measurements (EMs) offer a simpler, quicker, and more cost-effective way of quantifying the corrosion response of alloys compared to IEs [50]. For instance, potentiodynamic polarization (PDP) and electrochemical impedance spectroscopy (EIS) methods have been widely used to study the corrosion behavior of metals in various media [122, 123].

These techniques involve applying controlled electrochemical disturbances to detect the response of the charge transfer process, thus revealing the corrosion behavior of metals. Nevertheless, the utilization of EMs in studying corrosion in BO environments is restricted, mainly due to the challenges posed by the low conductivity of BO, resulting in inferior data quality. Consequently, conducting research in such complex electrolytes demands meticulous experimental design and data interpretation.

Some researchers have adopted EMs to investigate steel corrosion in BO environments. Jun et al. [56] performed EIS measurements for 2.25Cr-1Mo and 9Cr-1Mo steels and SS 410 and 430 in selected organic constituents of BO at room temperature. The electrolytes used include 0.1 M catechol, formic acid, their mixtures, and lactobionic acid in the solvent of 85 wt% deionized (DI) water + 15 wt% ME. A Randle circuit, comprising the solution resistance, a constant phase element (CPE), and the charge transfer resistance (R_{ct}), was used to fit the EIS results. The obtained R_{ct} results were used to evaluate the corrosion susceptibility of each steel in the studied environments. The authors concluded that the two SS with high R_{ct} values (> 100 kohm·cm^2) exhibited high corrosion resistance in all tested environments, while 2.25Cr-1Mo steel with low R_{ct} values (< 3 kohm·cm^2) demonstrated severe corrosion. 9Cr-1Mo steel only displayed corrosion resistance to the 0.1M catechol environment (R_{ct} > 300 kohm·cm^2).

Later, Jun et al. [124] studied the corrosion performance of 2.25Cr-1Mo steel and SS 430 and 430F in BO at room temperature via EIS measurements. The same Randel circuit mentioned above was used for EIS fitting. Results indicated that the R_{ct} value of each alloy increased over time, indicating a gradual reduction in the CR. The R_{ct} data of SS were at least 2 orders of magnitude

higher than that of 2.25Cr-1Mo steel. It was concluded that BO was corrosive to steels with a low Cr content.

To the authors' best knowledge, corrosion investigations concerning structural alloys in BO environments using EMs have only been conducted at room temperature [125-127]. Direct calculation of CRs from EMs for metals has not been performed. Therefore, a comparison between corrosion data obtained from IEs and EMs becomes essential to validate the applicability of EMs in BO environments and to justify the equivalent circuit model (ECM) used for interpreting EIS results.

As discussed above, a comprehensive understanding of carbon steel corrosion in BO environments is essential for the safety of BO operations. The assessment of BO corrosivity using EMs requires further refinement and validation. In this study, we proposed modified EM techniques, encompassing open circuit potential (OCP), PDP, Tafel scans, and EIS, to study the corrosion of CS in BO at storage temperatures of 20 and 50 °C. In addition, 10 and 20 wt% ME were added into BO to study the effect of ME addition on CS corrosion. For comparison, EMs were also conducted using 0.1 M acetic acid in DI water, with the same pH as BO. To validate the CR data obtained from EMs, parallel IEs were carried out.

4.2. Experimental Setup

4.2.1. Electrolytes and the Target Steel

A BO (BTG Bioliquids) converted from pinewood by fast pyrolysis was used in this study. The properties of BO can be found elsewhere [121, 128]. BO was also blended with 10 and 20 wt%

ME. Additionally, 0.1M acetic acid in DI water, denoted as 0.1AC, was used for comparison. **Table 4.1** lists the composition of electrolytes used in this study. Notably, BO had the same pH as 0.1AC, while the viscosity of the former was two orders of magnitude higher than the latter. Compared to pure BO, the pH and viscosity of BO/ME mixtures (such as 10ME and 20ME) increased and decreased, respectively, with the concentration of ME. The corrosion study used a common structural CS widely employed for bio-oil processing, and its composition can be found elsewhere [121].

Table 4.1. The composition of electrolytes used in this study.

Code name	Composition	pH	Viscosity (cP)
BO	100 wt% BO	2.8	172
10ME	90 wt% BO + 10 wt% ME	3.1	49
20ME	80 wt% BO + 20 wt% ME	3.4	20
0.1AC	0.1 M AC in DI water	2.8	around 1

4.2.2. Electrochemical Measurements (EMs)

The potentiostat used for EMs was a Princeton Applied Research Versastat 4 potentiostat. CS specimens were mounted in epoxy resin with an exposed surface area of 0.4 cm^2 serving as the working electrode (WE). The specimens were polished using SiC papers to a 600-grit finish, rinsed with DI water, and air-dried. A platinum mesh and a RE-7 non-aqueous reference electrode (Ag/Ag$^+$) (ALS Co., Ltd 012171) (0.345 V vs. Ag/AgCl saturated KCl electrode) were used as the counter electrode (CE) and the reference electrode (RE), respectively. A water bath was connected to a water-jacketed cell to control the electrolyte temperature.

Since the electrolytes used in this study were low-conductive, efforts had been made to improve data acquisition. Instead of adopting a traditional three-electrode setup, a four-electrode setup was used in this study as shown in **Fig. 4.2**. In a traditional three-electrode setup, the working sense (WS) wire is shorted with the WE wire. In order to improve the electrical transfer, the WS wire in the current setup was separated from the WE wire for potential control between RE and WE. In addition, WE/CE and RE/WS were paired by twisting the wires to reduce the electromagnetic field thus minimizing the inductance of cell cables (**Fig. 4.2**). All EMs were conducted in a Faraday shield to minimize electromagnetic interference outside of the system.
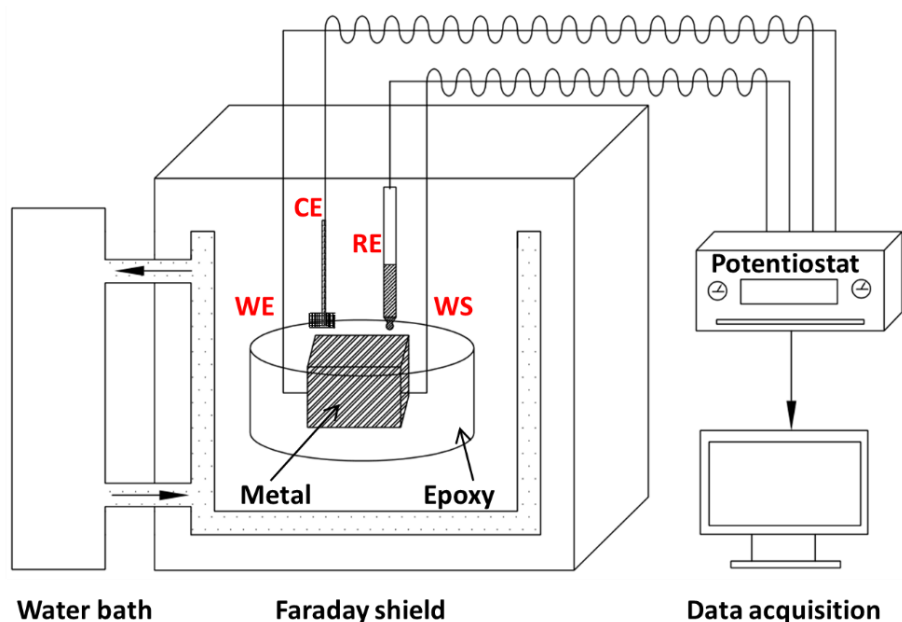
Fig. 4.2. Schematics of the four-electrode EM set-up.

EMs were conducted as follows at 20 and 50 °C: (1) OCP measurements were carried out for at

least 1 h to let the system reach a steady state; (2) EIS experiments were conducted afterwards (repeat for 3 times), where the frequency range and amplitude for EIS measurements were set as 0.1 Hz–1000 Hz and ±5 mV against OCP, respectively; (3) PDP measurements were performed from -0.25 V vs. OCP to +1.6 V vs. Ref. with a scan rate of 0.167 mV/s; (4) Tafel scans were conducted separately with a new CS specimen from -0.15 V vs. OCP to +0.15 V vs. OCP (repeat for 3 times) with a scan rate of 0.167 mV/s. For each condition, at least two trials of experiments were performed.

4.2.3. Immersion Experiments (IEs)

Parallel with EMs, IEs following the procedures of ASTM G31 [94] were conducted for CS strip coupons ($1 \times 1/4 \times 1/16$ in^3) in the electrolytes mentioned above (**Table 4.1**) at 20 and 50 °C for 168 h and with 4 coupons for each condition. CRs of CS were calculated using weight loss data. The detailed setup can be found elsewhere [121]. After IEs, an optical microscope was used to observe the surface morphology of corroded CS coupons. X-ray diffraction (XRD) and X-ray photoelectron spectroscopy (XPS) analyses were performed for CS coupon surface characterization. The XRD analysis was conducted to determine the corrosion products by using an X-ray diffractometer (Rigaku XRD Ultima IV) with a Cu X-ray source and a scanning speed of 1°/step. The chemical states of the elements on the metal surface were measured by an XPS spectrometer (Kratos AXIS Ultra) with Al Kα excitation. The XPS binding energies are calibrated to the C 1s spectra at 284.8 eV.

4.3. Results and Discussion

4.3.1. PDP Measurements

Fig. 4.3 shows the polarization curves generated from PDP measurements. The reported potentials were against an Ag/AgCl saturated KCl electrode. At 20 °C, the corrosion potentials of CS in BO/ME mixtures were around -0.43 V, while the corrosion potential in 0.1AC was -0.59 V (**Fig. 4.3a**). The corrosion potentials of CS in all electrolytes stayed at a narrow range between -0.39 to -0.45 V at 50 °C (**Fig. 4.3b**). As indicated in **Fig. 4.3**, the anodic branches exhibited active corrosion with no passivation region identified. This suggests that the corrosion form of CS was uniform corrosion, indicating a lack of susceptibility to pitting corrosion in all studied environments, which agrees with previous findings [49, 121]. The anodic branches shifted to the right (higher anodic current density at a fixed potential) in the following order: BO < 10ME < 20ME < 0.1AC at both temperatures (denoted by the green dashed arrows). Such observation suggested that the corrosion intensity of CS increased in the same order. According to previous studies, the CR of CS is expected to be higher in BO/ME mixtures with a higher concentration of ME (up to 20 wt% ME) [121]. This could be attributed to the increase of diffusivity of corrosive species in BO/ME mixtures as adding ME dilutes BO (*i.e.*, lower viscosity). Although ME addition in BO slightly increases the pH due to dilution, the diffusivity effect dominates especially at low temperatures (less than 50 °C) [121]. Due to the same reason, amongst the electrolytes in **Table 4.1**, 0.1AC (low pH and viscosity) is expected to be the most corrosive environment to CS. For each electrolyte, as temperature increased, the anodic branch moved to the right suggesting the CR of CS increased with temperature. Although not discussed here for brevity, Tafel curves exhibited similar features to the PDP curves. The Tafel slopes obtained from Tafel scans were used for CR calculations, which will be discussed later.
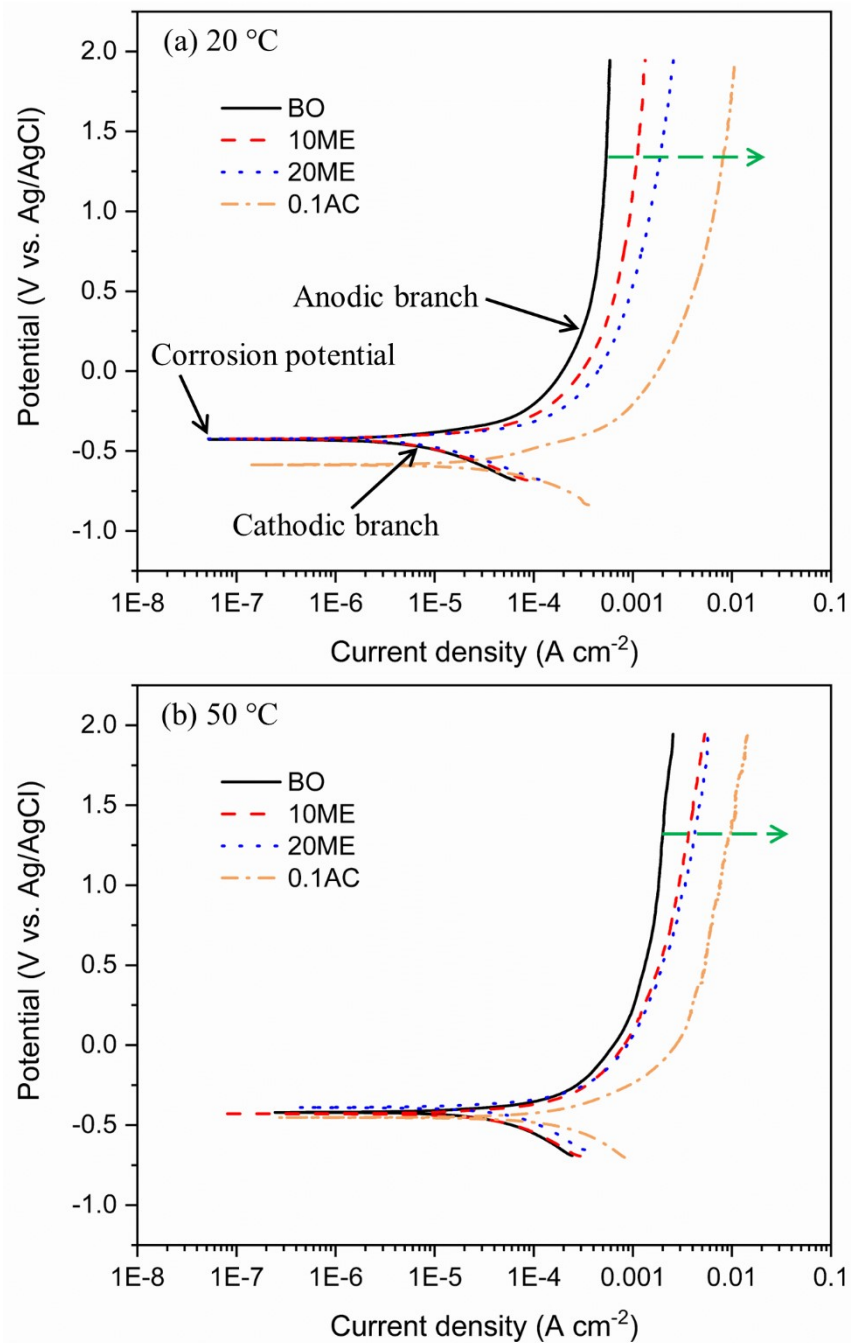
Fig. 4.3. PDP curves for CS in BO, 10ME, 20ME, and 0.1AC environments at: (a) 20 °C; and (b) 50 °C.

4.3.2. EIS Measurements

4.3.2.1. Nyquist Plots

The EIS measurements were conducted after OCP, at which the system was stabilized (*i.e.*, the resting potential between RE and WE fluctuates less than ±5 mV over a long period of time). At 20 °C, the system became stabilized within 1 h, thus the EIS measurements were conducted at 1, 4, and 11 h. As it took a long time for the system to be stabilized at 50 °C (around 10 h), the EIS measurements were only conducted at 11 h for this temperature. **Fig. 4.4** presents the Nyquist plots obtained from EIS measurements. As indicated in **Fig. 4.4a**, the Nyquist plots measured at 1, 4, and 11 h were composed of semi-arcs across the frequency range of 1000–0.1 Hz at 20 °C. The starting point of each semi-arc (from left at 1000 Hz) represented the electrolyte/solution resistance. Thus, the solution resistance from high to low followed the order of BO, 10ME, 20ME, and 0.1AC, which coincided with the order of solution viscosity from high to low (**Table 4.1**). Solution resistance and viscosity are inversely related to the ease of ion diffusion within the solution, which is relevant to the corrosion process involving ion transfers. Generally, within a certain pH range, metals tend to corrode more extensively in electrolytes with lower solution resistance (lower viscosity). Besides, as shown in **Fig. 4.4a**, the real impedance (Z_{re}) of BO at 1000Hz increased notably from 1.88 kohms·cm^2 at 1h to 2.09 kohms·cm^2 at 11h. This was attributed to the increase in BO viscosity caused by the bonding between leached metal ions and organic molecules in BO during CS corrosion. Yet, the changes in the Z_{re} of 10ME and 20ME were subtle due to the addition of ME reducing the aging of BO caused by metal corrosion, aligning with the previous findings [121]. Additionally, it can be observed in **Fig. 4.4a** that the diameter of the semi-arcs for each electrolyte increased over time, indicating that the CR of CS was initially fast and gradually slowed down. This is consistent with the general corrosion process for uniform

corrosion. Initially, the CR is relatively high, then it gradually decreases due to the depletion of corrosive species and the formation of corrosion product layers on metal surfaces. The Nyquist plots obtained at 50 °C (**Fig. 4.4b**) exhibited similar features to those measured at 20 °C. The diameters of the semi-arcs (representing the charge transfer resistance) decreased in the order of BO, 10ME, 20ME, and 0.1AC, indicating an expected increase in the CR of CS in the same order.
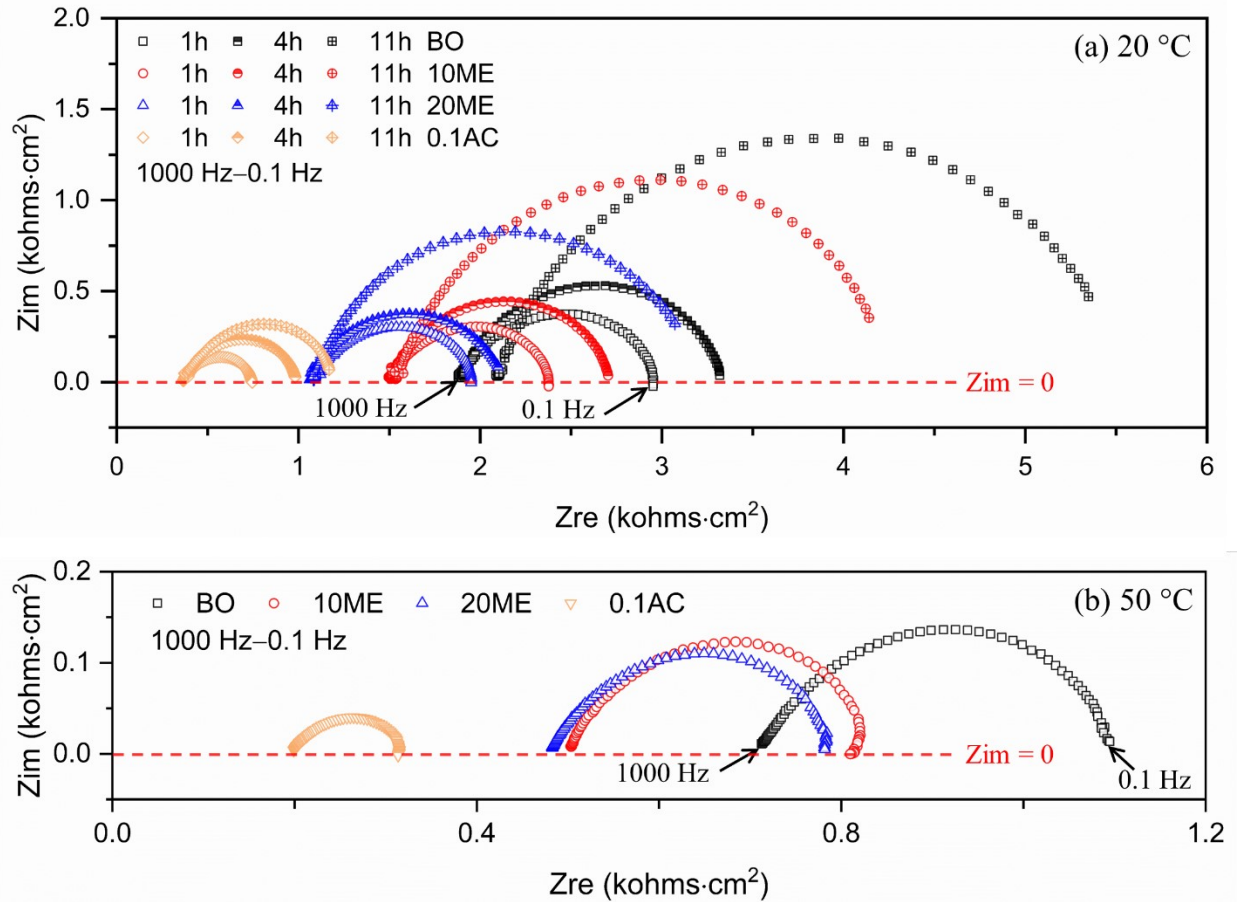
Fig. 4.4. Nyquist plots for CS in BO, 10ME, 20ME, and 0.1 AC Environments: (a) at 20 °C after 1, 4 and 11 h; and (b) at 50 °C after 11 h.

Notably, some data points of the imaginary impedance (Z_{im}) in the low-frequency region were below 0, as shown in **Fig. 4.4**. This phenomenon has been observed in EIS measurements of

various types of steel in BO environments. Jun et al. [124, 129, 130] performed EIS experiments on 2.25Cr-1Mo, 9Cr-1Mo, and SS416 steels in BO environments at room temperature, where incomplete loops (negative Z_{im}) were formed in the low-frequency region. Similar features were also observed in EIS studies of steel corrosion in crude oil environments [131]. The appearance of a second loop below the semicircle can be attributed to an inductive response, indicating the involvement of an adsorption mechanism [132, 133]. Such phenomena are commonly observed when chemical species, ions, or molecules are adsorbed at the interface of the electrical double layer (EDL). For instance, some EIS measurements presented inductive loops when corrosion inhibitors were added to the electrolytes [134-136]. The presence of organic inhibitor molecules formed a barrier layer on the metal surface, providing protection for steels under aggressive conditions. The adsorption process of corrosion inhibitors leads to the inductive response observed in the Nyquist plots. There are two kinds of adsorption pathways: physical adsorption, which occurs through electrostatic interactions between charged organic molecules and charged metal surfaces; and chemical adsorption, where donor-acceptor interactions take place between free electron pairs and vacant of heteroatoms (e.g., nitrogen and oxygen) and metal's low energy d-orbitals [137]. The chemical adsorption process is similar to chelation, involving bonding between ions, molecules, and metals to form chelate complexes. Previous studies have shown that organic molecules in BO would chelate with surface metals and metal oxides [112, 121]. Nyquist plots obtained in this study (**Fig. 4.4**) further support the presence of electrical inductance resulting from the adsorption/chelation of organic compounds with metals during CS corrosion in BO. This aspect was considered during the fitting of EIS data, as discussed below.

4.3.2.2. Bode Plots and the Equivalent Circuit Model (ECM)

The ECM used for fitting the EIS results is shown in **Fig. 4.5a**. The ECM ($R_s(LR_f)(QR_{ct})$) consists of the solution resistance (R_s), inductance due to chelation (L), resistance associated with the chelate complex exchanging layer (R_f), capacitance modelled by a constant phase element (CPE, also represented by Q), and R_{ct}. The schematics interpreting the components of the ECM are presented in **Fig. 4.5b**. The EIS data were fitted using the ZSimpWin (AMETEK), and the resulting data of the measured impedance (|Z|_msd), calculated impedance (|Z|_cal), measured phase angle (Angle_msd), and calculated phase angle (Angle_cal) were plotted against the frequency. **Fig. 4.6** and **Fig. 4.7** illustrate the Bode plots for the EIS measurements conducted at 20 and 50 °C, respectively. The fitting parameters are summarized in **Table 4.2**. Overall, the calculated data closely overlapped with the measured data (as indicated in **Fig. 4.6** and **Fig. 4.7**). The chi-square (χ^2) values ranged from 10^{-6} to 10^{-4}, and the percentage error of R_{ct} was between 0.66%–5.16%, indicating that the ECM effectively fitted the EIS data. The overall impedance (|Z|) for all cases shown in **Fig. 4.6** and **Fig. 4.7** exhibited a trend of plateau-decline-plateau, corresponding to a phase shift at the intermediate frequencies (around 1–10 Hz). At both temperatures, the |Z| decreased in the order of BO, 10ME, 20ME, and 0.1AC. At 20 °C, for each electrolyte, the |Z| values at 11 h (**Fig. 4.6b**) were higher than those at 1 h (**Fig. 4.6a**). In addition, the |Z| measured at 50 °C (**Fig. 4.7**) was lower than that at 20 °C (**Fig. 6b**) for each electrolyte. These findings align with the conclusions obtained from the Nyquist plots (**Fig. 4.4**).
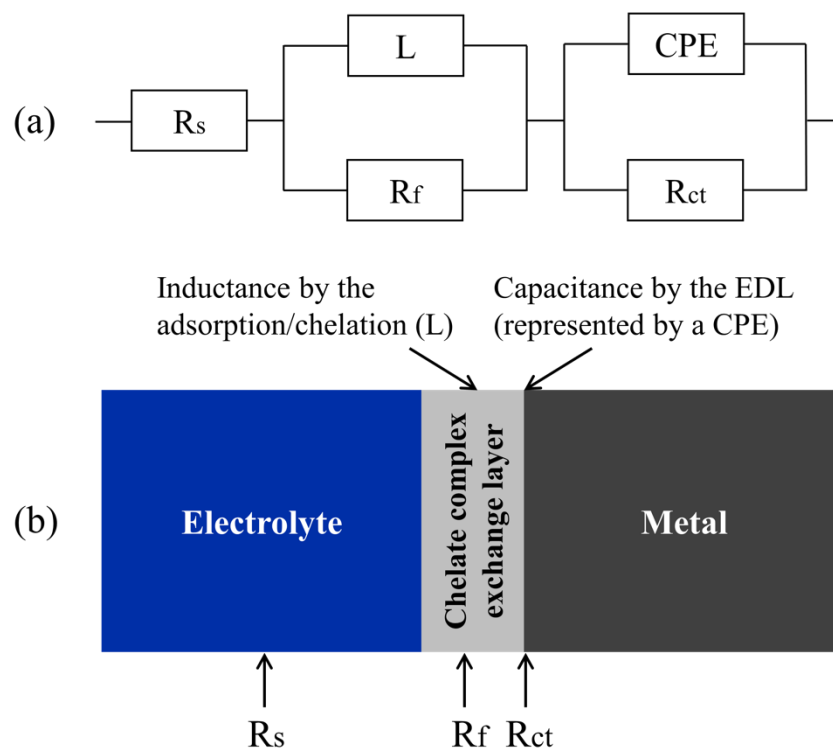
Fig. 4.5. (a) The equivalent circuit model used for EIS data fitting; and (b) schematics of the corrosion mechanism.
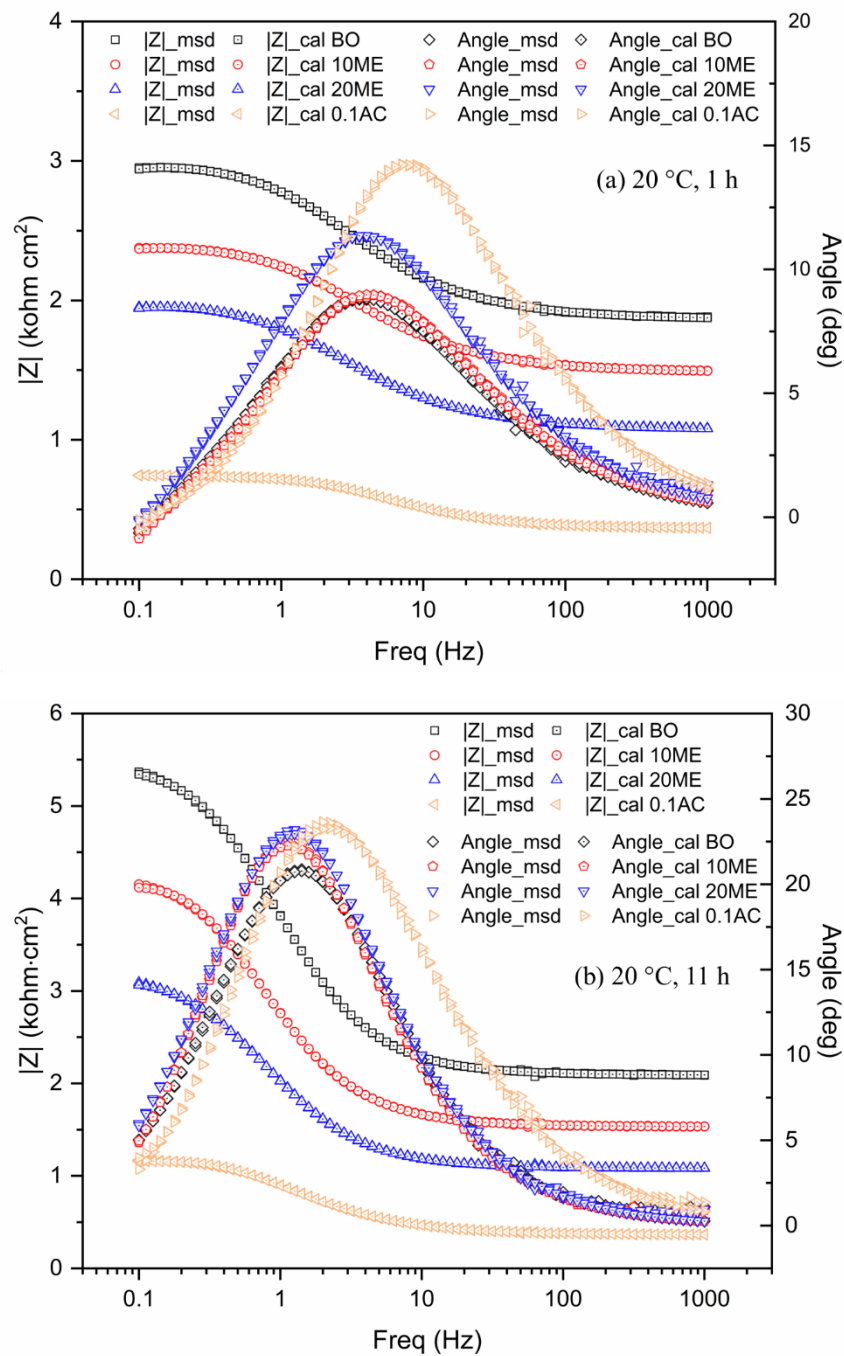
Fig. 4.6. Bode plots for CS at 20 °C: (a) after 1 h; and (b) after 11 h.
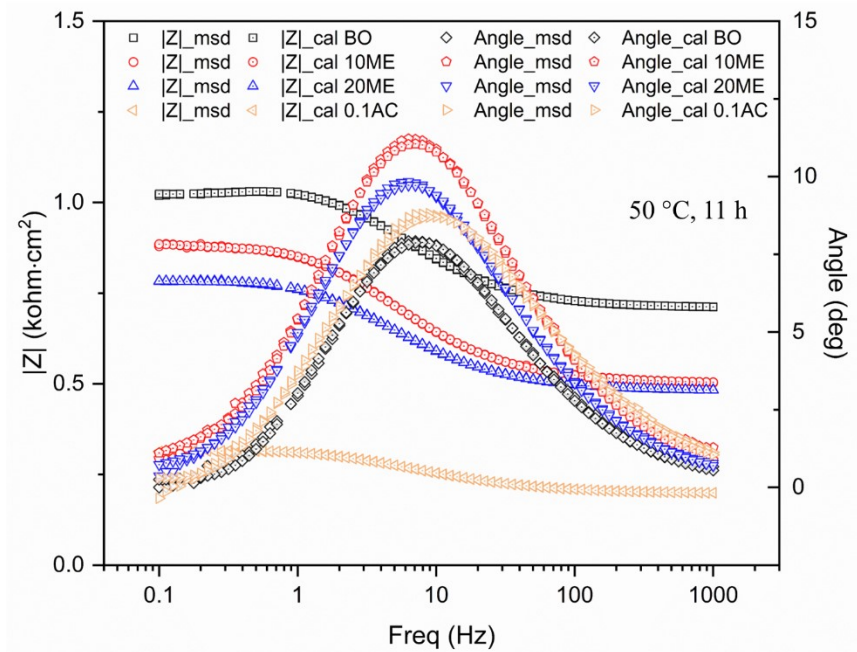
Fig. 4.7. Bode plots for CS at 50 °C after 11 h.

Table 4.2. Parameters of EIS fitting results.

Sol.	T (°C)	t (h)	R_s (kohms·cm²)	L (kH·cm²)	R_f (kohms·cm²)	Q_{dl}-Y_o ×10⁻³ (S·sⁿ/cm²)	Q_{dl}-n	R_{ct} (kohms·cm²)	χ^2 ×10⁻⁵	% error R_{ct}
BO		1	1.57	0.96	0.49	0.13	0.67	1.11	2.98	1.25
	20	4	1.52	1.95	0.38	0.09	0.78	1.51	3.57	0.90
		11	1.81	0.37	2.78	0.08	0.82	3.70	5.15	2.65
	50	11	0.65	0.02	0.06	0.19	0.80	0.47	0.57	0.95
10ME		1	1.28	0.46	0.21	0.12	0.71	0.98	1.77	0.84
	20	4	1.22	1.07	0.28	0.13	0.77	1.30	1.72	0.70
		11	0.88	0.91	0.07	0.11	0.81	3.34	3.22	2.89
	50	11	0.45	0.01	0.00	0.22	0.80	0.44	1.31	1.47
20ME		1	0.88	0.46	0.32	0.18	0.66	0.85	2.69	3.95
	20	4	0.71	2.42	0.34	0.10	0.79	1.10	3.66	0.66
		11	0.85	0.45	0.23	0.14	0.82	2.29	4.76	2.15
	50	11	0.48	1.35	0.34	0.26	0.80	0.41	0.76	1.96
0.1AC		1	0.32	0.02	0.43	0.18	0.80	0.42	4.72	1.28
	20	4	0.23	0.08	0.14	0.25	0.74	0.78	7.86	2.96
		11	0.06	0.26	0.31	0.29	0.73	1.18	11.7	5.16
	50	11	0.18	0.01	0.02	0.60	0.80	0.14	1.33	1.00

4.3.2.3. Corrosion Rate (CR) Calculations

The R_{ct} results, inversely related to the CR of CS, were summarised in **Fig. 4.8**. BO exhibited the highest R_{ct} value, indicating the lowest CR among the tested electrolytes, while 0.1AC had the lowest R_{ct} value, corresponding to the highest CR. The R_{ct} value decreased with increasing ME concentration in BO, indicating that the ME addition would accelerate CS corrosion in BO at studied temperatures [121]. The addition of ME enhanced the diffusivity of corrosive species, leading to more aggressive corrosion of CS. At 20 °C, the R_{ct} value increased over time (at 1, 4, and 11 h), showing a slowdown in corrosion over time. The R_{ct} value obtained at 50 °C was lower than that at 20 °C at 11 h, indicating an acceleration of corrosion with increasing temperature.
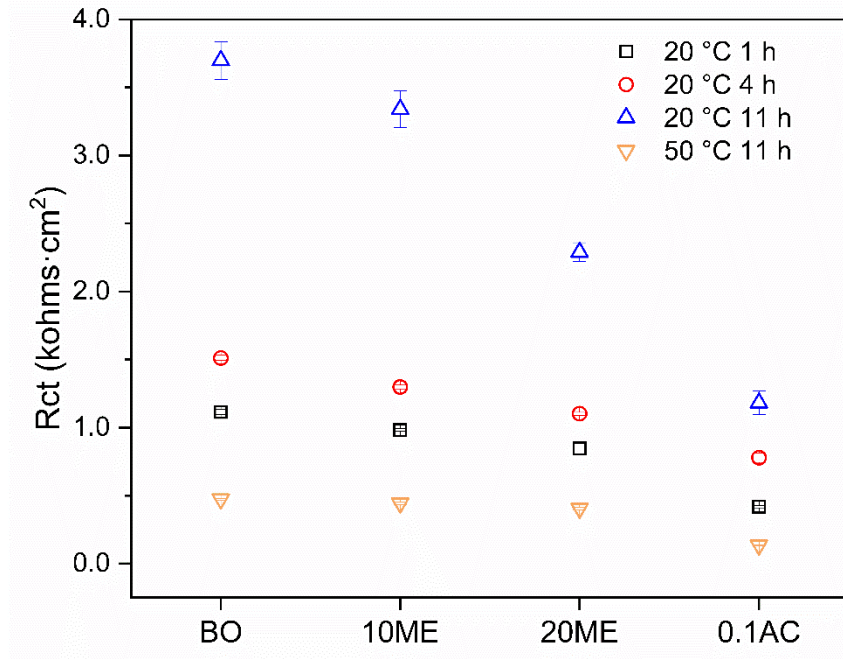
Fig. 4.8. A summary of R_{ct} values for CS at 20 and 50 °C obtained from EIS fittings.

The corrosion current density (i_{corr}, $\mu A/cm^2$) was calculated by **Equation (4.1)** as shown below, considering R_{ct} (kohm·cm^2, **Table 4.2**) and Tafel slopes (β_a, β_c, V/decade, **Table 4.3**). The calculated i_{corr} data at 11 h for both 20 and 50 °C are presented in **Fig. 9a**. The i_{corr} showed an inverse relationship with R_{ct} (**Fig. 4.8**) and increased in the order of BO, 10ME, 20ME, and 0.1AC.

$$i_{corr} = \frac{10^3 \beta_a \beta_c}{2.3 R_{ct}(\beta_a + \beta_c)}$$

Equation (4.1)

Table 4.3. Tafel slopes obtained from Tafel scans at 11 h.

Sol.	T (°C)	β_a (V/decade)	β_c (V/decade)
BO	20	0.201	0.181
	50	0.276	0.276
10ME	20	0.227	0.148
	50	0.265	0.280
20ME	20	0.216	0.141
	50	0.276	0.283
0.1AC	20	0.195	0.204
	50	0.237	0.291
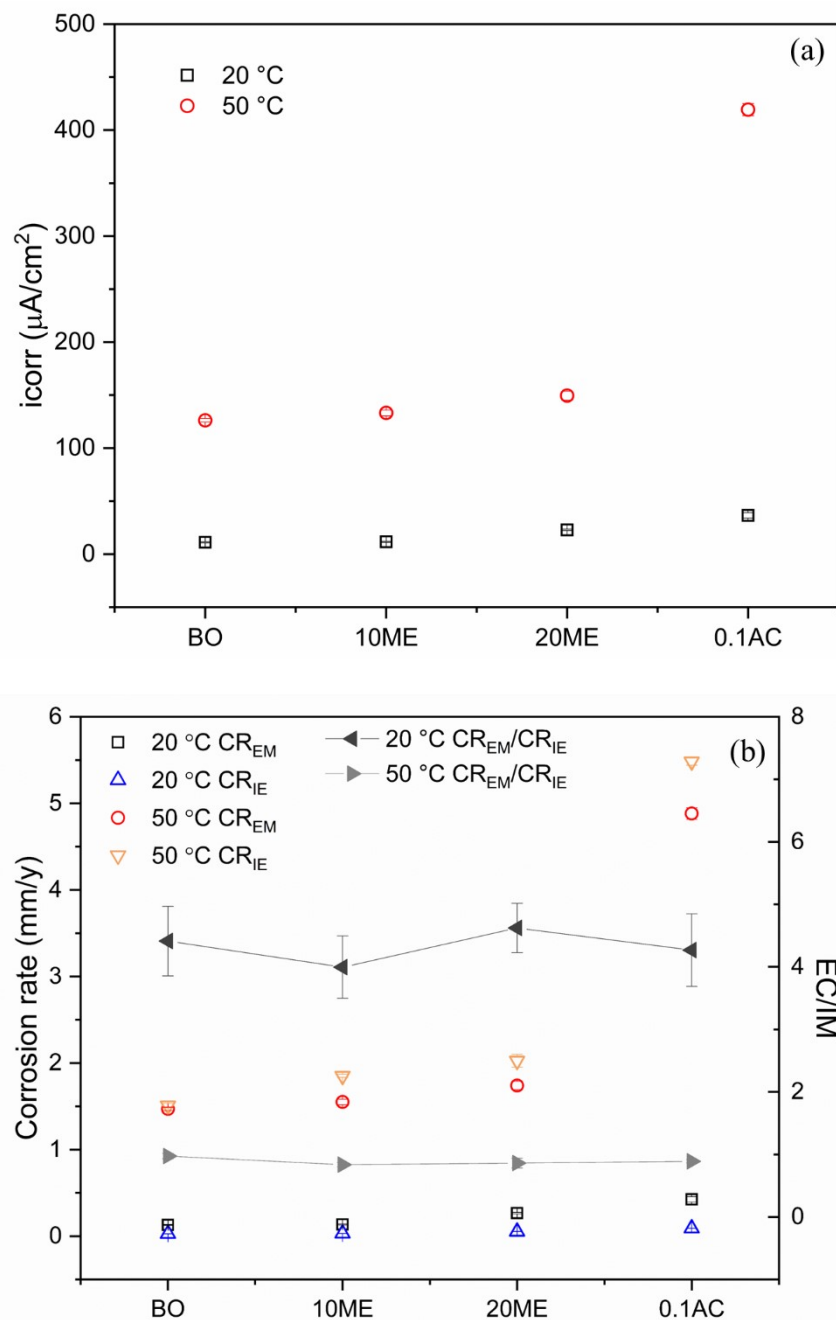
Fig. 4.9. (a) The corrosion current density (i_{corr}) of CS at 20 and 50 °C after 11 h; and (b) CRs calculated from EMs (CR_{EM}) and IEs (CR_{IE}) at 20 and 50 °C after 11 h and their corresponding ratios at each temperature and in each environment.

The CRs obtained from EMs and IEs were calculated by **Equation (4.2) and Equation (4.3)**, respectively, shown below: CR calculated by EMs (CR_{EM}, mm/y); equivalent weight (EW, 27.92 g); density (ρ, 7.86 g/cm^3); CR calculated by IEs (CR_{IE}, mm/y); mass loss (Δm_{loss}, g); immersion time (t, h); surface area (A, cm^2).

$$CR_{EM} = \frac{0.00327 i_{corr} EW}{\rho} \qquad\qquad \textbf{Equation (4.2)}$$

$$CR_{IE} = \frac{87600 \Delta m_{loss}}{\rho t A} \qquad\qquad \textbf{Equation (4.3)}$$

Fig. 4.9b and **Table 4.4** present the CRs obtained from EMs (after 11 h) and IEs (after 168 h) at 20 and 50 °C. In general, both methods showed that the CR increased in the order of BO, 10ME, 20ME, and 0.1AC. For both methods at both temperatures, the CRs in 10ME were slightly higher than those in BO. Yet, the CRs in 20ME and 0.1 AC were around 2 and 4 times higher than those in BO, respectively. For all electrolytes, the CRs obtained by EMs at 50 °C were one order of magnitude higher than those at 20 °C. Similarly, the CRs at 50 °C from IEs were around 50 times higher than those at 20 °C. From the perspective of corrosion risk management, CS is suitable for use in BO environments at 20 °C, where the CR of CS is less than 0.1 mm/y. However, CS is not applicable to BO environments at 50 °C as the CR is excessive (> 1.5 mm/y).

Table 4.4. CRs obtained by EMs (CR_{EM}) and IEs (CR_{IE}) [121].

Electrolytes	CR_{EM} (mm/y)		CR_{IE} (mm/y)	
	20 °C	50 °C	20 °C	50 °C
BO	0.130	1.471	0.027	1.509
10ME	0.136	1.551	0.031	1.852
20ME	0.267	1.741	0.054	2.027
0.1AC	0.426	4.883	0.091	5.484

In addition, the CRs obtained by both methods were compared by dividing CR_{EM} by CR_{IE} to validate the corrosion data from EMs at both temperatures. As indicated in **Fig. 4.9a**, at 20 °C, CR_{EM}/CR_{IE} was around 4.3 for all electrolytes. This can be attributed to the fact that CR_{EM} was obtained at the beginning of the corrosion process (11 h), when the CR was relatively rapid, whereas CR_{IE} represented the average CR of CS over 168 h. Despite the relatively large difference in CR data between these two methods, the consistent ratio between CR_{EM} and CR_{IE} for all cases validates the reliability of EMs. This, in turn, provides guidance for accurately calculating real CRs in future studies using EM under similar conditions. At 50 °C, the ratio between CR_{EM} and CR_{IE} for all cases was around 0.9, suggesting the CRs calculated by EMs closely approximate the actual corrosion data at this temperature. This can be explained by the was more aggressive corrosion at higher temperatures, resulting in a quicker attainment of a steady CR. Thus, the CR data obtained after a short period (11 h) closely approximates the average CR over a longer period (168 h).

4.3.2.4 Metal Surface Characterizations

Fig. 4.10 presents the optical micrographs of CS after IEs at 50 °C, revealing uniform corrosion of the metal surfaces. Visual inspection indicated an increase in surface roughness corresponding to the order of corrosion intensity (*i.e.*, BO < 10ME < 20ME < 0.1AC). The XRD analysis (**Fig. 4.11**) on selected CS coupons did not show any metal oxides as the corrosion products, rather only the peaks associated with the base metal (Fe) were detected. This can be attributed to that the metal oxides were too thin or amorphous organic deposits (such as chelate complexes) formed on metal surfaces.
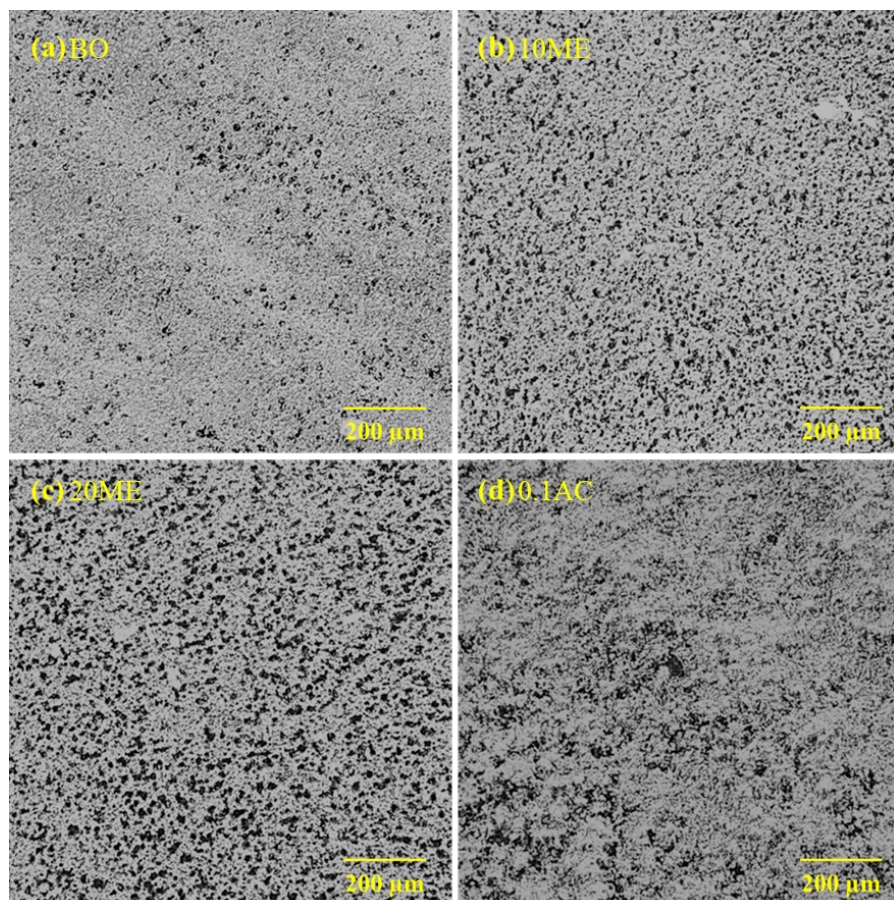
Fig. 4.10. Optical micrographs of CS after EMs at 50 °C: (a) BO; (b) 10ME; (c) 20 ME; and (d) 0.1AC.
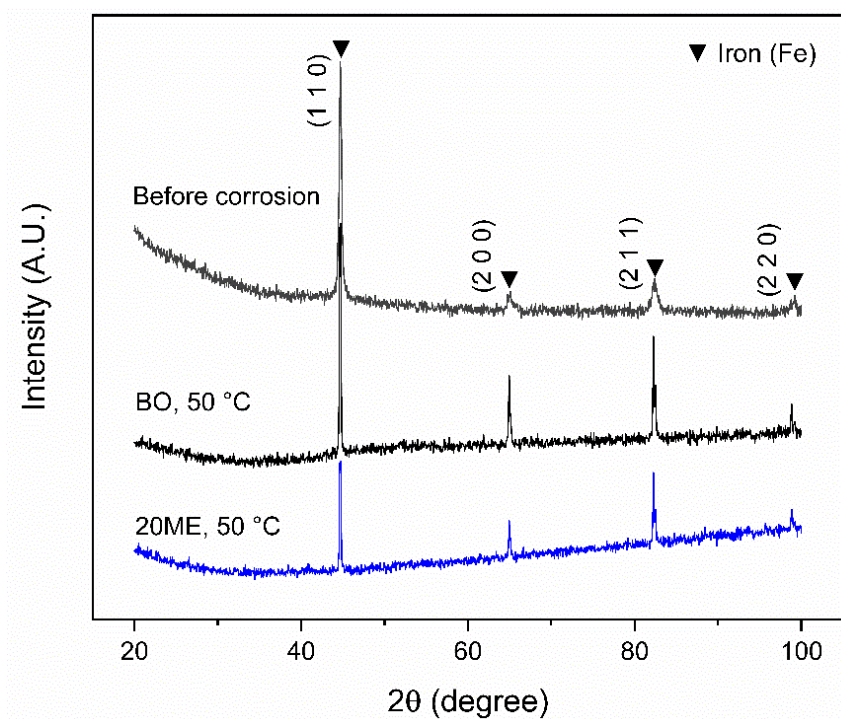
Fig. 4.11. XRD analysis results of uncorroded CS and CS coupons after IEs in BO and 20ME at 50 °C.

To further characterize the surface products after corrosion, XPS analysis was performed on the CS coupon after the IE in BO at 50 °C. The XPS analysis revealed the chemical states of elements present on the metal surface. **Fig. 4.12a** shows the C 1s spectra that exhibited distinct chemical forms of carbon present on the surface and were classified into three peaks: (1) carbon bonded to carbon or hydrogen (C–C or C–H, binding energy (BE)=284.8 eV); (2) carbon-oxygen single bond (C–OH or C–O–C, BE=286 eV); and (3) carbon-oxygen double bond (C=O or O–C=O, BE=288.5 eV) [84]. Meanwhile, **Fig. 4.12b** displays the O 1s spectra with three fitted peaks: (1) oxygen atoms in metal oxides (BE in the range of 529.7 eV); (2) oxygen-carbon double bond or oxygen bonded to two carbon atoms (C=O or C–O–C, BE=531.5 eV); and (3) oxygen in a hydroxyl group bonded with carbon (C–OH, BE=533 eV) [45]. In addition, **Fig. 4.12c** presents the N 1s spectra

including peaks corresponding to metal nitride (BE=397.6 eV) and C–NH$_2$ (BE=399.7 eV). The XPS results indicated the presence of extremely thin layers of metal oxides and metal nitrides formed on the metal surface after corrosion. However, these layers were not detectable by XRD. Furthermore, the XPS analysis suggested the existence of an organic compound layer on the metal surface, which remained even after ultrasonic cleaning in methanol and acetone following IEs. This deposited organic layer is likely composed of chelate complexes formed through the chelation mechanism between iron and organic compounds containing oxygen and nitrogen atoms. The strong bonding between the metal substrate and oxygen/nitrogen atoms prevented the removal of these chelate complexes by organic solvents.
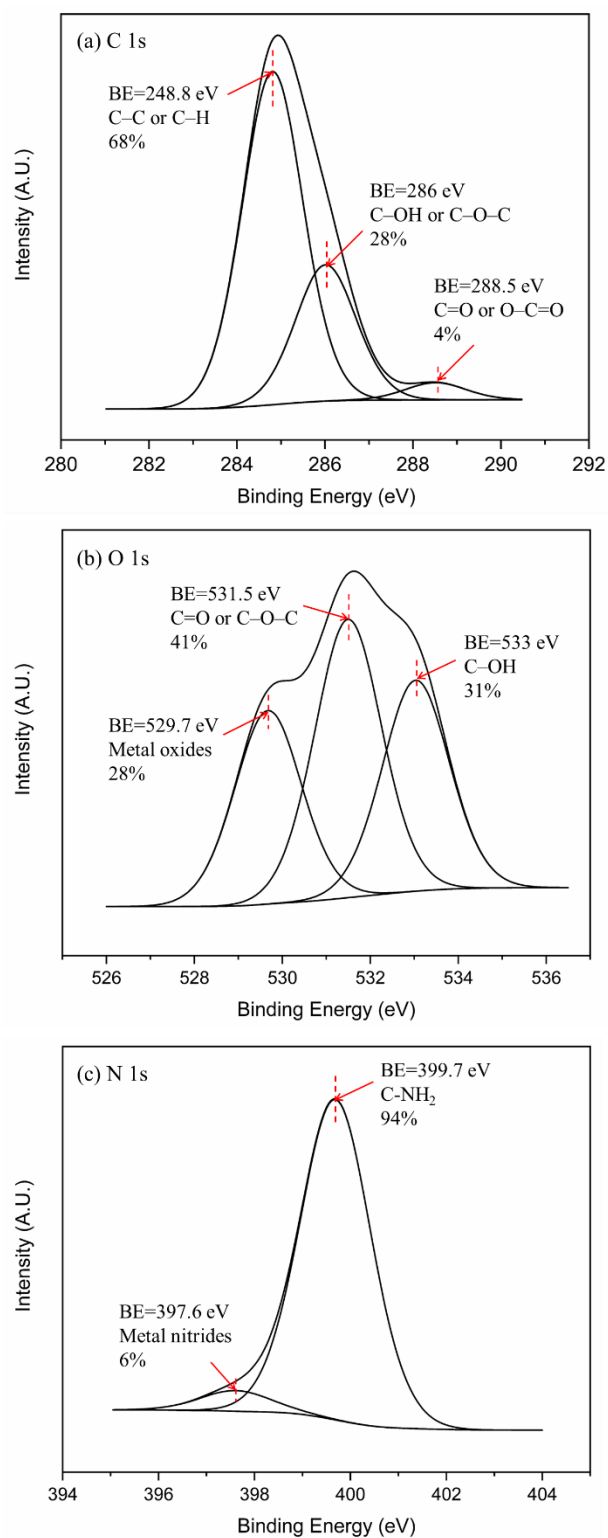
Fig. 4.12. XPS analysis results of the CS coupon after the IE in BO at 50 °C. The spectra, corresponding bonds, and area percentages of: (a) C 1s; (b) O 1s; and (c) N 1s.

4.4. Conclusions

This study utilized various EM techniques, including OCP, PDP, Tafel scans, and EIS, to investigate the corrosion behavior of CS in different environments, such as BO, 10ME, 20ME, and 0.1AC, at both 20 and 50 °C. Simultaneously, IEs were performed under identical conditions to allow for a comprehensive comparison. Several techniques were employed to enhance the quality of electrochemical data in low-conductive environments. Some key conclusions are summarized below:

- PDP plots indicated uniform corrosion of CS in all studied environments. CS exhibited slightly higher corrosion rates (CRs) in 10ME compared to BO, while in 20ME and 0.1AC, the CRs were 2 and 4 times higher than in BO, respectively, at both temperatures.

- EIS Nyquist plots suggested the involvement of adsorption/chelation processes in the corrosion mechanisms, well represented by the inductance component in the ECM used for data fitting. Bode plots demonstrated a good fit of the ECM response to the corrosion processes. Rct (charge transfer resistance) decreased in the order of BO, 10ME, 20ME, and 0.1AC, while icorr (corrosion current density) increased following the same order.

- Temperature significantly influences CS corrosion in the presence of BO. The CRs obtained from IEs at 50 °C were approximately 50 times higher than those recorded at 20 °C. At 20 °C, the ratio of CRs obtained from EMs to those from IEs was approximately 4.3 for all electrolytes, and at 50 °C, this ratio was around 0.9 for all cases.

- Overall, this research demonstrates the suitability of EM techniques for investigating corrosion in BO environments and provides valuable insights into the corrosion behavior of CS under various conditions.

Chapter 5. Corrosion-Induced Changes in Bio-oil Aging: A Gas Chromatography Exploration

Abstract

Understanding the intricate interactions among metals, corrosion products, and bio-oil (BO) is crucial for the safety and efficiency of BO operations. This study conducted aging experiments on BO and immersion experiments with BO + steel, including carbon steel (CS) and stainless steel (SS), at 80 °C for 168 h. Synthetic corrosion products, such as Fe_2O_3 and Cr_2O_3 powders, were also added separately to BO alongside immersion experiments. Gas generated during these experiments was collected and analyzed via gas chromatography (GC). Results revealed that 80 °C serves as a suitable pre-heating temperature for BO without gas evolution. Additional BO aging experiments at up to 220 °C for 24 h indicated an increase in CO_2 and CO concentrations with temperature. Immersion experiments demonstrated higher H_2 and CO_2 production during CS immersion at 80 °C compared to 50 °C, attributed to a higher corrosion rate at the higher temperature. In the BO + Fe_2O_3 trial, less H_2 was released but more CO_2 was produced compared to BO + CS immersion, due to BO internal reactions catalyzed by Fe_2O_3. Additionally, BO + SS 304L and BO + Cr_2O_3 trials exhibited similar H_2 and CO_2 production, indicating a dominant catalytic effect of Cr_2O_3 on BO. Characterization results revealed that leached Fe ions chelated with organic compounds in the BO, forming viscous chelate complexes that promoted phase separation. These findings have significant implications for BO co-processing operations, highlighting the need to optimize preheating temperatures, validate the compatibility of materials, and implement safety measures to mitigate gas accumulation risks.

Keywords: Bio-oil; Aging; Corrosion; Gas Chromatography (GC); Chelation; Co-processing

5.1. Introduction

Biofuels play a significant role in achieving the ambitious goal of net-zero emissions and addressing the escalating demand for sustainable energy sources [138, 139]. To minimize the impact on food and land use, the focus has shifted towards harnessing biofuels derived from non-food energy crops, agricultural waste residues, and various other wastes [140]. An effective strategy involves converting lignocellulosic biomass–derived bio-oil (BO) into drop-in biofuels through co-processing with petroleum intermediates in fluid catalytic cracking (FCC) units [118, 141]. This approach offers a promising avenue for BO upgrading with minimal capital investment requirements and has been extensively investigated, particularly within the last decade [17, 142, 143].

While ensuring the quality equivalence of products derived from co-processing to those produced without adding BO is vital, operational safety, compatibility of materials of construction (MOCs), and BO stability must also be addressed before integrating into the system [91, 119, 141]. For instance, addressing challenges such as the thermal stability of BO during the preheating and the potential corrosivity of BO to MOCs becomes imperative considerations [100, 144].

One primary challenge arising from BO aging is the increase in viscosity due to polymerization reactions involving organic compounds containing hydroxyl, carbonyl, and carboxyl groups [25]. This viscosity escalation hinders the flowability of BO, posing obstacles in its integration into FCC systems and potentially impacting the conversion ratio to biofuels [26, 27]. Research efforts have focused on understanding the aging rate, particularly the viscosity increase at different temperatures, with 50 °C as the maximum storage temperature and 80 °C as the critical pre-heating

temperature for FCC injections [145]. These temperature benchmarks are set to ensure that the viscosity of BO does not undergo dramatic alterations in chemical properties, maintaining its compatibility with FCC processes [146, 147].

Researchers have also delved into investigating the compatibility of BO with common MOCs, such as carbon steel (CS) and stainless steel (SS) [32, 44, 148]. CS exhibits pronounced corrosion in BO above 50 °C, exceeding 1 mm/y, while SS remains corrosion-resistant at this temperature threshold [47, 48]. When subjected to an 80 °C BO environment, SS 304L experiences a moderate corrosion rate, surpassing 0.1 mm/y, while SS 316L demonstrates minimal corrosion [45, 149].

Beyond the corrosion of steels induced by BO, it is equally vital to evaluate the impact of steel corrosion on BO quality during processing, informing decisions in BO storage systems and operational protocols for enhanced safety and efficiency. The previous study indicates that the aging of BO was not affected by the existence of metals such as SS306 and copper that are not corroded in BO at 80 °C [150]. However, the corrosion of CS, particularly, has a significant impact on the aging rate of BO. This influence is evident in 168 h of immersion experiments with CS, showcasing a substantial viscosity increase of approximately 2.5 times at 50 °C and 30 times at 80 °C, compared to conditions where CS is absent [151]. A proposed chelation mechanism involving the interaction of Fe with heteroatoms (such as nitrogen and oxygen) in BO contributes to this viscosity increase [112, 152].

Despite limited focus, assessing gases generated during BO aging and steel corrosion is essential for elucidating the interactions among metals, corrosion products, and BO. In this investigation,

aging experiments on BO and immersion experiments with BO + steel were conducted in an autoclave at 80 °C for a duration of 168 h. Common MOCs, including CS and SS 304L, were used for immersion studies. Additionally, synthetic corrosion products (Fe_2O_3 and Cr_2O_3) were introduced into the BO to compare with the immersion experiments. The evolved gases were collected using aluminum foil bags at room temperature and analyzed by gas chromatography (GC). Comprehensive characterization techniques were employed to provide an understanding of the interactions between the metals, corrosion products, and BO, offering valuable insights into the intricate dynamics of the BO aging and metal corrosion processes.

5.2. Experimental Setup

5.2.1. Aging and Corrosion Immersion Experiments

The BO used for this study was a pinewood-derived pyrolysis oil. Its physical and chemical properties can be found elsewhere [151]. As shown in **Fig. 5.1a**, an autoclave was used for the BO aging and immersion experiments. A digital pressure gauge was connected to the autoclave to monitor the pressure. For each trial, 100 mL of BO contained in a PTFE container was placed inside the autoclave. CS and SS 304L strip coupons ($1 \times 1/4 \times 1/16$ in^3) were used for immersion experiments. Details regarding the chemical compositions of used materials and immersion experiment procedures are available elsewhere [151]. As indicated in **Fig. 5.1b**, the autoclave was heated by a heating mantle, and the temperature was monitored by a thermocouple. For comparison, 2 g of Fe_2O_3 and Cr_2O_3 powders were added into BO. Initially, aging and immersion experiments were carried out at 80 °C for 168 h. Upon the experimental results, additional aging experiments were conducted at 100, 150, and 220 °C for 24 h. Besides, in order to study the temperature effect on corrosion, a CS immersion experiment was also conducted at 50 °C for 168

h. After each experiment, the autoclave was cooled overnight to reach room temperature. The remaining gases were collected by aluminum foil bags via the outlet of the autoclave (**Fig. 5.1b**). **Table 5.1** summarizes the setup for each trial of the experiment.
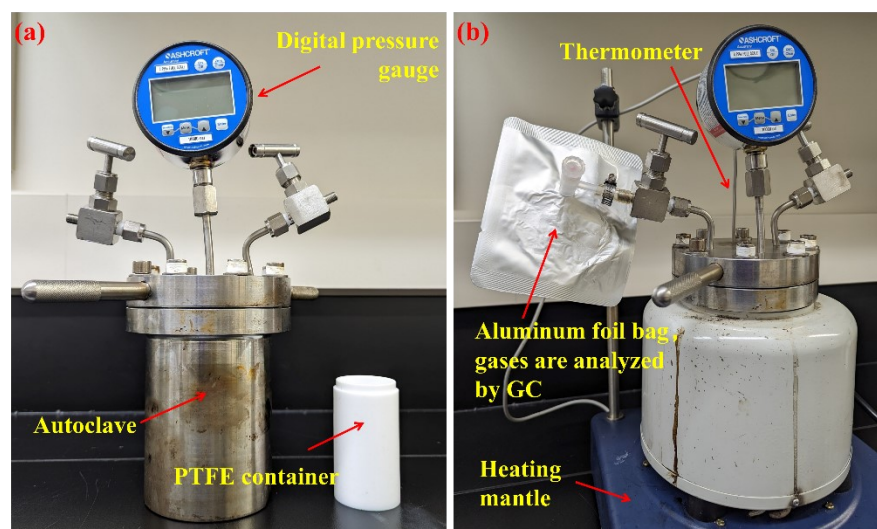
Fig. 5.1. The experimental setup of bio-oil aging and immersion experiments using an autoclave. After the autoclave cooled to room temperature, gases were collected in aluminum foil bags and then analyzed by the GC equipment.

Table 5.1. Experimental setup for BO aging and immersion experiments.

Trial No.	BO (mL)	Metal	Additive	Temperature (°C)	Time (h)
1	100			80	168
2	100	CS		80	168
3	100	SS 304L		80	168
4	100		Fe_2O_3	80	168
5	100		Cr_2O_3	80	168
6	100			100	24
7	100			150	24
8	100			220	24
9	100	CS		50	168

5.2.2. Gas Chromatography (GC) Analysis

Gas chromatography (GC) was used to characterize the evolved gases during BO aging and immersion experiments. The GC equipment was the Agilent 8890 series GC system with an Agilent J&W capillary GC column (27 m length×320 μm inner diameter×8 μm thickness). In each measurement, a 5 mL gas sample was injected. Two thermal conductivity detectors (TCDs) in GC were used to detect non-hydrocarbon gases. One of the TCDs was used for detecting H_2 using N_2 as the carrier gas. The other TCD was used to detect nonhydrocarbon gases such as CO and CO_2 using H_2 as the carrier gas. The flame ionized detector (FID) was used to detect hydrocarbon gases, where N_2 was used as the carrier gas. The GC oven temperature was programmed to increase from 60 °C (held for 1min) to 190 °C (held for 10min) at a rate of 20 °C/min. The FID and TCD were set at 250 °C.

5.2.3. Bio-oil (BO) and Metal Characterizations

After the aging and immersion experiments, viscosity measurements and thermogravimetric analysis (TGA) were performed on the BO samples. Besides, the BO samples collected after immersion experiments was dissolved into methanol and then filtered by filter paper. The solid powders that remained on the filter paper were rinsed with methanol three times and then dried. The collected solid powders and steel coupons were analyzed by scanning electron microscopy (SEM) with energy-dispersive X-ray spectroscopy (EDS) and X-ray diffraction (XRD) to characterize the corrosion product. In addition, X-ray photoelectron spectroscopy (XPS) was conducted for the solid powers to examine the bonding between the components of corrosion products and BO. The equipment information and detailed setup can be found elsewhere [151, 152].

5.3. Results and Discussion

5.3.1. Bio-oil (BO) Aging and Corrosion Immersion Experiments at 80°C

The BO aging and immersion experiments were carried out at 80 °C for 168 h (refer to trials 1–5 in **Table 5.1**). The pressure within the autoclave was continuously monitored, with the results summarized in **Fig. 5.2a**. At the onset of each trial, when the temperature reached 80 °C (designated as time "0"), the initial pressure registered at 7 psi, attributed to steam and low-boiling hydrocarbon compounds. As depicted in **Fig. 5.2a**, throughout the duration of the aging experiment, denoted as "BO", there was no observable change in pressure. This implies that no gas evolution occurred during the aging process at this temperature. Hence, it can be concluded that 80 °C serves as a safe pre-heating temperature for BO, as it avoids the breakdown of hydrocarbon chains and prevents internal reactions that may lead to the release of gases.
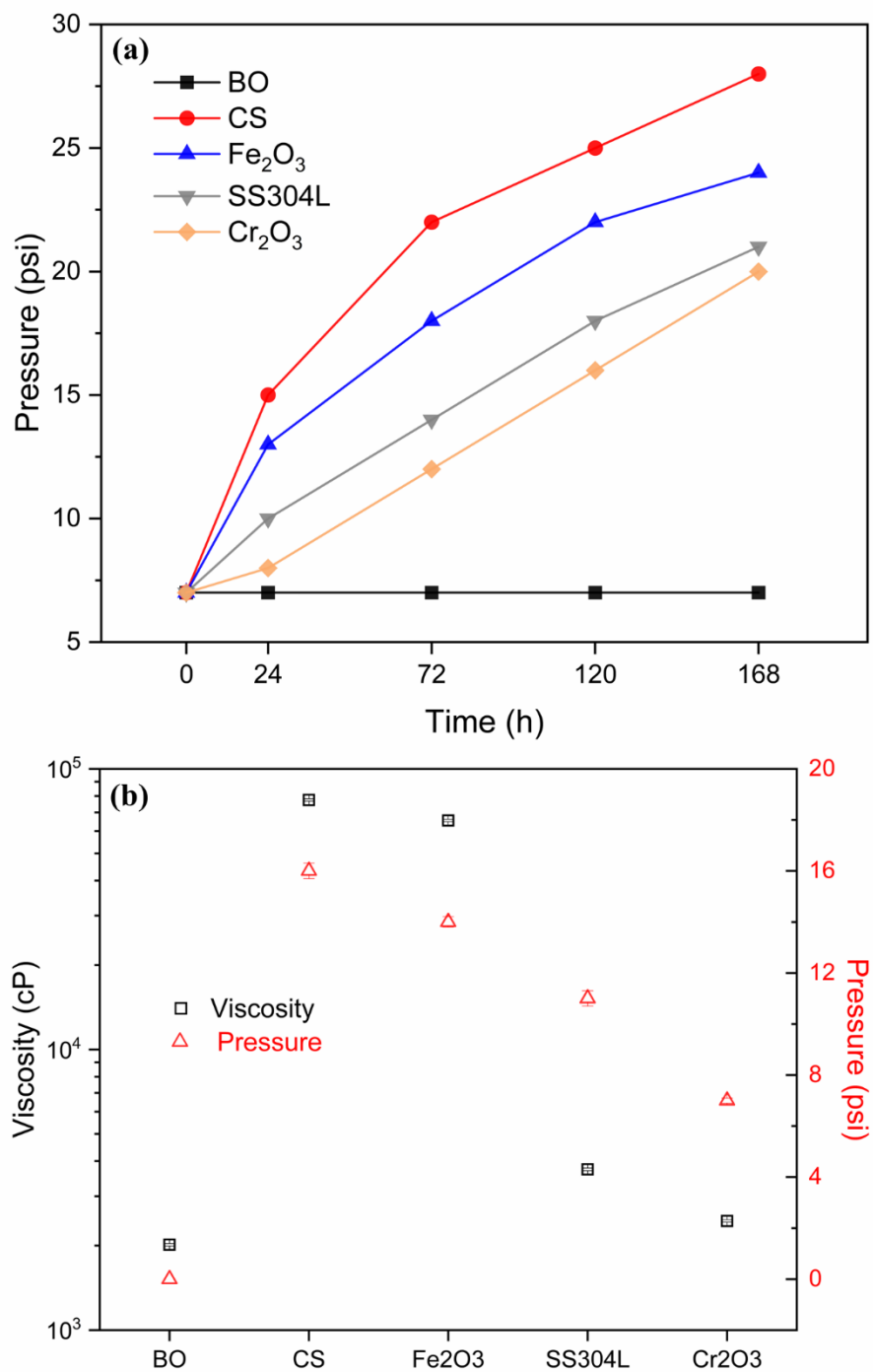
Fig. 5.2. (a) The pressure changes inside the autoclave during bio-oil aging and immersion experiments for 168h at 80°C; and (b) the pressure at room temperature and the viscosity of the bottom phase of bio-oil for each trial of the experiment.

For the immersion experiment with CS, the pressure kept increasing and reached 28 psi at 168 h (red line in **Fig. 5.2a**). The corrosion of CS generated H_2, contributing to the pressure increase. The increasing rate of pressure declined which could be caused by the slowing down of CS corrosion over time. The total mass loss for CS coupons (primarily Fe) was 1.4 g corresponding to 2 g of Fe_2O_3 (with the same molarity of Fe), which was the reason why 2 g of Fe_2O_3 additives were added for comparison (**Table 5.1**). The pressure trend for the Fe_2O_3 trial was similar to that of CS immersion with a lower final pressure of 24 psi at 168 h. Fe_2O_3 would dissolve into BO (pH=2.8) by reacting with organic acid at the experimental conditions [153, 154]. By visual observation, there was no red Fe_2O_3 residue after the experiment. However, the dissolution of Fe_2O_3 does not inherently produce any gas. The observed increase in pressure could potentially be attributed to gases produced from internal reactions of the BO with Fe_2O_3 acting as a catalyst, or from interactions between Fe ions and organic compounds. This aspect will be further explained based on the characterization results presented below.

The pressure of SS 304L and Cr_2O_3 trials increased at a relatively steady rate reaching the final pressures of 21 and 20 psi respectively (**Fig. 5.2a**). Notably, the corrosion rate of SS 304L at 80 °C was approximately one order of magnitude lower than that of CS, with a total weight loss recorded at 0.2 g [151]. However, despite this disparity, the final pressure recorded in the SS 304L trial was comparable to that of the CS trial (21 vs. 28 psi), suggesting that gases produced by corrosion accounted for only a small fraction of the total evolved gases during immersion experiments. The observed increase in pressure during immersion can be attributed to interactions between metals and corrosion products with the BO. Following the Cr_2O_3 trial, a greenish layer was observed on the BO surface, indicating that Cr_2O_3 did not dissolve in the BO. Despite this, the

final pressure in the Cr_2O_3 trial closely matched that of SS 304L, implying that Cr_2O_3 could potentially act as a catalyst, facilitating internal reactions of the BO to produce light hydrocarbons.

Fig. 5.2b presents the pressure inside the autoclave for each trail after cooling down to room temperature and the viscosity of the BO bottom phase after aging and immersion experiments. The pressure for the BO aging experiment was 0, so no gas was collected. This agreed with the findings shown in **Fig. 5.2a** that no gas was produced during the aging of BO at 80 °C. The pressure at room temperature from high to low (**Fig. 5.2b**) followed the order of "CS", "Fe_2O_3", "SS 304L", and "Cr_2O_3" aligning with the order of the final pressure at 168 h (**Fig. 5.2a**). Compared to SS 304L (11 psi), more excessive corrosion of CS (16 psi) produced more non-condensable gases (*i.e.*, H_2) leading to a higher pressure at room temperature. Compared to Cr_2O_3 (7 psi), adding Fe_2O_3 resulted in a higher pressure (13 psi) suggesting that the effect of Fe ions on BO resulting from Fe_2O_3 dissolution was more prominent than that of Cr_2O_3.

Following the aging and immersion experiments, the BO underwent phase separation, yielding a watery top phase and a viscous bottom phase [155, 156]. As shown in **Fig. 5.2b**, the viscosity of the BO bottom phase was proportional to the pressure. The viscosity of the BO bottom phase from the BO aging experiment (2015 cP) was one order of magnitude higher than that of unaged BO (171.5 cP) due to the polymerization reactions during aging [151]. The viscosities of "CS" and "Fe_2O_3" skyrocketed to 77500 and 65500 cP, respectively, more than 30 times more viscous than that measured from the "BO" trial. Previous studies have reported that CS corrosion in BO would increase BO viscosity [112, 151]. The bonding between Fe ions with heteroatoms (such as nitrogen and oxygen) in BO led to the formation of chelate complexes [152]. Similar mechanisms have also

been identified in plants uptalking Fe ions from soil. Fe metabolism is essential for the growth of plants. In order to absorb Fe from the soil, organic compounds (e.g., nicotianamine, containing carboxylic acid and amine functional groups) in the roots chelate Fe ions and then the chelated Fe are transported by ferroportin [157, 158]. Similarly, in this study, Fe ions released from CS corrosion and Fe_2O_3 dissolution likely chelated with organic compounds in the BO, forming chelate complexes and inducing a viscosity increase. The viscosity of "SS 304L" (3740 cP) was 1.5 times higher than that of "Cr_2O_3" (2450 cP), which was caused by the corrosion of SS 304L releasing Fe ions into BO. the viscosity of "Cr_2O_3" was comparable to that of "BO" (2450 vs. 2015 cP), indicating the absence of chelation effects in the "Cr_2O_3" trial.

TGA measurements were conducted in an argon atmosphere to reveal the relationship between BO mass loss and temperature from 30 to 750 °C for unaged BO and BO bottom phases obtained from aging and immersion experiments (refer to trials 1–5 in **Table 5.1**). As indicated in **Fig. 5.3**, the percentage of remaining BO weight (denoted as TG) was plotted versus temperature. Overall, the TG curves exhibited a smooth decreasing trend, with a relatively higher decline rate observed between 30 to 400 °C. For instance, there was around 20wt% remaining for the unaged BO at 400 °C, and it decreased to 14wt% at 750 °C. The TG curves shifted to the upper right as indicated by the red arrow following the sequence of "unaged BO", "BO", "Cr_2O_3", "SS 304L", "Fe_2O_3", and "CS" aligning with the increase in viscosity. This shift to the upper right represents less mass loss at lower temperatures. For example, there was 40 wt% remaining for "CS" at 400 °C, two times higher than that of "unaged BO". Furthermore, the TG curves can be categorized into three distinct groups based on the remaining BO at 750 °C: "unaged BO", "BO, Cr_2O_3, and SS 304L" and "Fe_2O_3, and CS" corresponding to the BO viscosity across three orders of magnitude (10^2–10^4 cP).
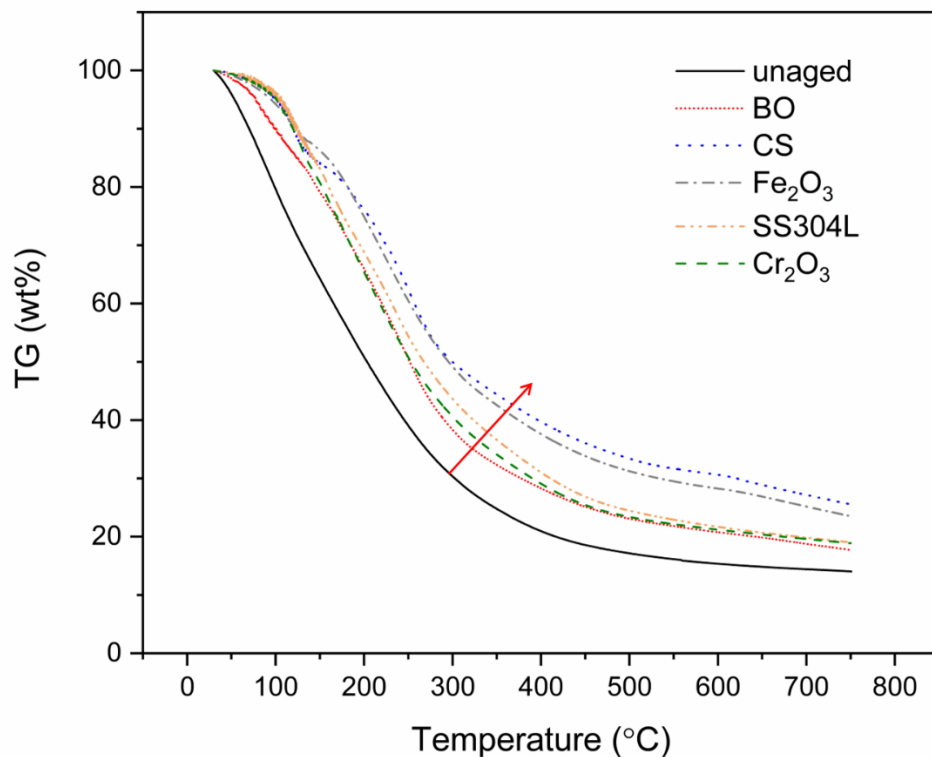
Fig. 5.3. TG curves of unaged bio-oil and the bottom phase of bio-oil samples after bio-oil aging and immersion experiments for 168h at 80°C (refer to trials 1–5 in **Table 5.1**).

5.3.2. Gas Chromatography (GC) Analysis

After the aging and immersion experiments, the autoclave was cooled down to room temperature, and gases were collected in aluminum foil bags (**Fig. 5.1b**). Notably, for the BO aging conducted at 80 °C, no gas was collected. Consequently, BO aging experiments at higher temperatures, namely 100, 150, and 220 °C, were carried out. It is worth mentioning that due to the significant polymerization of BO at higher temperatures, and considering practical considerations for co-processing operations, the aging time was set at 24 h [145]. Furthermore, to account for the temperature effect on CS corrosion and the interactions between CS corrosion products and BO, an additional immersion experiment was conducted for CS at 50 °C. These aging and immersion experiments, in addition to the trials 1–5, were summarized in **Table 5.1** trials 6–9.

91

Fig. 5.4 presents the GC analysis results for experiments listed in **Table 5.1**. Gases such as H_2, CO_2, CO, O_2, and N_2 were quantified by GC. The detected O_2 and N_2 should come from the air in the autoclave. The mixture of light hydrocarbon gases (e.g., methane, propylene, 1-butene, i-butylene, etc.) was classified as "other". The total concentration of the above-mentioned six items was 100 vol.% for each trial of the experiment. For the aging experiments shown in **Fig. 5.4a**, the volume percentage of H_2 decreased with temperature (45 vol.% at 100 °C vs. 5 vol.% at 220 °C). The concentration of "other" declined from 4 vol.% at 100 °C to 0 at 220 °C. This suggested that BO polymerized more severely at higher temperatures, so fewer light gases (*i.e.*, H_2 and low-boiling hydrocarbon gases) were evolved. Besides, H_2 would go back to BO by reacting with heavy compounds, which is similar to the hydrodeoxygenation processes. In contrast, the CO_2 and CO concentrations increased with temperature. From 100 °C to 220 °C, the CO_2 concentration increased from 30 vol.% to 85 vol.%, and CO increased from 0.3 vol.% to 3 vol.%. At high temperatures, more CO_2 and CO were produced as the byproducts of complex internal chemical reactions during BO aging. For instance, oxygen can be removed from BO via decarboxylation (oxygen removed as CO_2) and decarbonylation reactions (oxygen removed as CO) [159-161]. CO_2 and CO were also observed in the products of co-processing [91, 162, 163]. The loss of carbon to these gases reduces the yield of renewable fuel products [164].
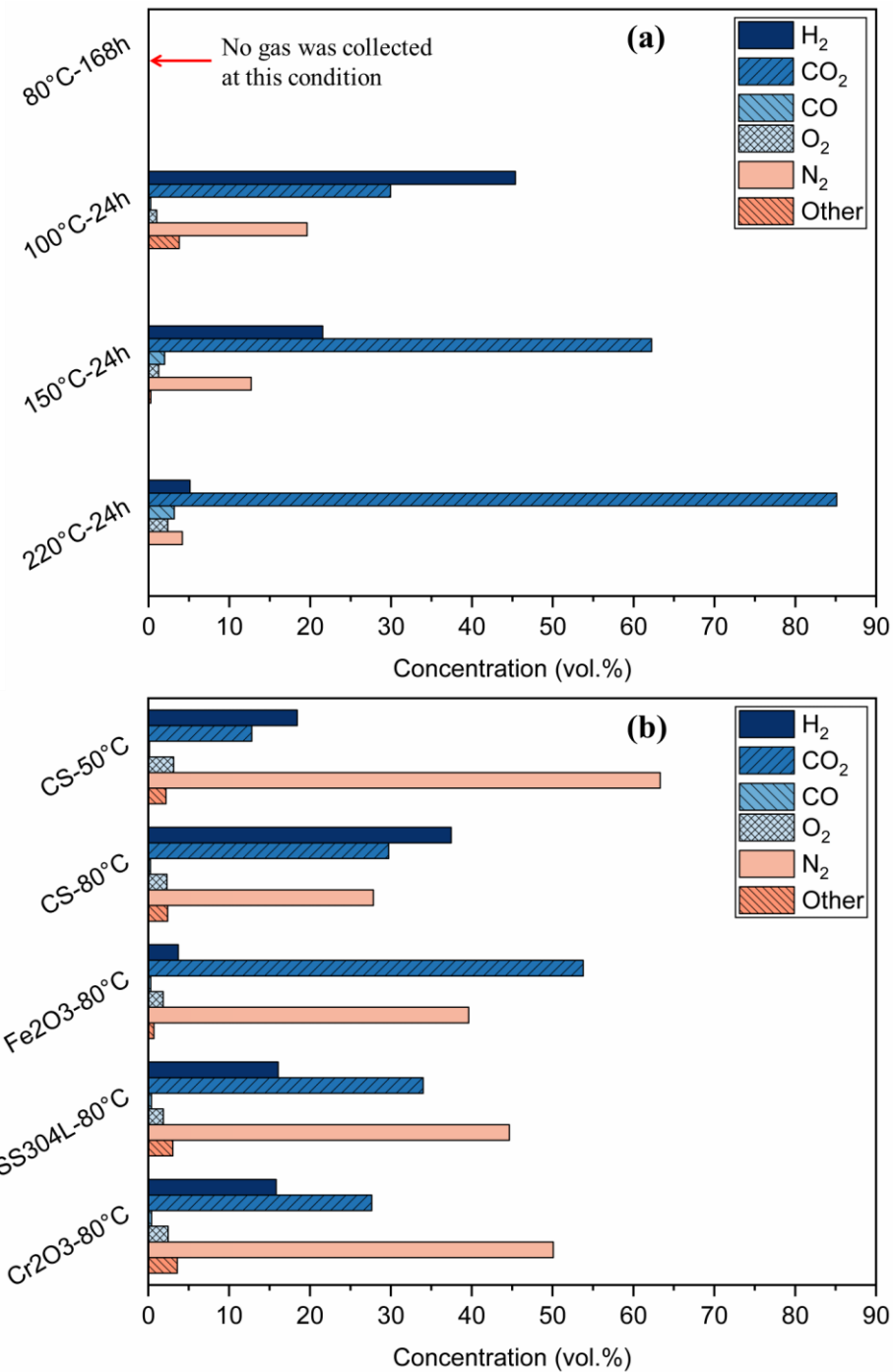
Fig. 5.4. The GC analysis on gas samples collected from bio-oil aging and immersion experiments: (a) bio-oil aging at 100, 150, and 220°C for 24h; and (b) CS, Fe_2O_3, SS 304L, Cr_2O_3 immersed in bio-oil for 168h. All gases were collected after the autoclave cooled down to room temperature. No gas was collected for bio-oil aging at 80°C for 168h.

The above findings provide two crucial information for BO co-processing operations. Firstly, the maximum preheating temperature for BO before injecting into the riser of FCC (150–300 °C for VGO injection) must be carefully considered. A low preheating temperature for BO may lead to insufficient contact between BO and catalysts causing a low BO conversion ratio [66, 165]. A high preheating temperature would promote BO polymerization causing the blockage of injection nozzles [119]. A careful design is needed considering factors such as temperature, injection time, BO aging rate, and BO conversion ratio to optimize the co-processing processes. Secondly, the production of gases during BO aging necessitates the implementation of additional safety features for preheating facilities. These safety measures are essential to mitigate potential risks associated with gas accumulation and release, ensuring the safe operation of the co-processing system.

Fig. 5.4b presents the GC results for immersion experiments showing that more H_2 and CO_2 were produced at 80 °C for CS immersion (37 and 30 vol.%, respectively) compared to 50 °C (18 and 13 vol.%, respectively). As the corrosion rate of CS at 80 °C was 5 times higher than that at 50 °C, more H_2 was released and more corrosion products interacted with BO [151]. The Fe_2O_3 trial produced less H_2 (4 vol.%) but more CO_2 was produced (54 vol.%) compared to CS immersion, suggesting catalytic effects on BO. Studies have shown that metal oxides such as Fe_2O_3 and Cr_2O_3 can act as catalysts for ketonization reactions of carboxylic acids where carboxylic acids react with each other producing ketones with CO_2 as the byproduct [166, 167]. This would explain why the Fe_2O_3 trial generated more CO_2 although Fe_2O_3 would gradually be consumed by organic acids in BO. It is necessary to mention that BO consists of over 400 organic compounds, so other internal reactions would also be responsible for the generation of gases detected by GC. The H_2 and CO_2 production (around 16 and 30 vol.%, respectively) of SS 304L and Cr_2O_3 trials were comparable

to each other, indicating the catalytic effect of Cr_2O_3 on BO dominated the gas production for these two experiments. For all trials, less than 0.5 vol.% of CO and 4 vol.% of other light hydrocarbon gases were produced. These findings underscore the need for careful consideration of material selection and operating conditions to ensure the safety and feasibility of BO co-processing operations.

5.3.3. Bio-oil (BO) and Metal Characterizations

XRD analysis was performed on steel coupons post-immersion at 80 °C to investigate potential corrosion products deposited on the metal surfaces. As depicted in **Fig. 5.5a** and **5.5b**, the observed peaks corresponded to the substrate metals CS and SS 304L, respectively. Notably, no distinct corrosion product was identified by XRD, likely attributed to the dissolution of corrosion products, such as Fe_2O_3, by BO. Previous SEM/EDS findings suggested the formation of amorphous organic deposits on metal surfaces in the form of chelate complexes [151, 152]. This phenomenon indicates that the corrosion rate may be accelerated due to the consumption of corrosion products. To further elucidate the mechanism of chelation between Fe ions and organic compounds and to trace the lost Fe in BO, the BO utilized in the CS immersion experiment at 80 °C was dissolved in methanol and subsequently filtered. The resulting methanol-insoluble fraction was collected in the form of black powders for subsequent characterization.
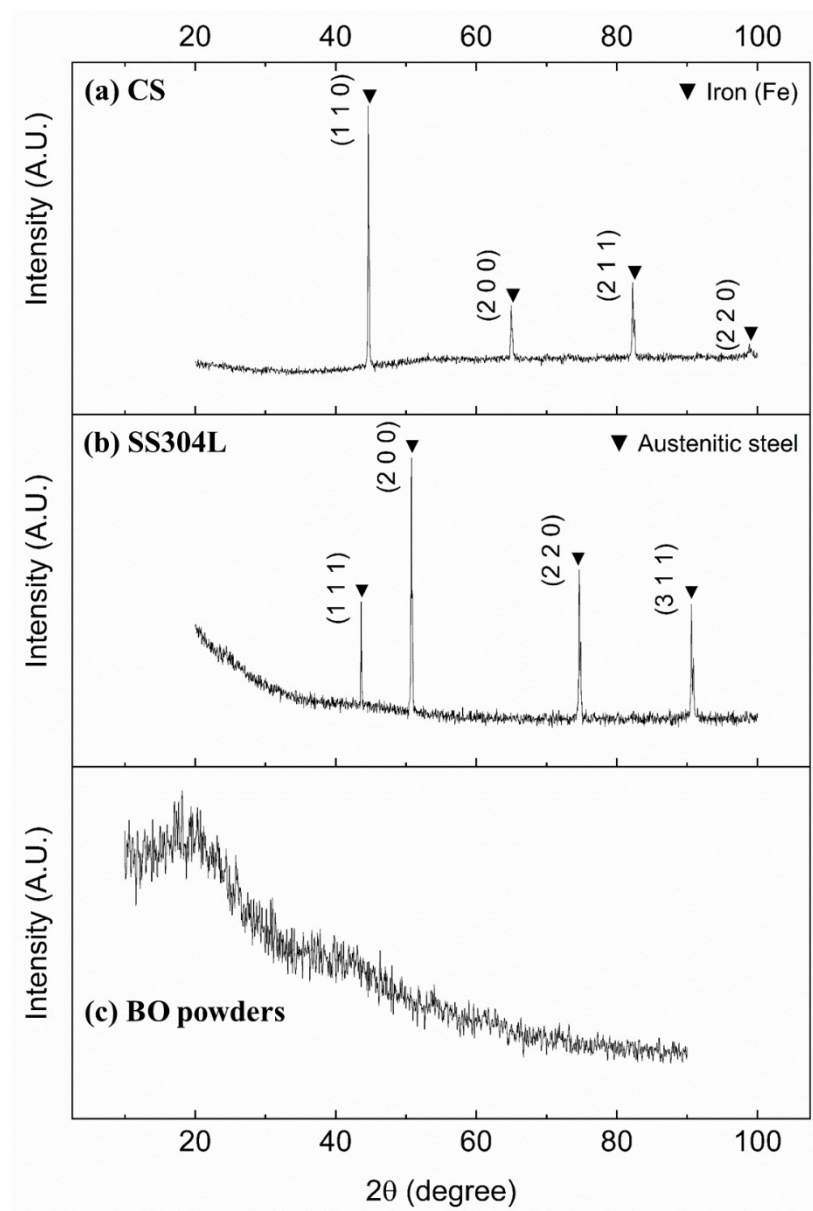
Fig. 5.5. XRD analysis results of: (a) CS surface and (b) SS 304L surface after immersion experiments at 80°C for 168h. (c) The XRD characterization of the methanol-insoluble fraction (powders) of the bio-oil sample from the CS immersion experiment at 80°C for 168h.

As shown in **Fig. 5.5c**, XRD analysis revealed the absence of any peaks for BO powders, indicating their amorphous nature. This finding demonstrates the absence of Fe oxides, typically observed as corrosion products, within the BO. Further characterization of the BO powders was conducted

96

using SEM/EDS, as illustrated in **Fig. 5.6**. Irregularly shaped BO particles with a broad size distribution were observed in **Fig. 5.6a**. EDS mapping confirmed the predominant presence of carbon, oxygen, and Fe within the BO powders, with Fe constituting 1.5 atomic% of the overall examined area (**Fig. 5.6b**). Specifically, at "area 1", where larger particles were observed, Fe accounted for 0.5 atomic%, suggesting that these particles primarily consist of BO polymers. In contrast, "area 2" exhibited significantly smaller particle sizes and a higher Fe content of 20 atomic%. Notably, nitrogen was not detected in the BO powders by EDS analysis, which may be attributed to the low concentration of nitrogen in BO (0.24 wt%) or the presence of nitrogen-containing compounds dissolved in methanol [151]. Combining the XRD and EDS results, the identification of Fe within the BO powders provides compelling evidence for the formation of chelate complexes between Fe and compounds present in the BO.
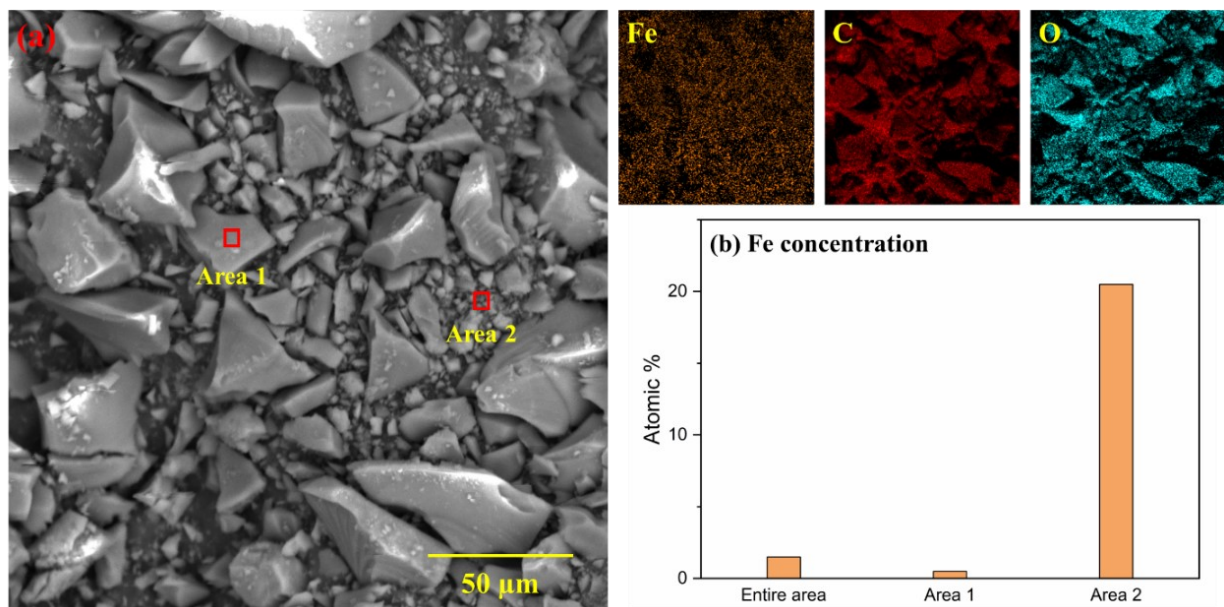
Fig. 5.6. (a) SEM images and compositional mapping by EDS of the methanol-insoluble fraction (powders) of the bio-oil sample from the CS immersion experiment at 80°C for 168h; and (b) the concentration of Fe indicated in the SEM image.

XPS analysis was conducted on the BO powders discussed previously to elucidate the chemical states of elements. As illustrated in **Fig. 5.7a**, the binding energies of Fe^{2+} $2p_{3/2}$ and Fe^{3+} $2p_{3/2}$ were observed at 711.0 and 715.0 eV, respectively, consistent with values reported in the literature [168]. Furthermore, two satellite peaks were discerned at 719.4 and 730.5 eV. Additionally, two Fe $2p_{1/2}$ peaks were identified at 723.2 and 725.8 eV, representing transition peaks associated with the main peaks of Fe $2p_{3/2}$ [169]. The XPS findings for C 1s, O 1s, and N 1s of the BO powders closely resembled those of the organic deposit layer observed on the post-corrosion CS surface in previous studies [152]. It is crucial to underscore the presence of Fe-O and Fe-N bonds as direct evidence of chelation between Fe ions and organic compounds within the BO.
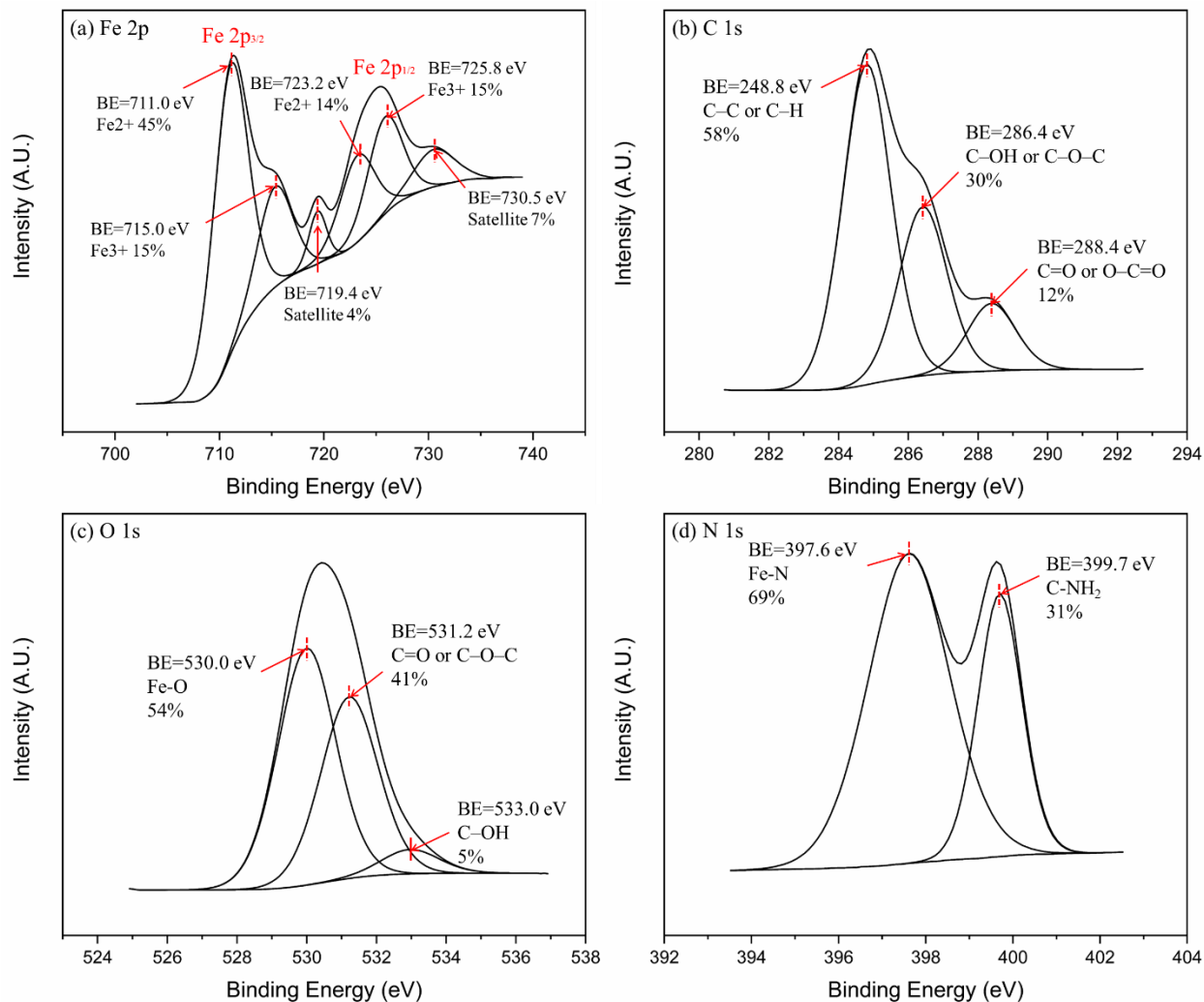
Fig. 5.7. XPS analysis results of the methanol-insoluble fraction (powders) of the bio-oil sample from the CS immersion experiment at 80°C for 168h. The spectra, corresponding bonds, and area percentages of: (a)Fe 2p; (b) C 1s; (c) O 1s; and (d) N 1s.

5.3.4. Mechanisms of Bio-oil (BO) Metal Interactions

According to the above findings, we propose mechanisms that govern the interactions between steel (using CS as a representative example) and BO, depicted in **Fig. 5.8**. When CS comes into contact with BO, steel undergoes electron loss, leading to the formation of oxidized Fe^{2+} ions (Fe $\rightarrow Fe^{2+} + 2e^-$). Meanwhile, dissociated hydrogen ions accept electrons, being reduced to form H_2

($H^+ + 2e^- \rightarrow H_2$). A portion of the detected H_2 in the GC analysis (**Fig. 5.4b**) originates from this process. As free Fe^{2+} ions migrate into the BO, some undergo further oxidation to Fe^{3+} ($Fe^{2+} \rightarrow Fe^{3+} + e^-$). These Fe ions subsequently form chelates with organic compounds in the BO, particularly bonding particularly with heteroatoms like nitrogen and oxygen. This bonding gives rise to chelate complexes characterized by high viscosities, accelerating the aging rate of the BO, denoted by the rate of viscosity increase. Additionally, both Fe ions and ephemeral Fe_2O_3 exert catalytic effects on the BO, enhancing polymerization reactions and resulting in the release of gases as byproducts. The formation of viscous chelate complexes and BO polymerization subsequently contribute to phase separation within the BO.
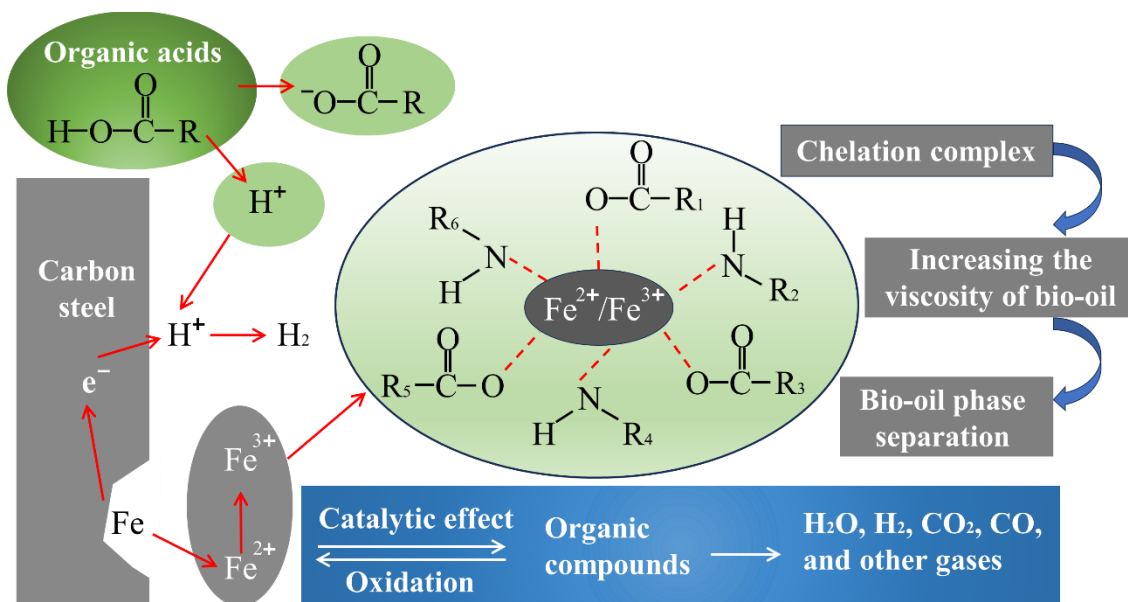
Fig. 5.8. Mechanisms of the interactions between bio-oil and carbon steel.

In summary, beyond the evaluation of MOC integrity, addressing gas production resulting from metal-BO interactions is also crucial for ensuring safe co-processing operations and achieving satisfactory BO conversion. The corrosion of BO to FCC infrastructures poses challenges to the

integrity of facilities such as BO storage units, pipelines, and preheating equipment. Most of the MOCs for FCC units are CS, which experiences excessive corrosion (> 1 mm/y) at temperatures greater than 50 °C [58, 151]. Furthermore, the corrosion products generated from MOCs can interact with BO through processes such as chelation or catalytic effects, thereby accelerating the aging rate of BO. This interaction may also lead to the production of gases, including toxic gases, as byproducts of corrosion and internal reactions within the BO, resulting in the buildup of pressure and potential safety hazards. Even when employing more corrosion-resistant MOCs such as SS, the catalytic effects of metal oxides on BO can pose challenges. Therefore, a comprehensive design approach, incorporating validated material selection criteria and operating conditions, is imperative for the successful commercialization of BO co-processing operations. This approach will ensure the selection of MOCs that not only withstand the corrosive nature of BO but also minimize catalytic effects and mitigate safety risks associated with gas production and buildup.

5.4. Conclusions

In this study, a series of BO aging experiments and immersion experiments (BO + steel vs. BO + synthetic corrosion products) were conducted to examine the corrosion-induced changes in BO aging. Interactions between corrosion products and BO were analyzed by various analytical techniques. Some key findings are summarized as follows:

- In the BO aging experiment at 80 °C, no significant change in pressure was observed over 168 h. Elevated temperatures (100–220°C) in shorter-duration (24 h) aging experiments resulted in increases in CO_2 and CO concentrations. This indicates that 80 °C is a suitable pre-heating temperature for BO without gas evolution.
- During the immersion experiments of BO + steel vs. BO + synthetic corrosion products at

80 °C, the BO + Fe$_2$O$_3$ trial exhibited higher CO$_2$ but lower H$_2$ concentrations compared to the BO + CS immersion, which was by the internal reactions catalyzed by Fe$_2$O$_3$. BO + SS 304L and BO + Cr$_2$O$_3$ trials showed similar H$_2$ and CO$_2$ production, suggesting a dominant catalytic effect of Cr$_2$O$_3$ on BO.

- Subsequent to aging or immersion experiments, phase separation occurred in BO, leading to the formation of a viscous bottom phase with viscosities proportional to the autoclave pressure. Higher H$_2$ and CO$_2$ production during CS immersion at 80 °C compared to 50 °C were identified, attributed to increased corrosion at the higher temperature.

- Characterization of metals and BO powders indicated the absence of a protective corrosion product layer on metal surfaces. Leached Fe ions formed chelate complexes with organic compounds in the BO, promoting phase separation. The catalytic effects of Fe ions and Fe$_2$O$_3$ intensified BO internal reactions, resulting in the production of gases such as H$_2$, CO$_2$, CO, and other light hydrocarbon gases.

- A comprehensive design approach integrating validated material selection criteria and operating conditions is essential to ensure the selected MOCs withstand the corrosive nature of BO, minimize catalytic effects, and mitigate associated safety risks.

Chapter 6. Emulsification and Corrosivity Study of Bio-oil and Vacuum Gas Oil Mixtures with A Novel Surfactant System

Abstract

Co-processing bio-oil (BO) with petroleum intermediates such as vacuum gas oil (VGO) in existing refining infrastructures provides a promising pathway to transform low-quality BO into value-added biofuels. Nevertheless, the immiscibility between BO and VGO is one of the major obstacles to BO co-processing, especially during the feeding stage of upgrading. To inject BO and VGO as a single-phase fluid and maximize their interactions, emulsification was applied to mix BO and VGO. In this study, a novel surfactant system, based on Span 80 (SP), Tween 80 (TW), and methanol (ME), was developed to suit the remedy to the immiscibility of BO and VGO. Thermogravimetric analysis (TGA), X-ray imaging, and optical microscopy were employed to examine the thermal behavior, phase stability, and microstructure of the as-developed emulsions. Immersion experiments were conducted with carbon steel (CS) strip coupons in BO/VGO emulsions at 50 °C for corrosivity assessment. Results showed that surfactant ST (a mixture of SP and TW) outranked SP and TW in stabilizing BO/VGO emulsions indicating that surfactants with a middle hydrophilic-lipophilic balance value (approximately 8) are more suitable for BO/VGO emulsions. Adding ME notably prolonged the stabilization time of BO/VGO emulsions. The addition of new mixed surfactant STM (e.g., BO:VGO:STM with a weight ratio of 1:4:0.1) resulted in the longest phase separation starting time (100 min, at 50 °C), one order of magnitude longer than that of BO:VGO as 1:4. The BO/VGO emulsion stayed single-phase for 80, 50, and 20 min when reduced the STM ratio to 0.05, 0.03, and 0.02, respectively. TGA results indicated that hydrogen transfers from VGO to BO reduced the coke formation of BO by 55 % at above 400 °C, highlighting the significance of mixing BO and VGO properly before co-processing.

Immersion experiments concluded that the addition of studied surfactants did not show prominent effects on CS corrosion in BO/VGO emulsions.

Keywords: Bio-oil, Vacuum Gas Oil, Emulsion, Surfactant, Corrosion, Co-processing

6.1. Introduction

Due to undesired properties such as low thermal stability and high corrosivity, bio-oil (BO) is being considered to be upgraded via co-processing with vacuum gas oil (VGO) in existing fluid catalytic cracking (FCC) units to produce drop-in fuels [159, 170, 171]. The co-processing strategy would expand the use of renewable energy resources with minimized capital expenditures [172]. Currently, there are three critical challenges for implementing co-processing on a large scale: low thermal stability of BO, high corrosivity of BO, and immiscibility between BO and VGO. Hence, considering all these challenges, the quality control of products, and not triggering major permitting requirements, 20 wt% BO is set to be the upper limit for current BO co-processing [66, 72, 119]. BO produced by fast pyrolysis is not miscible with non-polar petroleum hydrocarbons such as light cycle oil, VGO, and diesel due to the high contents of polar substances like water (15–30 wt%) and oxygenated compounds (e.g., organic acids, alcohols, aldehydes) [25, 28, 66, 88]. Hydrodeoxygenation (HDO) BO with an oxygen content of less than 20 wt% is reported to be miscible with VGO. Dimitriadis et al. [173] studied the miscibility between HDO BO and various fossil-based intermediates at a 30:70 v/v (HDO BO/petroleum) ratio. The HDO process reduced the oxygen content of pyrolysis BO used in this study from 33.3 wt% to 1.4 wt%. The results indicated that HDO BO was miscible with all examined refinery streams, where homogeneous mixtures were formed between HDO BO and petroleum. However, the HDO

process consumes much energy and adds additional operational costs to co-processing [63]. Thus, mass-produced pyrolysis BO has received considerable interest as a substitute for petroleum refinery feedstocks.

The immiscibility between BO and VGO hinders feeding the two liquids together as a single-phase fluid into FCC units. Bertero and Sedran [174] conducted FCC experiments of BO/VGO blends in a riser simulator reactor. The injections were accomplished by syringes to overcome the immiscibility issue, whereas it cannot be achieved at a plant scale. de Rezende Pinho et al. [91] co-processed BO and VGO in a demonstration-scale unit by feeding BO and VGO via separate feeding streams. The results showed that FCC products from separate injections of BO and VGO are comparable to those from solely refining VGO. However, modifications for FCC feeding systems are required, which increases the capital costs of adopting the BO co-processing strategy [66]. In addition, competition for hydrogen at the zeolite catalyst interface was observed during the cracking process of oxygenated components of BO [165]. For separate or segregated injections, hydrogen transfers from hydrogen-rich VGO to hydrogen-deficit BO will be incomplete due to insufficient contact between these two liquids [66]. Concerning the catalyst efficiency, oxygenates in BO adsorb more strongly on the acid sites of catalysts resulting in excessive coke formation and consequently pore blocking and lower reaction rates [165]. Yielding products with better quality and higher catalyst efficiency are expected if adequate interactions between BO and VGO are achieved.

Emulsifying BO and VGO can be a potential solution for feeding BO and VGO mixtures as a single-phase fluid into FCC units and maximizing the BO/VGO contact. To the authors' best

knowledge, no work has been done on emulsifying pyrolysis BO with VGO. BO produced by hydrothermal liquefaction (HTL) contains less oxygen (approximately 20 wt%) compared to pyrolysis BO (approximately 50 wt%) and thus has a closer polarity to VGO [175]. Ideally, the efforts required for emulsifying HTL BO and VGO would be less than that of pyrolysis BO and VGO. However, the production of HTL BO is still under development and has not been commercialized [176]. It will take substantial time to develop the supply chains for HTL BO within a co-processing strategy. Consequently, co-processing HTL BO can be seen as a long-term strategy and is not the target BO of the present work.

Researchers have improved the miscibility of BO and diesel by emulsification for direct combustion in diesel engines [1, 34, 77]. Various surfactants such as Span 80 (SP), Tween 80 (TW), Atlox 4919, and octanol were added to obtain a stable BO/diesel emulsion [36, 75, 177]. Alcohols such as methanol (ME), ethanol, and n-butanol were used as co-surfactants to improve the emulsion stability by reducing the surface tension of droplets (*i.e.*, dispersed phase), where ME had the best performance [178]. Many factors can affect the stability of BO/diesel emulsions including BO/diesel ratio, surfactant concentration, temperature, mixing method, mixing speed, mixing time, *etc* [179]. Moreover, the hydrophilic-lipophilic balance (HLB), a measurement of the degree of hydrophilic or lipophilic of a surfactant, also plays an important role in emulsion stability [180]. A surfactant with an HLB range of 4–8 (e.g., SP, HLB=4.3) is more lipophilic, which will result in a water in oil emulsion. In contrast, a surfactant with an HLB range of 8–18 (e.g., TW, HLB=15) is more hydrophilic, which is suitable for creating an oil in water emulsion [181]. The optimal HLB value for BO/diesel emulsions depends on the surfactant type, BO composition, and concentration. Farooq et al. [177] investigated the influence of HLB value (4.3–8.8) on the stability

of BO/diesel emulsions (BO/surfactant/diesel ratio: 5/5/90 wt%) and concluded that the surfactant with an HLB value of 7.3 created the most stable emulsion. Although adding more surfactant and a higher energy input (*i.e.*, higher mixing speed and longer mixing time) are expected to result in a more stable emulsion, economic factors also need to be taken into consideration for practical applications.

Since the low thermal stability and high corrosivity of BO are two major obstacles in BO co-processing, efforts have been made to improve BO stability using additives, with ME as a promising candidate. Wang et al. [151] studied the influence of ME addition on BO thermal stability and corrosivity. Adding ME improved the thermal stability (*i.e.*, decreased the aging rate) of BO. At 50 °C, the results showed that carbon steel (CS) corroded severely (greater than 1 mm/y) in BO, whereas stainless steels (SS) were not corroded. Lu et al. [84] investigated the corrosion of BO/diesel emulsions with BO concentrations of 10 and 30 wt% on mild steel and SS at up to 70 °C for 120 h. The pH of emulsions was nearly the same as BO (pH 3.2) meaning that BO/diesel emulsions contained the same concentration of dissociated hydrogen ions as BO. However, the immersion experiments concluded that the weight loss of mild steel (0.5 wt%) in BO/diesel emulsion (10 wt% BO) was one order of magnitude lower than that (6.5 wt%) in BO. It was also suggested that the low corrosion rate in BO/diesel emulsions could be caused by the continuous phase (*i.e.*, diesel) limiting the contact between the dispersed phase (*i.e.*, BO) and metal surfaces [84]. The corrosion rate of mild steel increased with the concentration of BO in BO/diesel emulsions and temperatures. SS was not found to be corroded in the emulsions. So far, there is no published information regarding the effects of ME on the corrosivity of BO/VGO emulsions.

In summary, emulsifying pyrolysis BO and VGO provides a promising pathway as a pre-treatment for co-processing. In this work, the phase stability and corrosivity of BO/VGO emulsions were investigated. A homogenizer was used to make BO/VGO emulsions with various surfactants. The emulsion made from 20/80 (wt.%/wt.%) BO/VGO served as the blank emulsion. The performance of a newly developed surfactant STM based on SP, TW, and ME was investigated in stabilizing BO/VGO emulsions. X-ray videography and optical microscopy were employed to evaluate the thermal stability (*i.e.*, phase separation starting time) and microstructure of emulsions, respectively. Thermogravimetric analysis (TGA) was employed to reveal the effect of emulsification on BO aging. Immersion corrosion experiments were conducted in the developed emulsions at 50 °C with a common FCC structural steel.

6.2. Experimental Setup

6.2.1. Materials

A BO (BTG Bioliquids), converted from pinewood by fast pyrolysis, and a typical VGO produced in Alberta, Canada were used in this study. Their properties are listed in **Table 6.1**. Fourier-transform infrared spectroscopy (FT-IR), and TGA were performed for BO and VGO to identify their functional groups and thermal behaviors, respectively. Equipment and methods used for oil characterization can be found elsewhere [151].

Table 6.1. Characteristics of BO and VGO [151].
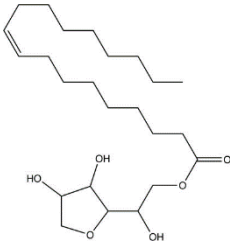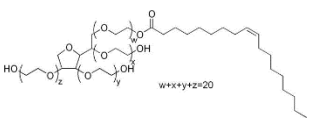
Property	BO	VGO
Viscosity[a] (at 25 °C)	171.5 cP	232.5 cP
Density[a,b]	1.20 g/mL	0.94 g/mL
Water content[a,b]	24.7 wt%	0 wt%
pH value[a,b]	2.83	
Ash content[a]	0.05 wt%	0.01 wt%
Heating value[c]	17.4 MJ/Kg	45.8 MJ/Kg
Elemental analysis[d] (wt%)	C (45.88±0.08), H (7.17±0.04), N (0.24±0.00), S (0±0.00), O[e] (46.71±0.11)	C (85.14±0.03), H (11.58±0.08), N (0.26±0.00), S (3.02±0.17), O[e] (0±0.00)

[a]Measured for multiple times until stabilized; [b]Measured at room temperature; [c]Calculated by Dulong's formula; [d]The average of four measurements; [e]By difference

Three surfactants with different HLB values were used in this study including SP (oil-soluble, TCI America™ S0060500G), TW (water-soluble, Fisher BioReagents BP338500) and a mixture of the two (ST) with an HLB equals to 8 (approximately equal affinity to oil and water) [1]. According to **Equation (6.1)** [182], surfactant ST was prepared by mixing 65.4 g of SP and 34.6 g of TW and stirring for 60 min. ME (99.9% purity, Fisher Chemical™ BPA4544) was used as a co-surfactant to further stabilize emulsions. Properties of additives are listed in **Table 6.2**.

$$\text{HLB (ST)} = \frac{\text{Mass (SP)} \times \text{HLB (SP)} + \text{Mass (TW)} \times \text{HLB (TW)}}{\text{Mass (SP)} + \text{Mass (TW)}} \qquad \textbf{Equation (6.1)}$$

Table 6.2. Properties of the surfactants used in this study [1, 182, 183].

Surfactant	SP	TW	ST	ME
Chemical structure				
Chemical formular	$C_{24}H_{44}O_6$	$C_{64}H_{124}O_{26}$		CH_4O
MW (g/mol)	428.6	1310	558.7	32.04
Color	Brown	Yellow		
Density[a] (g/mL)	0.99	1.08	1.02	0.79
Viscosity[b] (cP)	348.7	196.2	229.4	0.445
Hydrophilic group	Sorbitan	Polyether		
Lipophilic group	Oleic acid	Oleic acid		
HLB value	4.3	15	8	

[a]Measured at room temperature for multiple times until stabilized; [b]Measured at 40 °C for multiple times until stabilized

6.2.2. BO/VGO Emulsification

BO/VGO emulsions were made by a homogenizer (IKA-T18) with a BO concentration of 20 wt% (**Fig. 6.1**a). The homogenizer ran at 10,000 rpm for 10 min. The total weight of 100 g emulsion was made each time in a wide-mouth jar (capacity 120 mL, diameter 5 cm). Prior to homogenizing,

BO and VGO were heated to 50 °C. Surfactants (SP, ST, or TW) and ME were gradually dropped into BO/VGO mixtures during the homogenization process. If present, the surfactant or ME concentration was 10 wt% of BO to limit the cost of additives. **Table 6.3** lists the composition of emulsions used in this study.

(a) Homogenization   **(b) X-ray imaging system**   **(c) Immersion experiments**
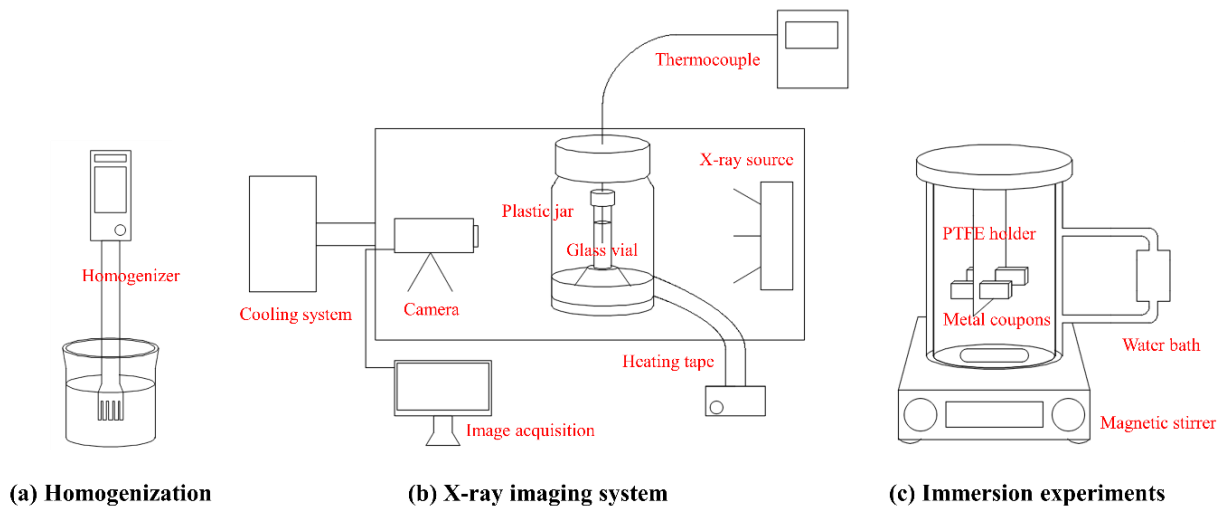
Fig. 6.1. Schematics of: (a) creating BO/VGO emulsions by homogenization; (b) determining the phase separation starting time of as-developed emulsions by X-ray imaging; and (c) immersion experiments in BO/VGO emulsions.

Table 6.3. Compositions (g) of BO/VGO emulsions.

Code name	BO	VGO	SP	ST	TW	ME	Emulsion type
1:4	20	80	-	-	-	-	
1:4:0.1SP	20	80	2	-	-	-	BO-in-VGO
1:4:0.1SP:0.1ME	20	80	2	-	-	2	BO-in-VGO
1:4:0.1ST	20	80	-	2	-		Complex
1:4:0.1ST:0.1ME	20	80	-	2	-	2	Complex
1:4:0.1TW	20	80	-	-	2	-	VGO-in-BO
1:4:0.1TW:0.1ME	20	80	-	-	2	2	VGO-in-BO

6.2.3. Emulsion Stability Measurements

The stability of BO/VGO emulsions was evaluated from two aspects—aging of emulsions determined by TGA and phase separation time of emulsions revealed by X-ray imaging. For aging experiments, emulsions were contained in a water-jacketed beaker to maintain their temperatures at 50 °C while being stirred at a rate of 400 rpm to keep from phase separation. Emulsion samples, taken at the beginning (*i.e.*, 0 h) and after aging for 24, 96, and 168 h were conducted for TGA. To evaluate the phase stability of emulsions, X-ray equipment was employed to image emulsions at a time interval of 10 min. As indicated in **Fig. 6.1**b, emulsions were stored in a glass vial (capacity 12 mL, diameter 2.5 cm) which was then put inside a plastic jar (capacity 125 mL, diameter 6.4 cm) coated with a silicone heating tape (Grainger WWG13P853). The temperature inside the jar was kept at 50 °C. A thermocouple was inserted into the glass vial for monitoring the temperature of emulsions. The operation and setup of the X-ray equipment are available elsewhere [184, 185]. Optical micrographs (OM) of emulsions were also taken to elucidate the effect of emulsion

microstructures on the stability of emulsions.

6.2.4. Immersion Experiments

A common FCC structural material, CS, was used for immersion experiments in BO/VGO emulsions, and its corresponding chemical composition can be found elsewhere [151]. Immersion experiments followed the procedures of ASTM G31 [94]. CS strip coupons ($1 \times 1/4 \times 1/16$ in^3) were polished to a 600-grit finish before immersion experiments. CS coupons were held by PTFE holders (**Fig. 6.1**c) and immersed in a water-jacketed beaker filled with BO/VGO emulsions (**Table 6.3**). The immersion experiments were repeated 4 times at 50 °C for 168 h. After immersion experiments, oils and corrosion products on CS coupon surfaces were gently removed by Q-tips soaked with toluene (dissolving VGO) and ethanol (dissolving BO). CS coupons were then cleaned in an ultrasonic bath with toluene, ethanol, and acetone for 10 min each before being rinsed with deionized water and air-dried. The corrosion rate (in mm/y) was calculated based on the weight loss of CS coupons.

6.3. Results and Discussion

FT-IR measurements were conducted for BO and VGO to compare their complexities in terms of functional groups existing in the two oils. **Fig. 6.2** shows the FT-IR spectrum of VGO which is much simpler compared to BO [151]. Primarily, aliphatic groups were identified at the absorbance frequencies (cm^{-1}) of 2924 and 2853 (symmetric and asymmetric stretching vibration of CH_2 and CH_3 aliphatic groups), 1462 (bending vibrations of CH_2 and CH_3 aliphatic groups), and 1377 (symmetric deformation of C–H in methyl groups) [38, 42]. This confirms that VGO, as a mixture of non-polar aliphatic hydrocarbons, is not miscible with BO containing mainly polar oxygenated

compounds (**Table 6.1**).
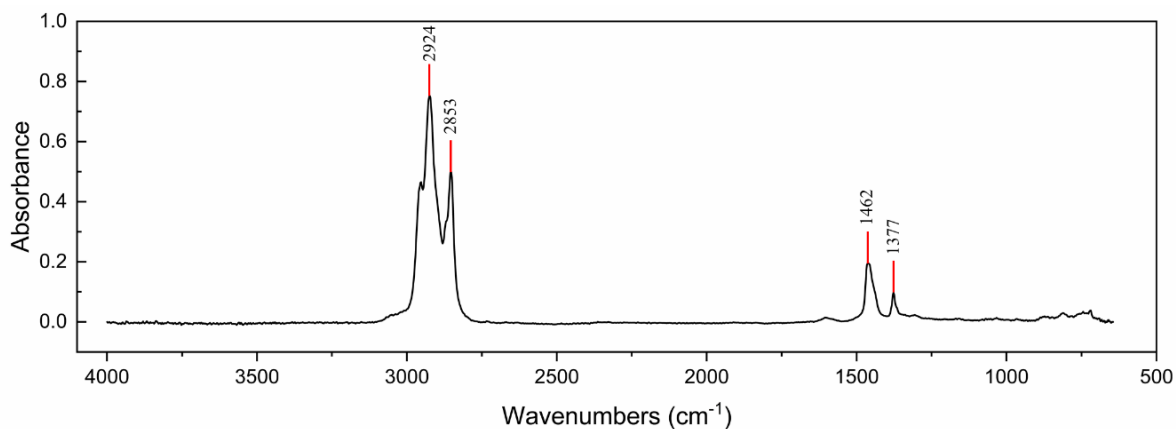
Fig. 6.2. FT-IR spectrum of the VGO used in this study.

6.3.1. Thermal Behaviors of BO/VGO Emulsions

The thermal behaviors of BO and VGO were measured by TGA to further compare their properties. As indicated in **Fig. 6.3**a, the relationships between oil sample remaining mass (*i.e.*, wt% unevaporated) and temperature (30–750 °C) in an argon atmosphere were plotted as TG curves. The TG curve of VGO possessed a typical plateau-slope-plateau shape, where the majority of chemical substances in VGO had boiling points ranging from 200 to 350 °C. In contrast, the TG curve of BO showed a continuous declining trend presenting that BO contained organic compounds with a wide range of boiling points. The first derivatives of TG curves, representing the rate of mass loss versus temperature, were plotted as DTG curves, where the highest mass-loss rate of BO and VGO appeared at 100 and 270 °C, respectively.
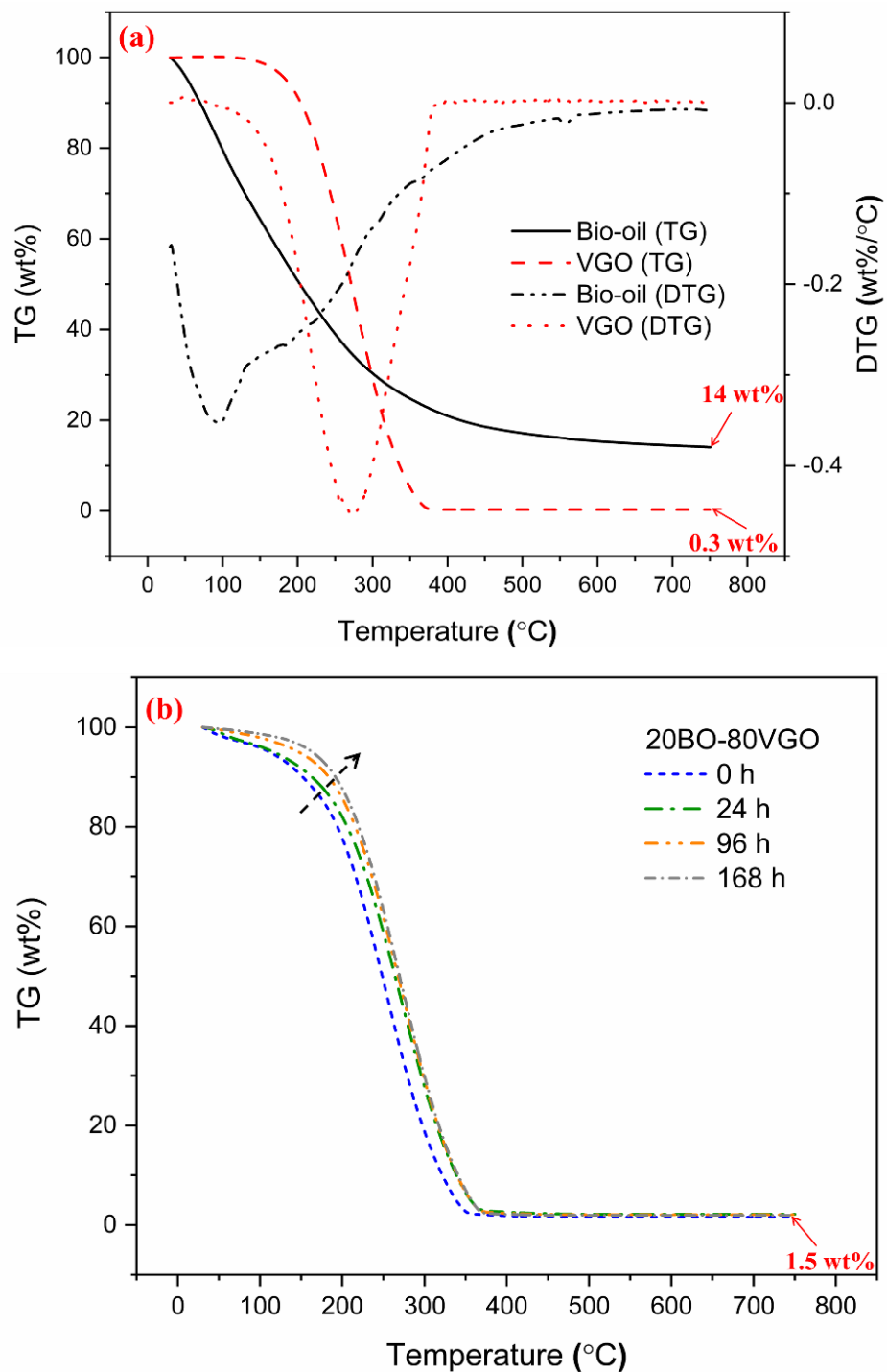
Fig. 6.3. TGA results of oil samples heated from 30 to 750 °C: (a) TG and DTG curves of BO and VGO; (b) TG curves of 1:4 emulsion samples after aging for 0, 24, 96, and 168 h at 50 °C (dashed arrows present the shift due to aging).

Fig. 6.3b depicts TG curves of the 1:4 unaged emulsion sample (*i.e.*, "0 h") and emulsion samples after aging for 24, 96 and 168 h at 50 °C. TG curves of aged and unaged 1:4 emulsion samples showed similar trends—a slow decrease (30–150 °C) followed by a rapid decline (150–350 °C) until reaching a plateau. This demonstrates one of the advantages of BO co-processing—a clearly defined operating temperature can be set where the conversion rate can no longer increase as further increasing temperature. As indicated by the dashed arrow, the TG curves of aged emulsion samples (*i.e.*, "24 h" "96 h" and "168 h") shifted to the upper right suggesting that some light components of BO transformed to higher-molecular-weight compounds during aging. The distance between the TG curves of "0 h" and "24 h" was larger than that between "24 h" and "96 h" indicating that the majority of the aging process had already completed after 24 h. The discrepancies in TG curves between the unaged and aged 1:4 emulsion samples diminished at temperatures above 400 °C. As a result, the aging at 50 °C did not affect the final weight percentage of the 1:4 emulsion prominently.

As shown in **Fig. 6.3**a–b, the final weight percentage of "BO", "VGO", and "0 h" samples were 14, 0.3 and 1.5 wt%, respectively. Interestingly, the final weight percentage of the "0 h" sample contributed by BO (1.26 wt%, calculated by subtracting the contribution of VGO, 0.24 wt%, from the final weight percentage of "0 h") was 55% lower than its expected value (2.80 wt%, 0.2 times of the final weight percentage of "BO"). This indicated that during the heating process of TGA, hydrogen transfer from VGO to BO occurred preventing some fractions in BO from forming substances with higher boiling points (greater than 750 °C). Another benefit of co-processing well-mixed BO/VGO feeds has been reinforced according to TGA results—hydrogen transfers from VGO to BO would increase the conversion rate of BO to biofuel and reduce the deactivation of

catalysts by gummy BO coke at the FCC temperature (approximately 500 °C).

6.3.2. Phase Stability of BO/VGO Emulsions

X-ray imaging was employed to examine the phase separation of emulsions stored at 50 °C. The X-ray images of emulsion samples, 1:4 and 1:4:0.1ST:0.1ME, are presented in **Fig. 6.4** and **Fig. 6.5**. The phase separation starting time was identified when the first thin layer of BO settled at the bottom of the glass vial, as indicated in Figs 4b and 5b. The just-made emulsion samples (*i.e.*, at the time "0 min") showed an evenly distributed green color (**Fig. 6.4**a and **Fig. 6.5**a). After 10 min, the phase separation of 1:4 started (**Fig. 6.4**b), at which a thin dark green layer was observed at the glass vial bottom. The height of the bottom BO phase continued increasing (**Fig. 6.4**c). After 60 min, around 80 wt% of BO separated from the emulsion (**Fig. 6.4**d). In contrast, 1:4:0.1ST:0.1ME sustained as a single-phase, one order of magnitude longer (100 min) than 1:4 (**Fig. 6.5**b). After 420 min, approximately 60 wt% of BO coalesced and settled at the bottom (**Fig. 6.5**d).
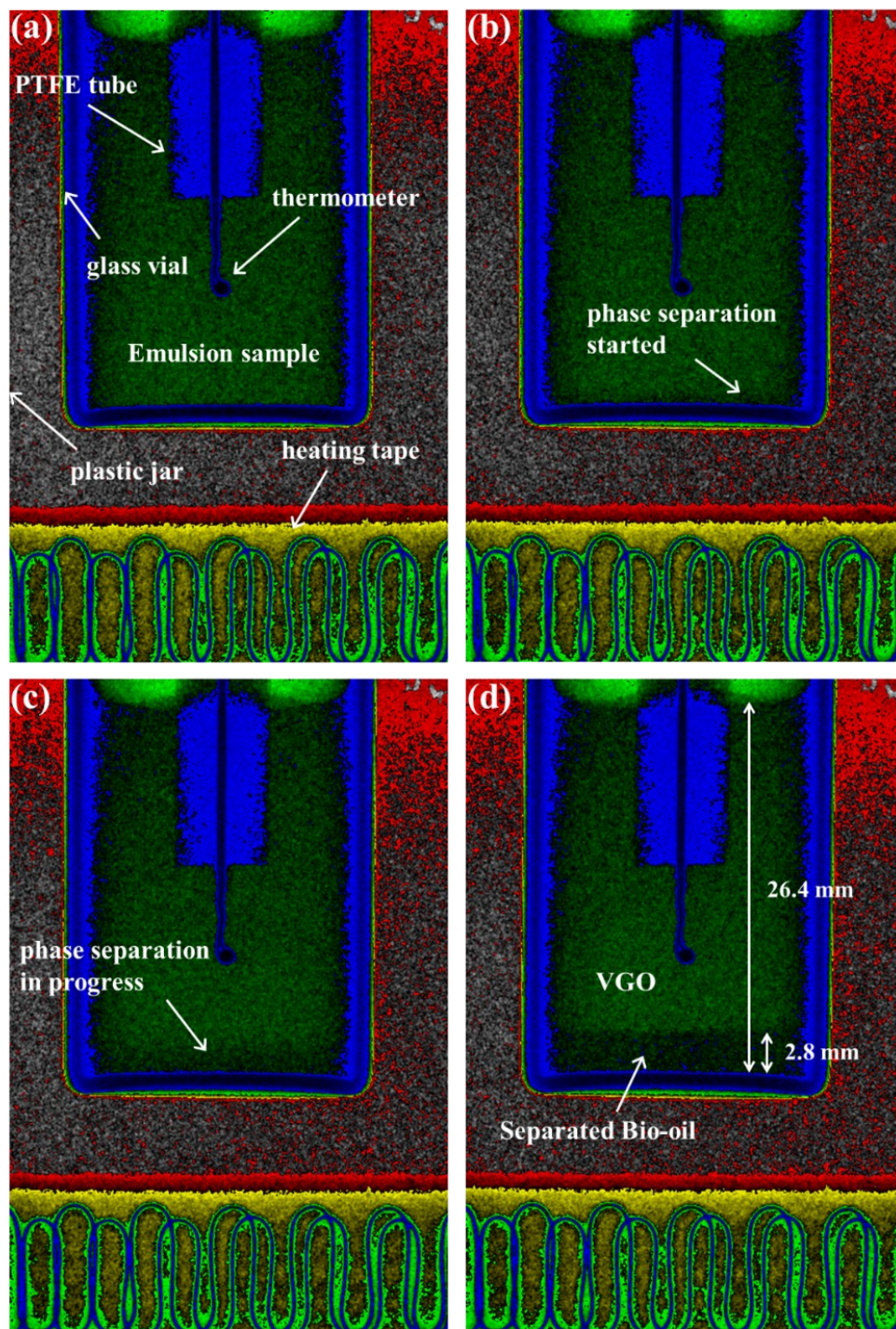
Fig. 6.4. X-ray images of the 1:4 emulsion at 50 °C: (a) just made; (b) after 10 min; (c) after 20 min; and (d) after 60 min.
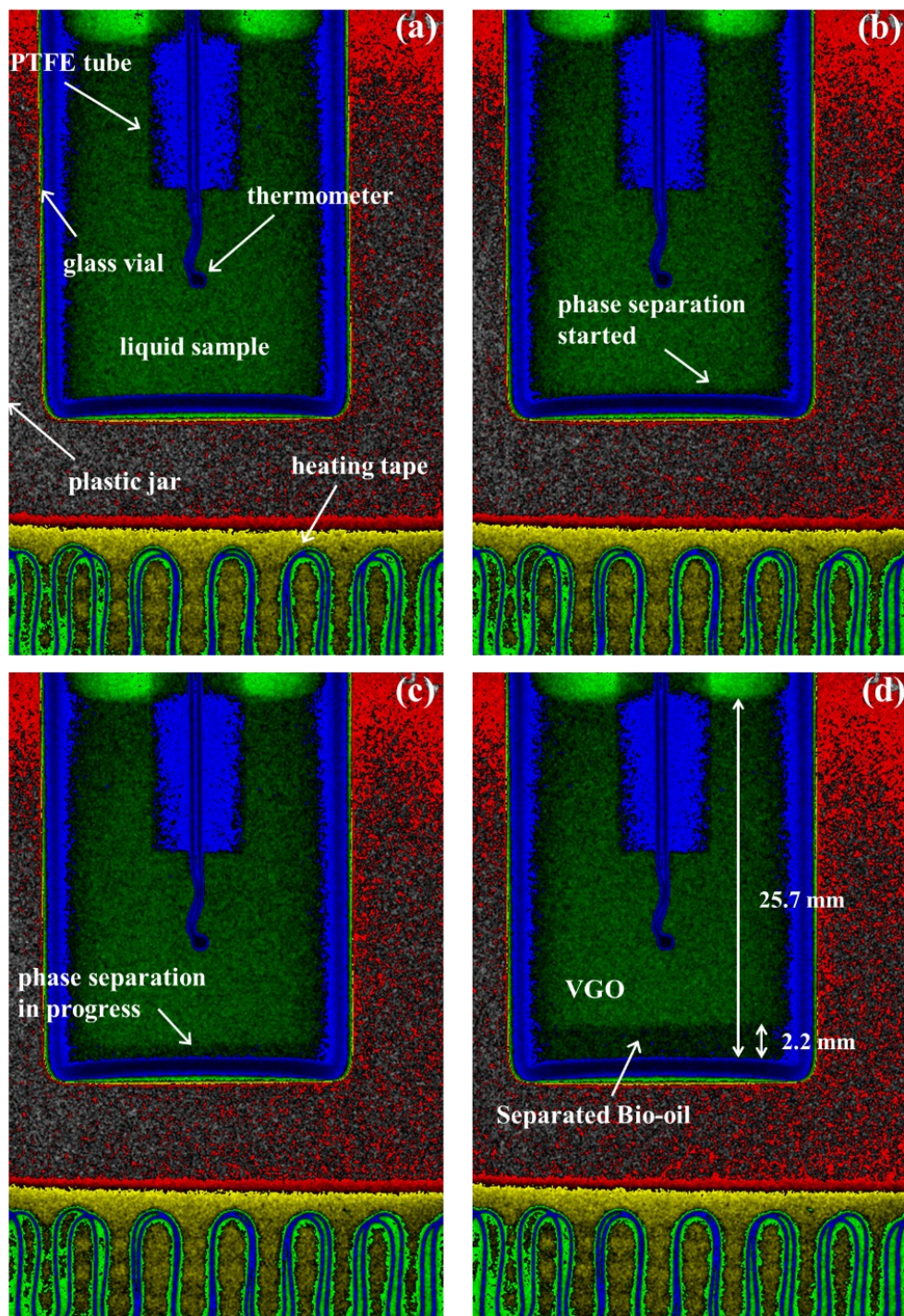
Fig. 6.5. X-ray images of 1:4:0.1ST:0.1ME emulsion at 50 °C: (a) just made; (b) after 100 min; (c) after 240 min; and (d) after 420 min.

Fig. 6.6 summarizes the phase separation starting time as well as the separation rate of emulsion samples listed in **Table 6.3**. Compared to the emulsion sample without surfactant addition (*i.e.*, 1:4), additions of SP, ST, and TW prolonged the phase separation starting time by 4, 6, and 2 times, respectively. ST had the best performance in stabilizing BO/VGO emulsions among the three tested surfactants. Moreover, adding ME further improved the stability of emulsions. For instance, 1:4:0.1SP:0.1ME could stay stable for 70 min, 30 min longer than 1:4:0.1SP. This suggested that ME could stabilize BO/VGO emulsions by reducing the surface energy between dispersed and continuous phases [178]. Among all emulsion samples, 1:4:0.1ST:0.1ME held the longest phase separation starting time.
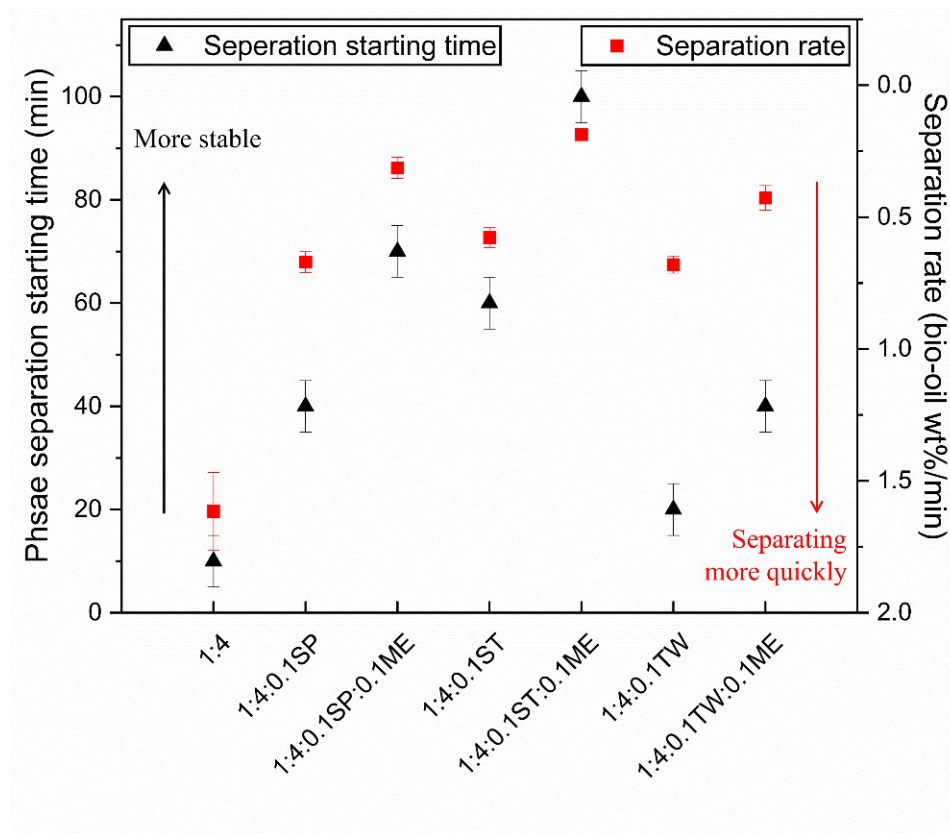
Fig. 6.6. The phase separation of BO/VGO emulsions. The phase separation starting time, t_0 (represented by the symbol of ▲), was determined when the first thin layer of BO settled at the bottom of the glass vial (**Fig. 6.4**b and **Fig. 6.5**b). The phase separation rate (represented by the symbol of ■) was calculated by dividing the weight percentage of separated BO relative to the total BO at t_1 by the elapsed time since t_0 (i.e., t_1-t_0).

The phase separation rate (wt%/min) after the phase separation starting time (t_0) was calculated by dividing the weight percentage of separated BO relative to the total BO at the time, t_1, by the elapsed time since t_0 (*i.e.*, t_1-t_0). As indicated in **Fig. 6.6**, 1:4 separated quickly at a rate of 1.6 wt%/min. Mann-Whitney U Test (MWUT) was performed to examine the significance of the difference in the phase separation rate between the emulsion without surfactant/ME addition (*i.e.*, 1:4) and the emulsions with surfactant/ME addition (*i.e.*, 6 emulsion samples except 1:4). A two-

sided significance level of 0.05 was used. The calculated p-value was 0.022 (less than 0.05), indicating the difference was significant—the addition of surfactant/ME reduced the phase separation rate. Compared to 1:4, adding surfactant (SP, ST, or TW) reduced the phase separation rate by around 2.5 times. Kruskal-Wallis H Test (KWHT) was performed among the three emulsion samples with only surfactant added (*i.e.*, 1:4:0.1SP, 1:4:0.1ST, 1:4:0.1TW)) with a two-sided significance level of 0.05. The calculated p-value was 0.156 (greater than 0.05), showing the surfactant type did not affect the phase separation rate significantly. MWUT was also performed for emulsions with only surfactant added (*i.e.*, 1:4:0.1SP, 1:4:0.1ST, 1:4:0.1TW) and emulsions with both surfactant and ME added (*i.e.*, 1:4:0.1SP:0.1ME, 1:4:0.1ST:0.1ME, 1:4:0.1TW:0.1ME). The calculated p-value was 0.002, indicating the addition of ME further reduced the separation rate. For example, the phase separation rate of 1:4:0.1ST:0.1ME was 9 times and 3 times slower than those of 1:4 and 1:4:0.1ST, respectively.

6.3.3. Microstructures of BO/VGO Emulsions

To reveal the microstructure of BO, VGO, and BO/VGO emulsions (at time 0 h), OM of oil samples were taken and presented in **Fig. 6.7**. BO showed a clean and homogeneous liquid phase with some dust and air bubbles trapped inside (**Fig. 6.7**a). In comparison, VGO as a mixture of long-chain hydrocarbons had textured microstructures (**Fig. 6.7**b). **Fig. 6.7**c indicates that 1:4 contained thin droplets with a wide range of size distribution, where some of the droplets had already flocculated and coalesced. This explained why 1:4 could only stay stable for 10 min. 1:4:0.1TW had droplets with irregular shapes (**Fig. 6.7**f), which led to its stability (stable for 20 min) the worst among surfactant-added emulsions. The droplets in 1:4:0.1SP were nearly round (minimized surface energy) resulting in its stable time extended to 40 min (**Fig. 6.7**d). As shown

in **Fig. 6.7**e, droplets in 1:4:0.1ST (stable for 100 min) were round, dense, and evenly distributed, which explained why the surfactant ST performed better than others. The diameters of some typical droplets in 1:4:0.1SP and 1:4:0.1ST are indicated in **Fig. 6.7**d and **Fig. 6.7**e, respectively. Although the droplet size distributions of 1:4:0.1SP and 1:4:0.1ST are similar, the droplet quantity of the latter is much more than that of the former. This finding concludes that surfactants with a middle HLB value (around 8) have superior performance in stabilizing BO/petroleum emulsions [177].
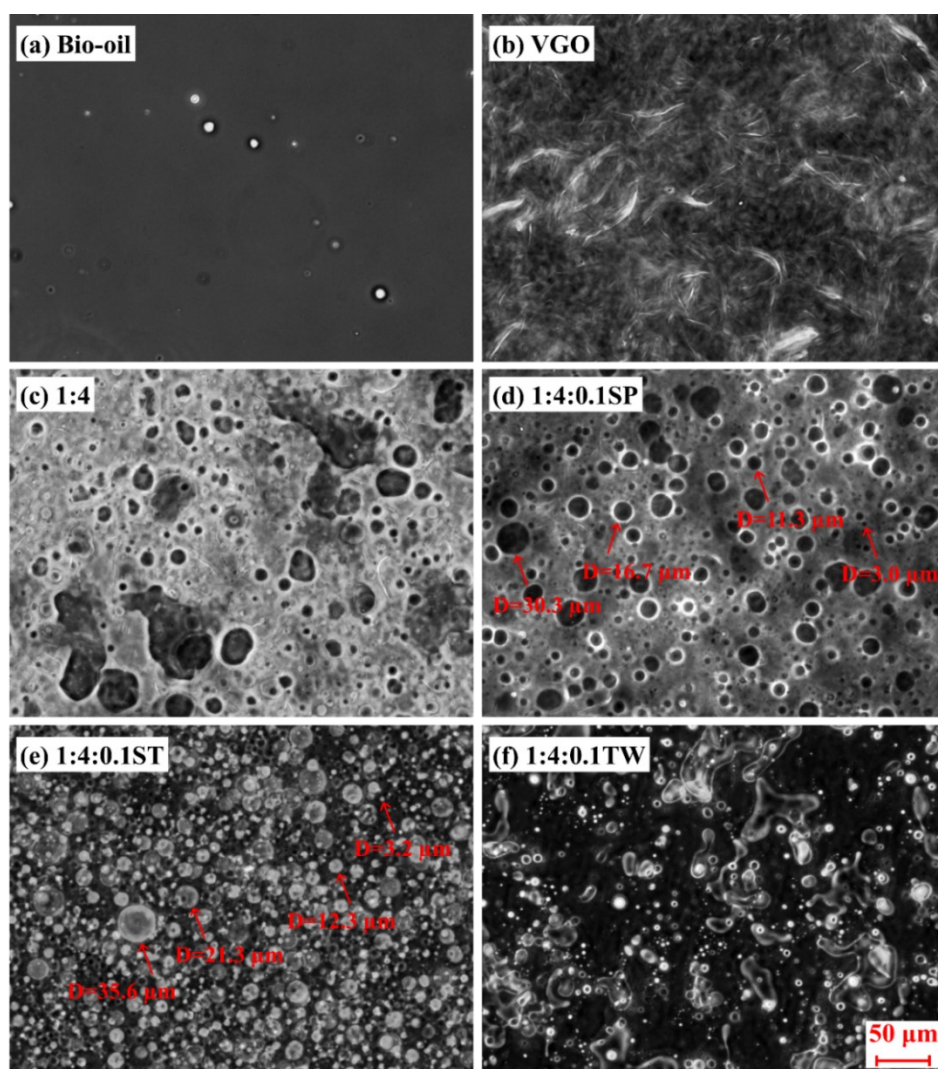
Fig. 6.7. Optical micrographs of: (a) BO; (b) VGO; and (c) 1:4; (d) 1:4:0.1SP; (e) 1:4:0.1ST; and (f) 1:4:0.1TW emulsions. Red arrows show the diameters of some typical droplets.

6.3.4. Corrosivity of BO/VGO Emulsions

Corrosivity evaluations on BO/VGO emulsions were conducted by immersing CS coupons into emulsion samples listed in **Table 6.3** for 24 h at 50 °C. **Fig. 6.8** shows the corrosion rates of CS in BO/VGO emulsions. In order to statistically justify the significance of the difference between the corrosion rates, KWHT with a two-sided significance level of 0.05 was performed for the corrosion data indicated in **Fig. 6.8**. The calculated *p*-value was 0.222 showing the addition of surfactant and ME did not affect the CS corrosion rate significantly. Adding SP and ST reduced the corrosion rate of CS slightly. For instance, the corrosion rate of CS in 1:4:0.1SP (1.8 mm/y) was slightly lower than that in 1:4 (2.2 mm/y). On the contrary, the addition of TW and ME increased the corrosivity of emulsions marginally (e.g., 2.3 mm/y in 1:4:0.1ST:0.1ME). Overall, severe corrosion of CS was identified in BO/VGO emulsions despite the type of surfactant added. This agreed with the previous finding that BO causes excessive corrosion to carbon steel. Cautions must also be taken when dealing with BO/VGO emulsions.
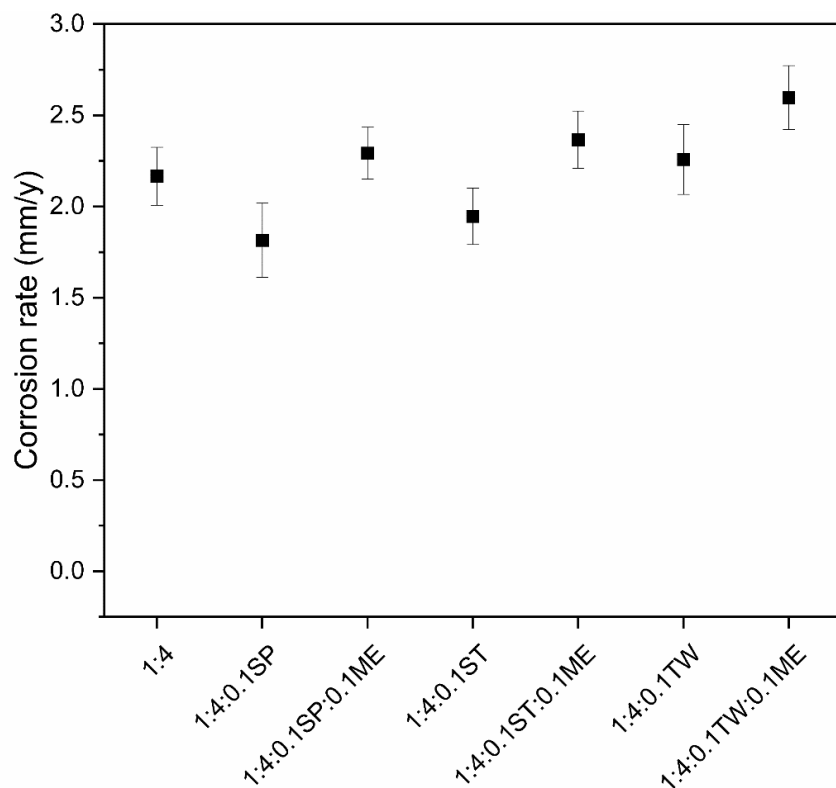
Fig. 6.8. Corrosion rates of CS coupons in BO/VGO immersions (**Table 6.3**). Immersion experiments were conducted at 50 °C for 24 h.

6.3.5. Optimization on the Surfactant Ratio

Based on the above discussion, a mixture of ST and ME (*i.e.*, STM, 1:1 weight ratio) served as the optimal surfactant in stabilizing BO/VGO emulsions, where 1:4:0.2STM (equivalent to 1:4:0.1ST:0.1ME) stayed single-phase for 100 min at 50 °C. To balance the stabilization time and economic consideration, phase stability measurements were also conducted for emulsions with reduced STM ratios, as listed in **Table 6.4**. As indicated in **Fig. 6.9**, reducing the STM ratio from 0.2 to 0.1 did not affect the stability of the emulsion meaning that the critical micelle concentration of STM had reached at 0.1. Further reducing the STM ratio to 0.05 resulted in a 20 min decrease in the stabilization time. The phase separation starting time of BO/VGO emulsions with 0.03 and

0.02 STM were 50 and 20 min, respectively. The optimal surfactant ratio depends on how long it requires from homogenization of BO/VGO mixtures to injection of BO/VGO emulsions into the riser of FCC units. The phase stability could be dramatically reduced at the practical feeding temperatures (150–300 °C). Further investigations are required for BO/VGO emulsions at higher temperatures.

Table 6.4. Compositions (g) of STM added BO/VGO emulsions.

Code name	BO	VGO	ST	ME
1:4:0.2STM	20	80	2	2
1:4:0.1STM	20	80	1	1
1:4:0.05STM	20	80	0.5	0.5
1:4:0.03STM	20	80	0.3	0.3
1:4:0.02STM	20	80	0.2	0.2
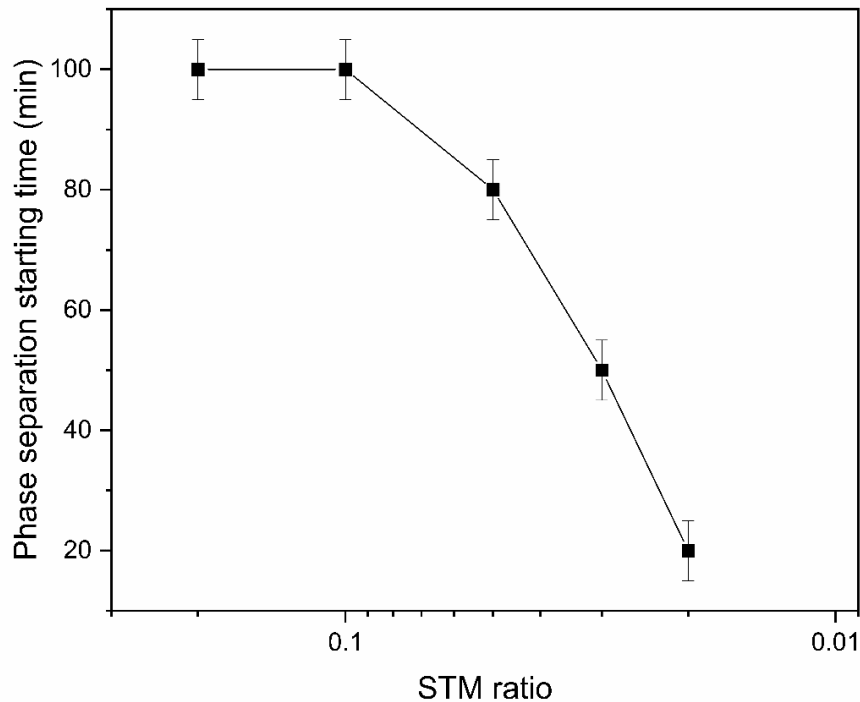
Fig. 6.9. The phase separation starting time of BO/VGO emulsions with various STM ratios (0.2, 0.1, 0.05, 0.03, and 0.02). The detailed composition of the emulsions is shown in **Table 6.4**.

6.4. Conclusions

The phase stability and corrosivity of BO/VGO (1:4 wt.%/wt.%) emulsions were evaluated in this study. The emulsification of BO and VGO using surfactants with different HLB values and a co-surfactant (ME) was performed at 50 °C. The results showed that ST with a middle HLB value performed the best in stabilizing BO/VGO emulsions among all tested surfactants. The addition of ME further improved the stability of the emulsions. OM indicated that emulsions containing dense, round and evenly distributed droplets had a longer stable time. A newly developed surfactant, STM (a mixture of SP, TW, and ME), was used to suit the remedy to the immiscibility of BO and VGO. Thereinto, 1:4:0.1STM held the longest phase separation starting time (100 min), one order of magnitude longer than that of 1:4. The stabilization time of BO/VGO emulsions with STM ratios

of 0.05, 0.03, and 0.02 was found to be 80, 50, and 20 min. TGA results indicated that the aging of BO could be partially offset by hydrogen transfer from hydrogen-rich VGO to hydrogen-deficit BO. Emulsifying BO and VGO reduced 55% of solid char formation of BO at above 400 °C, emphasizing the significance of mixing BO and VGO properly before co-processing. Additions of surfactant and co-surfactant did not affect on CS corrosion significantly. Further investigations are required to develop stable and less-corrosive BO/VGO emulsions at FCC preheating temperatures (*i.e.*, 150–300 °C).

Chapter 7. Summary and Future Prospects

7.1. Summary

Co-processing BO with VGO within petroleum refineries stands as a promising strategy for transforming low-grade BO into high-value drop-in fuels. However, this method encounters three primary obstacles: the inherently low thermal stability of BO, its corrosive effects on construction materials, and the lack of miscibility between BO and VGO. The research detailed in this thesis was undertaken to tackle these challenges, with the overarching goal of advancing BO co-processing strategies.

The thermal stability of BO was investigated through aging experiments conducted at temperatures of up to 80 °C for durations of up to 168 hours. Methanol was added into BO, with concentrations of up to 20 wt%. The experimental findings revealed that the addition of methanol effectively mitigated the aging process of bio-oil. However, CS experienced significant corrosion (> 1 mm/y) under the studied temperatures, and the presence of methanol accelerated its corrosion rate. SS 304L demonstrated a moderate corrosion rate (> 0.1 mm/y) at 80°C, while SS 316L displayed minimal corrosion (< 0.1 mm/y) across the range of temperatures studied.

Modified electrochemical techniques tailored to accommodate low-conductivity BO environments were employed to investigate the corrosion behavior of CS in BO. An equivalent circuit model, incorporating chelation processes within the corrosion mechanisms, was developed to accurately interpret the experimental results. The corrosion data obtained from electrochemical measurements were corroborated by parallel immersion experiments. The gases generated from BO aging and steel immersion experiments were analyzed using gas chromatography, revealing the presence of

various gases such as H_2, CO, CO_2, and light hydrocarbons. Notably, the corrosion of steel was found to expedite the aging process of BO. Interactions between corrosion products and BO were analyzed by various analytical techniques. It was observed that leached Fe ions formed chelate complexes with organic compounds present in the BO, thereby promoting phase separation. Furthermore, the catalytic effects of Fe ions and Fe_2O_3 intensified the internal reactions within the BO, leading to the production of gases.

Lastly, emulsification incorporating various surfactants was implemented as a solution to address the immiscibility of BO and vacuum VGO. The phase stability and corrosive properties of BO/VGO (1:4 wt%/wt%) emulsions were assessed. Experimental findings demonstrated the successful creation of a stable BO/VGO emulsion, sustaining stability for up to 100 minutes at 50°C with the addition of 2 wt% surfactant. Subsequent immersion experiments conducted within the BO/VGO emulsions revealed no significant alteration in corrosion rates compared to immersion experiments conducted solely in BO.

7.2. Future Prospects

Despite significant efforts aimed at advancing the BO co-processing strategy, notable knowledge gaps persist regarding the systematic design of co-processing processes that incorporate considerations of safety and feasibility. Consequently, the following recommendations are proposed for further research and development in the field of BO co-processing:

1. Critical Methanol Addition Concentration. Investigate the optimal concentration of methanol required to stabilize bio-oil and prevent undesired aging. This entails conducting systematic

experiments to determine the threshold concentration at which methanol effectively mitigates aging without adversely impacting product quality or process economics.

2. Feasible Preheating Temperature. Determine the most suitable pre-heating temperature for BO to achieve the desired conversion ratio during co-processing. This involves assessing the impact of pre-heating temperature on process kinetics, product yields, and energy consumption to identify the optimal operating conditions.

3. Appropriate Injection Strategy. Explore different injection strategies for introducing BO into the co-processing unit, considering factors such as mixing efficiency, and reactor design. Comparative studies can help identify the most effective injection method for maximizing conversion efficiency and minimizing operational challenges.

4. Minimum Hydrotreating Degree. Determine the minimum level of hydrotreating required for BO to achieve an acceptable corrosion rate on construction materials during co-processing. This necessitates comprehensive corrosion studies using various hydrotreated BO to establish the threshold hydrotreating degree that ensures operational safety while minimizing the cost.

5. Eco-technical Analysis. Conduct an integrated eco-technical analysis to evaluate the environmental and technical implications of co-processing strategies, including methanol addition, surfactant use, emulsification, energy consumption, product quality and overall co-processing operations.

Bibliography

[1] L. Leng, H. Li, X. Yuan, W. Zhou, H. Huang, Bio-oil upgrading by emulsification/microemulsification: A review, Energy 161 (2018) 214-232.

[2] T. Wang, Y. Zhai, Y. Zhu, C. Li, G. Zeng, A review of the hydrothermal carbonization of biomass waste for hydrochar formation: Process conditions, fundamentals, and physicochemical properties, Renewable and Sustainable Energy Reviews 90 (2018) 223-247.

[3] U. Dtie, Converting waste agricultural biomass into a resource, Compendium of technologies. Osaka, United Nations Environment Programme (2009).

[4] A.M.S. Chun, I.E. Brisson, Ground Rules in Humanitarian Design, John Wiley & Sons2015.

[5] N. Tripathi, C.D. Hills, R.S. Singh, C.J. Atkinson, Biomass waste utilisation in low-carbon products: harnessing a major potential resource, npj Climate and Atmospheric Science 2(1) (2019) 1-10.

[6] L. Nazari, S. Sarathy, D. Santoro, D. Ho, M. Ray, C.C. Xu, Recent advances in energy recovery from wastewater sludge, Direct thermochemical liquefaction for energy applications, Elsevier2018, pp. 67-100.

[7] C. Yang, L. Jia, C. Chen, G. Liu, W. Fang, Bio-oil from hydro-liquefaction of Dunaliella salina over Ni/REHY catalyst, Bioresource technology 102(6) (2011) 4580-4584.

[8] C. Xu, T. Etcheverry, Hydro-liquefaction of woody biomass in sub-and super-critical ethanol with iron-based catalysts, Fuel 87(3) (2008) 335-345.

[9] Y. Yang, A. Gilbert, C. Xu, Production of bio‐crude from forestry waste by hydro‐liquefaction in sub‐/super‐critical methanol, AIChE journal 55(3) (2009) 807-819.

[10] H.-j. Huang, X.-z. Yuan, Recent progress in the direct liquefaction of typical biomass, Progress in Energy and Combustion Science 49 (2015) 59-80.

[11] U. Jena, K. Das, Comparative evaluation of thermochemical liquefaction and pyrolysis for bio-oil production from microalgae, Energy & fuels 25(11) (2011) 5472-5482.

[12] L. Zhang, S.-C. Kong, Multicomponent vaporization modeling of bio-oil and its mixtures with other fuels, Fuel 95 (2012) 471-480.

[13] D. Kirk, Z. Li, D. Fuleki, P. Patnaik, Materials compatibility with pyrolysis Biofuel, Turbo Expo: Power for Land, Sea, and Air, American Society of Mechanical Engineers, 2001, p. V002T01A006.

[14] J.M. Jarvis, K.O. Albrecht, J.M. Billing, A.J. Schmidt, R.T. Hallen, T. Schaub, Assessment of hydrotreatment for hydrothermal liquefaction biocrudes from sewage sludge, microalgae, and pine feedstocks, Energy Fuels 32(8) (2018) 8483-8493.

[15] J. Yan, P. Alvfors, L. Eidensten, G. Svedberg, A future for biomass, Mechanical Engineering 119(10) (1997) 94.

[16] D. Mohan, C.U. Pittman Jr, P.H. Steele, Pyrolysis of wood/biomass for bio-oil: a critical review, Energy & fuels 20(3) (2006) 848-889.

[17] X. Han, H. Wang, Y. Zeng, J. Liu, Advancing the application of bio-oils by co-processing with petroleum intermediates: A review, Energy Conversion and Management: X (2020) 100069.

[18] R. Yuste, Biofuels production in conventional oil refineries through bio-oil co-processing, Jointworkshop of ENMIX, FASTCARD, CASCATBEL, BIOGO 21 (2016).

[19] J.A. Melero, G. Calleja, A. Garcia, M. Clavero, E.A. Hernandez, R. Miravalles, T. Galindo, Storage stability and corrosion studies of renewable raw materials and petrol mixtures: A key issue for their co-processing in refinery units, Fuel 89(3) (2010) 554-562.

[20] J. Axsen, M. WOLINETZ, The Renewable and Low Carbon Fuel Requirement Regulation, Navius Research, 2014.

[21] A.E. Farrell, D. Sperling, A. Brandt, A. Eggert, A. Farrell, B. Haya, J. Hughes, B. Jenkins, A. Jones, D. Kammen, A low-carbon fuel standard for California, Part I (2007).

[22] A. Undri, M. Abou-Zaid, C. Briens, F. Berruti, L. Rosi, M. Bartoli, M. Frediani, P. Frediani, A simple procedure for chromatographic analysis of bio-oils from pyrolysis, Journal of Analytical Applied Pyrolysis 114 (2015) 208-221.

[23] T. Ba, A. Chaala, M. Garcia-Perez, C. Roy, Colloidal properties of bio-oils obtained by vacuum pyrolysis of softwood bark. Storage stability, Energy & fuels 18(1) (2004) 188-201.

[24] J.P. Diebold, A review of the chemical and physical mechanisms of the storage stability of fast pyrolysis bio-oils, National Renewable Energy Lab., Golden, CO (US), 1999.

[25] A. Oasmaa, C. Peacocke, A guide to physical property characterisation of biomass-derived fast pyrolysis liquids, Technical Research Centre of Finland Espoo2001.

[26] A. Oasmaa, E. Kuoppala, Fast pyrolysis of forestry residue. 3. Storage stability of liquid fuel, Energy & Fuels 17(4) (2003) 1075-1084.

[27] M. Boucher, A. Chaala, H. Pakdel, C. Roy, Bio-oils obtained by vacuum pyrolysis of softwood bark as a liquid fuel for gas turbines. Part II: Stability and ageing of bio-oil and its blends with methanol and a pyrolytic aqueous phase, Biomass and Bioenergy 19(5) (2000) 351-361.

[28] R.J. Westerhof, N.J. Kuipers, S.R. Kersten, W.P. van Swaaij, Controlling the water content of biomass fast pyrolysis oil, Industrial & Engineering Chemistry Research 46(26) (2007) 9238-9247.

[29] A. Oasmaa, S. Czernik, Fuel oil quality of biomass pyrolysis oils state of the art for the end users, Energy & Fuels 13(4) (1999) 914-921.

[30] A. Oasmaa, C. Peacocke, S. Gust, D. Meier, R. McLellan, Norms and standards for pyrolysis liquids. End-user requirements and specifications, Energy & Fuels 19(5) (2005) 2155-2163.

[31] A. Oasmaa, D.C. Elliott, J. Korhonen, Acidity of biomass fast pyrolysis bio-oils, Energy & Fuels 24(12) (2010) 6548-6554.

[32] A. Oasmaa, E. Leppämäki, P. Koponen, J. Levander, E. Tapola, Physical characterisation of biomass-based pyrolysis liquids: application of standard fuel oil analyses, VTT publications (1997).

[33] M.W. Nolte, M.W. Liberatore, Viscosity of biomass pyrolysis oils from various feedstocks, Energy & fuels 24(12) (2010) 6601-6608.

[34] S. Xiu, A. Shahbazi, Bio-oil production and upgrading research: A review, Renewable and Sustainable Energy Reviews 16(7) (2012) 4406-4414.

[35] J.P. Diebold, S. Czernik, Additives to lower and stabilize the viscosity of pyrolysis oils during storage, Energy & Fuels 11(5) (1997) 1081-1091.

[36] P. Udomsap, Y.H. Yeinn, J.T.H. Hui, B. Yoosuk, S.B. Yusuf, S. Sukkasi, Towards stabilization of bio-oil by addition of antioxidants and solvents, and emulsification with conventional hydrocarbon fuels, 2011 International Conference & Utility Exhibition on Power and Energy Systems: Issues and Prospects for Asia (ICUE), IEEE, 2011, pp. 1-5.

[37] R. Yin, L. Zhang, R. Liu, Y. Mei, W. Yu, Optimization of composite additives for improving stability of bio-oils, Fuel 170 (2016) 1-8.

[38] Y. Mei, R. Liu, L. Zhang, Influence of industrial alcohol and additive combination on the physicochemical characteristics of bio-oil from fast pyrolysis of pine sawdust in a fluidized bed reactor with hot vapor filter, Journal of the Energy Institute 90(6) (2017) 923-932.

[39] L. Zhu, K. Li, Y. Zhang, X. Zhu, Upgrading the storage properties of bio-oil by adding a compound additive, Energy & Fuels 31(6) (2017) 6221-6227.

[40] L. Zhu, K. Li, H. Ding, X. Zhu, Studying on properties of bio-oil by adding blended additive during aging, Fuel 211 (2018) 704-711.

[41] A. Oasmaa, E. Kuoppala, J.-F. Selin, S. Gust, Y. Solantausta, Fast pyrolysis of forestry residue and pine. 4. Improvement of the product quality by solvent addition, Energy & Fuels 18(5) (2004) 1578-1583.

[42] Y. Mei, M. Chai, C. Shen, B. Liu, R. Liu, Effect of methanol addition on properties and aging reaction mechanism of bio-oil during storage, Fuel 244 (2019) 499-507.

[43] H. Ding, C. Wang, X. Zhu, Estimation of the kinematic viscosities of bio-oil/alcohol blends: Kinematic viscosity-temperature formula and mixing rules, Fuel 254 (2019) 115687.

[44] H. Aubin, C. Roy, Study on the corrosiveness op wood pyrolysis oils, Petroleum Science and Technology 8(1) (1990) 77-86.

[45] H. Darmstadt, M. Garcia-Perez, A. Adnot, A. Chaala, D. Kretschmer, C. Roy, Corrosion of metals by bio-oil obtained by vacuum pyrolysis of softwood bark residues. An X-ray photoelectron spectroscopy and auger electron spectroscopy study, Energy & fuels 18(5) (2004) 1291-1301.

[46] T. Ba, A. Chaala, M. Garcia-Perez, D. Rodrigue, C. Roy, Colloidal properties of bio-oils obtained by vacuum pyrolysis of softwood bark. Characterization of water-soluble and water-insoluble fractions, Energy & Fuels 18(3) (2004) 704-712.

[47] J.R. Keiser, M. Howell, S.A. Lewis, R.M. Connatser, Corrosion studies of raw and treated biomass-derived pyrolysis oils, CORROSION 2012, NACE International, 2012.

[48] J.R. Keiser, M.A. Bestor, S. Lewis, J.M. Storey, Corrosivity of pyrolysis oils, Proceedings of the 2011 TAPPI PEERS Conference, 2011, pp. 2-5.

[49] J. Keiser, R. Connatser, Corrosion Studies of Pine-Derived Bio-oil and Heavy Fuel Oil Blends, Oak Ridge National Lab.(ORNL), Oak Ridge, TN (United States), 2020.

[50] S. Papavinasam, Electrochemical polarization techniques for corrosion monitoring, Techniques for corrosion monitoring, Elsevier2021, pp. 45-77.

[51] S. Al Saadi, Y. Yi, P. Cho, C. Jang, P. Beeley, Passivity breakdown of 316L stainless steel during potentiodynamic polarization in NaCl solution, Corrosion Science 111 (2016) 720-727.

[52] B.-Y. Chang, S.-M. Park, Electrochemical impedance spectroscopy, Annual Review of Analytical Chemistry 3 (2010) 207-229.

[53] M.E. Orazem, B. Tribollet, Electrochemical impedance spectroscopy, New Jersey 1 (2008) 383-389.

[54] T. Hong, Y. Sun, W. Jepson, Study on corrosion inhibitor in large pipelines under multiphase flow using EIS, Corrosion science 44(1) (2002) 101-112.

[55] J. Jun, M.G. Frith, R. Connatser, J. Keiser, M.P. Brady, S. Lewis Sr, Corrosion of Ferrous Alloys by Organic Compounds in Simulated Bio-Oils, Oak Ridge National Lab.(ORNL), Oak Ridge, TN (United States), 2019.

[56] J. Jun, M.G. Frith, R.M. Connatser, J.R. Keiser, M.P. Brady, S. Lewis Sr, Corrosion susceptibility of Cr–Mo steels and ferritic stainless steels in biomass-derived pyrolysis Oil constituents, Energy & Fuels 34(5) (2020) 6220-6228.

[57] X. Dupain, M. Makkee, J. Moulijn, Optimal conditions in fluid catalytic cracking: A mechanistic approach, Applied Catalysis A: General 297(2) (2006) 198-219.

[58] R. Sadeghbeigi, Fluid catalytic cracking handbook: An expert guide to the practical operation, design, and optimization of FCC units, Butterworth-Heinemann2020.

[59] Y.-M. Chen, Recent advances in FCC technology, Powder Technology 163(1-2) (2006) 2-8.

[60] R. Harding, A. Peters, J. Nee, New developments in FCC catalyst technology, Applied Catalysis A: General 221(1-2) (2001) 389-396.

[61] A.T. Jarullah, N.A. Awad, I.M. Mujtaba, Optimal design and operation of an industrial fluidized catalytic cracking reactor, Fuel 206 (2017) 657-674.

[62] A. Oloruntoba, Y. Zhang, C.S. Hsu, State-of-the-art review of fluid catalytic cracking (FCC) catalyst regeneration intensification technologies, Energies 15(6) (2022) 2061.

[63] A.V. Bridgwater, Review of fast pyrolysis of biomass and product upgrading, Biomass and bioenergy 38 (2012) 68-94.

[64] J. Adjaye, N. Bakhshi, Production of hydrocarbons by catalytic upgrading of a fast pyrolysis bio-oil. Part II: Comparative catalyst performance and reaction pathways, Fuel processing technology 45(3) (1995) 185-202.

[65] S. Vitolo, M. Seggiani, P. Frediani, G. Ambrosini, L. Politi, Catalytic upgrading of pyrolytic oils to fuel over different zeolites, Fuel 78(10) (1999) 1147-1159.

[66] S.D. Stefanidis, K.G. Kalogiannis, A.A. Lappas, Co‐processing bio‐oil in the refinery for drop‐in biofuels via fluid catalytic cracking, Wiley Interdisciplinary Reviews: Energy and Environment 7(3) (2018) e281.

[67] D. Castello, L. Rosendahl, Coprocessing of pyrolysis oil in refineries, Direct Thermochemical Liquefaction for Energy Applications, Elsevier2018, pp. 293-317.

[68] D. Chiaramonti, A. Oasmaa, Y. Solantausta, Power generation using fast pyrolysis liquids from biomass, Renewable and sustainable energy reviews 11(6) (2007) 1056-1086.

[69] S. Czernik, A. Bridgwater, Overview of applications of biomass fast pyrolysis oil, Energy & fuels 18(2) (2004) 590-598.

[70] J.D. Adjaye, S.P. Katikaneni, N.N. Bakhshi, Catalytic conversion of a biofuel to hydrocarbons: effect of mixtures of HZSM-5 and silica-alumina catalysts on product distribution, Fuel Processing Technology 48(2) (1996) 115-143.

[71] M. Talmadge, Y.J. Jiang, J. Askander, A. Singh, Strategies for Co-Processing in Refineries: Techno-Economic & Refinery Impact Analysis, National Renewable Energy Lab.(NREL), Golden, CO (United States), 2020.

[72] A.H. Bhatt, Y. Zhang, G. Heath, Bio-oil co-processing can substantially contribute to renewable fuel production potential and meet air quality standards, Applied Energy 268 (2020) 114937.

[73] S. Reham, H.H. Masjuki, M. Kalam, I. Shancita, I.R. Fattah, A. Ruhul, Study on stability, fuel properties, engine combustion, performance and emission characteristics of biofuel emulsion, Renewable and Sustainable Energy Reviews 52 (2015) 1566-1579.

[74] Q. Yin, S. Wang, X. Li, Z. Guo, Y. Gu, Review of bio-oil upgrading technologies and experimental study on emulsification of bio-oil and diesel, 2010 International Conference on Optoelectronics and Image Processing, IEEE, 2010, pp. 343-347.

[75] Z. Guo, S. Wang, X. Wang, Stability mechanism investigation of emulsion fuels from biomass pyrolysis oil and diesel, Energy 66 (2014) 250-255.

[76] D. Chiaramonti, M. Bonini, E. Fratini, G. Tondi, K. Gartner, A. Bridgwater, H. Grimm, I. Soldaini, A. Webster, P. Baglioni, Development of emulsions from biomass pyrolysis liquid and diesel and their use in engines—Part 2: tests in diesel engines, Biomass and Bioenergy 25(1) (2003) 101-111.

[77] M. Ikura, M. Stanciulescu, E. Hogan, Emulsification of pyrolysis derived bio-oil in diesel fuel, Biomass and bioenergy 24(3) (2003) 221-232.

[78] A. Lif, K. Holmberg, Water-in-diesel emulsions and related systems, Advances in colloid and interface science 123 (2006) 231-239.

[79] M. Ikura, S. Mirmiran, M. Stanciulescu, H. Sawatzky, Pyrolysis liquid-in-diesel oil microemulsions, Google Patents, 1998.

[80] L.L.L. Leng, Characterization of liquefaction bio-oil from sewage sludge and its solubilization in diesel microemulsion, Energy 82 (2015) 218-228.

[81] R. Prakash, R. Singh, S. Murugan, Use of biodiesel and bio-oil emulsions as an alternative fuel for direct injection diesel engine, Waste and Biomass Valorization 4(3) (2013) 475-484.

[82] X. Ding, X. Yuan, L. Leng, H. Huang, H. Wang, J. Shao, L. Jiang, X. Chen, G. Zeng, Upgrading sewage sludge liquefaction bio-oil by microemulsification: the effect of ethanol as polar phase on solubilization performance and fuel properties, Energy & Fuels 31(2) (2017) 1574-1582.

[83] D. Chiaramonti, M. Bonini, E. Fratini, G. Tondi, K. Gartner, A. Bridgwater, H. Grimm, I. Soldaini, A. Webster, P. Baglioni, Development of emulsions from biomass pyrolysis liquid and diesel and their use in engines—Part 1: emulsion production, Biomass and bioenergy 25(1) (2003) 85-99.

[84] Q. Lu, J. Zhang, X. Zhu, Corrosion properties of bio-oil and its emulsions with diesel, Chinese Science Bulletin 53(23) (2008) 3726-3734.

[85] A. Hoyle, Modelling the effect of Canada's clean fuel standard on greenhouse gas emissions, (2020).

[86] F.L. Stewart, S. Carrière, The Greenhouse Gas Pollution Pricing Act and The Interaction of Federal and Provincial Enforcement Efforts, SSRN Electron. J (2019).

[87] M.K. Lam, C.G. Khoo, K.T. Lee, Scale-up and commercialization of algal cultivation and biofuels production, Biofuels from algae, Elsevier2019, pp. 475-506.

[88] A. Oasmaa, J. Korhonen, E. Kuoppala, An approach for stability measurement of wood-based fast pyrolysis bio-oils, Energy & Fuels 25(7) (2011) 3307-3313.

[89] K. Cen, J. Zhang, Z. Ma, D. Chen, J. Zhou, H. Ma, Investigation of the relevance between biomass pyrolysis polygeneration and washing pretreatment under different severities: Water, dilute acid solution and aqueous phase bio-oil, Bioresource technology 278 (2019) 26-33.

[90] D. Chen, K. Cen, X. Cao, F. Chen, J. Zhang, J. Zhou, Insight into a new phenolic-leaching pretreatment on bamboo pyrolysis: Release characteristics of pyrolytic volatiles, upgradation of three phase products, migration of elements, and energy yield, Renewable and Sustainable Energy Reviews 136 (2021) 110444.

[91] A. de Rezende Pinho, M.B. de Almeida, F.L. Mendes, L.C. Casavechia, M.S. Talmadge, C.M. Kinchin, H.L. Chum, Fast pyrolysis oil from pinewood chips co-processing with vacuum gas oil in an FCC unit for second generation fuel production, Fuel 188 (2017) 462-473.

[92] F.A. Agblevor, O. Mante, R. McClung, S. Oyama, Co-processing of standard gas oil and biocrude oil to hydrocarbon fuels, Biomass and bioenergy 45 (2012) 130-137.

[93] M. Chakraborty, C. Miao, A. McDonald, S. Chen, Concomitant extraction of bio-oil and value added polysaccharides from Chlorella sorokiniana using a unique sequential hydrothermal extraction technology, Fuel 95 (2012) 63-70.

[94] N.S.T. /G31-12a, Standard Guide for Laboratory Immersion Corrosion Testing of Metals, (2012).

[95] Z. Ma, Q. Sun, J. Ye, Q. Yao, C. Zhao, Study on the thermal degradation behaviors and kinetics of alkali lignin for production of phenolic-rich bio-oil using TGA–FTIR and Py–GC/MS, Journal of Analytical and Applied Pyrolysis 117 (2016) 116-124.

[96] V. Pasangulapati, K.D. Ramachandriya, A. Kumar, M.R. Wilkins, C.L. Jones, R.L. Huhnke, Effects of cellulose, hemicellulose and lignin on thermochemical conversion characteristics of the selected biomass, Bioresource technology 114 (2012) 663-669.

[97] Y. Ma, H. Zhang, H. Yang, Y. Zhang, The effect of acid washing pretreatment on bio-oil production in fast pyrolysis of rice husk, Cellulose 26(15) (2019) 8465-8474.

[98] R.N. Hilten, K. Das, Comparison of three accelerated aging procedures to assess bio-oil stability, Fuel 89(10) (2010) 2741-2749.

[99] K.H. Kim, T.J. Daugaard, R. Smith, M. Mba-Wright, R.C. Brown, Recovery of resin acids from fast pyrolysis of pine, Journal of Analytical and Applied Pyrolysis 138 (2019) 132-136.

[100] D. Chen, J. Zhou, Q. Zhang, X. Zhu, Evaluation methods and research progresses in bio-oil storage stability, Renewable and Sustainable Energy Reviews 40 (2014) 69-79.

[101] Q. Lu, X.-l. Yang, X.-f. Zhu, Analysis on chemical and physical properties of bio-oil pyrolyzed from rice husk, Journal of Analytical and Applied Pyrolysis 82(2) (2008) 191-198.

[102] B. Pidtasang, P. Udomsap, S. Sukkasi, N. Chollacoop, A. Pattiya, Influence of alcohol addition on properties of bio-oil produced from fast pyrolysis of eucalyptus bark in a free-fall reactor, Journal of Industrial and Engineering Chemistry 19(6) (2013) 1851-1857.

[103] J. Diebold, A review of the chemical and physical mechanisms of the storage stability of fast pyrolysis bio-oils. 2000, Thermalchemie, Inc. Lakewood, Colorado National Renewable Energy Laboratory http://www. doe. gov/bridge.

[104] Q. Lu, W.-Z. Li, X.-F. Zhu, Overview of fuel properties of biomass fast pyrolysis oils, Energy conversion and management 50(5) (2009) 1376-1383.

[105] R. Sadeghbeigi, Process and mechanical design guidelines for FCC equipment, Fluid Catalytic Cracking Handbook (2020) 223-240.

[106] R. Sadeghbeigi, Chapter 1—Process Description, Fluid Catalytic Cracking Handbook, 2nd ed.; Sadeghbeigi, R., Ed (2012) 1-39.

[107] M. Brady, J. Keiser, D. Leonard, A. Zacher, K. Bryden, G. Weatherbee, Corrosion of stainless steels in the riser during co-processing of bio-oils in a fluid catalytic cracking pilot plant, Fuel Processing Technology 159 (2017) 187-199.

[108] A.A. Frutos, L.F. Sala, G.M. Escandar, J.M.S. Peregrin, M.G. Sierra, Complex formation between D-lactobionate and bivalent metal ions. Studies in solution and in the solid state, Canadian journal of chemistry 75(4) (1997) 405-413.

[109] R.A. Antunes, M.C.L. de Oliveira, Corrosion in biomass combustion: A materials selection analysis and its interaction with corrosion mechanisms and mitigation strategies, Corrosion Science 76 (2013) 6-26.

[110] D. Mercier, M.-G. Barthés-Labrousse, The role of chelating agents on the corrosion mechanisms of aluminium in alkaline aqueous solutions, Corrosion Science 51(2) (2009) 339-348.

[111] D. Mercier, J.-C. Rouchaud, M.-G. Barthés-Labrousse, Interaction of amines with native aluminium oxide layers in non-aqueous environment: Application to the understanding of the formation of epoxy-amine/metal interphases, Applied Surface Science 254(20) (2008) 6495-6503.

[112] R.M. Connatser, M.G. Frith, J. Jun, S.A. Lewis Sr, M.P. Brady, J.R. Keiser, Approaches to investigate the role of chelation in the corrosivity of biomass-derived oils, Biomass and Bioenergy 133 (2020) 105446.

[113] I.M.T. Usman, Y.-C. Ho, L. Baloo, M.-K. Lam, W. Sujarwo, A comprehensive review on the advances of bioproducts from biomass towards meeting net zero carbon emissions (NZCE), Bioresource Technology (2022) 128167.

[114] É. Yáñez, H. Meerman, A. Ramírez, É. Castillo, A. Faaij, Assessing bio‐oil co‐processing routes as CO2 mitigation strategies in oil refineries, Biofuels, Bioproducts and Biorefining 15(1) (2021) 305-333.

[115] P. Adams, T. Bridgwater, A. Lea-Langton, A. Ross, I. Watson, Biomass conversion technologies, Greenhouse gas balances of bioenergy systems, Elsevier2018, pp. 107-139.

[116] X. Chen, Q. Che, S. Li, Z. Liu, H. Yang, Y. Chen, X. Wang, J. Shao, H. Chen, Recent developments in lignocellulosic biomass catalytic fast pyrolysis: Strategies for the optimization of bio-oil quality and yield, Fuel Processing Technology 196 (2019) 106180.

[117] J. Akhtar, N.A.S. Amin, A review on process conditions for optimum bio-oil yield in hydrothermal liquefaction of biomass, Renewable and Sustainable Energy Reviews 15(3) (2011) 1615-1624.

[118] L. Wu, Y. Yang, T. Yan, Y. Wang, L. Zheng, K. Qian, F. Hong, Sustainable design and optimization of co-processing of bio-oil and vacuum gas oil in an existing refinery, Renewable and Sustainable Energy Reviews 130 (2020) 109952.

[119] A. de Rezende Pinho, M.B. De Almeida, F.L. Mendes, V.L. Ximenes, L.C. Casavechia, Co-processing raw bio-oil and gasoil in an FCC Unit, Fuel Processing Technology 131 (2015) 159-166.

[120] X. Han, H. Wang, Y. Zeng, J. Liu, Advancing the application of bio-oils by co-processing with petroleum intermediates: a review, Energy Conversion and Management: X 10 (2021) 100069.

[121] H. Wang, A. Gross, J. Liu, Influence of methanol addition on bio-oil thermal stability and corrosivity, Chemical Engineering Journal 433 (2022) 133692.

[122] R. Holland, Corrosion testing by potentiodynamic polarization in various electrolytes, Dental Materials 8(4) (1992) 241-245.

[123] S. Wang, J. Zhang, O. Gharbi, V. Vivier, M. Gao, M.E. Orazem, Electrochemical impedance spectroscopy, Nature Reviews Methods Primers 1(1) (2021) 41.

[124] J. Jun, D. Sulejmanovic, J.R. Keiser, M.P. Brady, M.D. Kass, Evaluation of Corrosion Susceptibility of Structural Steels in Biomass Derived Pyrolysis Oil, CORROSION 2021, OnePetro, 2021.

[125] J. Jun, D. Sulejmanovic, J.R. Keiser, M.P. Brady, M.D. Kass, Electrochemical Corrosion Analysis of Stainless Steels in LALM Pyrolysis Bio-Oil with Organic Corrodents, AMPP CORROSION, AMPP, 2022, p. D021S017R004.

[126] J. Jun, D. Sulejmanovic, J.R. Keiser, M.P. Brady, M.D. Kass, Corrosion Behavior of Alloy Structural Steels in Catechol and Biomass-Derived Pyrolysis Oils, NACE CORROSION, NACE, 2021, p. D121S053R001.

[127] J.R. Keiser, G.L. Warrington, S.A. Lewis Sr, R.M. Connatser, J. Jun, J. Qu, K. Lee, M.P. Brady, Corrosion and Chemical Characterization of Bio-Oils from Biomass with Varying Ash and Moisture Contents, NACE CORROSION, NACE, 2021, p. D121S053R007.

[128] H. Wang, J. Liu, Emulsification and corrosivity study of bio-oil and vacuum gas oil mixtures with a novel surfactant system, Fuel 333 (2023) 126460.

[129] J. Jun, D. Sulejmanovic, J.R. Keiser, M.P. Brady, M.D. Kass, Electrochemical Corrosion Analysis of Stainless Steels in LALM Pyrolysis Bio-Oil with Organic Corrodents, AMPP Annual Conference+ Expo, OnePetro, 2022.

[130] J. Jun, D. Sulejmanovic, J.R. Keiser, M.P. Brady, M.D. Kass, Corrosion Behavior of Alloy Structural Steels in Catechol and Biomass-Derived Pyrolysis Oils, CORROSION 2021, OnePetro, 2021.

[131] A. Ahmad, F. Hussain, K. Deen, R. Ahmad, L. Ali, M. Kamran, M. Azam, Corrosion behavior of X-70 pipe steel in crude oil environments depending upon surface characteristics, Arabian Journal for Science and Engineering 39 (2014) 5393-5404.

[132] H.H. Hernández, A.M.R. Reynoso, J.C.T. González, C.O.G. Morán, J.G.M. Hernández, A.M. Ruiz, J.M. Hernández, R.O. Cruz, Electrochemical impedance spectroscopy (EIS): A review study of basic aspects of the corrosion mechanism applied to steels, Electrochemical Impedance Spectroscopy (2020) 137-144.

[133] X. Liu, J. Xiong, Y. Lv, Y. Zuo, Study on corrosion electrochemical behavior of several different coating systems by EIS, Progress in Organic Coatings 64(4) (2009) 497-503.

[134] L. Gao, S. Peng, Z. Gong, J. Chen, A combination of experiment and theoretical methods to study the novel and low-cost corrosion inhibitor 1-hydroxy-7-azabenzotriazole for mild steel in 1 M sulfuric acid, RSC advances 8(67) (2018) 38506-38516.

[135] S.E. Lemallem, A. Fiala, H.B. Ladouani, H. Allal, Corrosion inhibition performance of two ketene dithioacetal derivatives for stainless steel in hydrochloric acid solution, Journal of Electrochemical Science and Technology 13(2) (2021) 237-253.

[136] J. Calderón, F. Vásquez, J. Carreño, Adsorption and performance of the 2-mercaptobenzimidazole as a carbon steel corrosion inhibitor in EDTA solutions, Materials Chemistry and Physics 185 (2017) 218-226.

[137] B.E. Brycki, I.H. Kowalczyk, A. Szulc, O. Kaczerewska, M. Pakiet, Organic corrosion inhibitors, Corrosion inhibitors, principles and recent applications 3 (2018) 33.

[138] B. Nahak, S. Preetam, D. Sharma, S. Shukla, M. Syväjärvi, D.-C. Toncu, A. Tiwari, Advancements in net-zero pertinency of lignocellulosic biomass for climate neutral energy production, Renewable and Sustainable Energy Reviews 161 (2022) 112393.

[139] O.C. Anika, S.G. Nnabuife, A. Bello, E.R. Okoroafor, B. Kuang, R. Villa, Prospects of low and zero-carbon renewable fuels in 1.5-degree net zero emission actualisation by 2050: A critical review, Carbon Capture Science & Technology 5 (2022) 100072.

[140] Z. Abideen, A. Hameed, H.-W. Koyro, B. Gul, R. Ansari, M.A. Khan, Sustainable biofuel production from non-food sources-An overview, Emirates Journal of Food and Agriculture (2014) 1057-1066.

[141] L. Wu, Y. Wang, L. Zheng, M. Shi, J. Li, Design and optimization of bio-oil co-processing with vacuum gas oil in a refinery, Energy Conversion and Management 195 (2019) 620-629.

[142] L. Wu, Y. Wang, L. Zheng, P. Wang, X. Han, Techno-economic analysis of bio-oil co-processing with vacuum gas oil to transportation fuels in an existing fluid catalytic cracker, Energy Conversion and Management 197 (2019) 111901.

[143] A.A. Ali, M.A. Mustafa, K.E. Yassin, A techno-economic evaluation of bio-oil co-processing within a petroleum refinery, Biofuels (2018).

[144] J.R. Keiser, M.P. Brady, J. Jun, D. Sulejmanovic, M.D. Kass, Performance of Structural Alloys in Bio-oil Production, Upgrading, and Storage Systems, Energy & Fuels 37(2) (2023) 1104-1115.

[145] H. Pedraza, H. Wang, X. Han, Y. Zeng, J. Liu, Corrosion and aging risk assessment of an injection system for FCC/Bio-oil co-feed, Biomass and Bioenergy 175 (2023) 106875.

[146] W. Cai, N. Kang, M.K. Jang, C. Sun, R. Liu, Z. Luo, Long term storage stability of bio-oil from rice husk fast pyrolysis, Energy 186 (2019) 115882.

[147] Z. Yang, A. Kumar, R.L. Huhnke, Review of recent developments to improve storage and transportation stability of bio-oil, Renewable and Sustainable Energy Reviews 50 (2015) 859-870.

[148] J. Jun, D. Sulejmanovic, J.R. Keiser, M.P. Brady, M.D. Kass, Evaluation of Corrosion Susceptibility of Structural Steels in Biomass Derived Pyrolysis Oil, NACE CORROSION, NACE, 2021, p. D121S053R002.

[149] J. Jun, Y.-F. Su, J.R. Keiser, J.E. Wade IV, M.D. Kass, J.R. Ferrell III, E. Christensen, M.V. Olarte, D. Sulejmanovic, Corrosion Compatibility of Stainless Steels and Nickel in Pyrolysis Biomass-Derived Oil at Elevated Storage Temperatures, Sustainability 15(1) (2022) 22.

[150] M. Garcia-Perez, A. Chaala, H. Pakdel, D. Kretschmer, D. Rodrigue, C. Roy, Evaluation of the influence of stainless steel and copper on the aging process of bio-oil, Energy & fuels 20(2) (2006) 786-795.

[151] H. Wang, A. Gross, J. Liu, Influence of methanol addition on bio-oil thermal stability and corrosivity, Chemical Engineering Journal (2021) 133692.

[152] H. Wang, J. Liu, Electrochemical corrosion study of carbon steel in bio-oil environments, Renewable Energy 221 (2024) 119823.

[153] W.P. Miller, L.W. Zelazny, D. Martens, Dissolution of synthetic crystalline and noncrystalline iron oxides by organic acids, Geoderma 37(1) (1986) 1-13.

[154] D. Panias, M. Taxiarchou, I. Paspaliaris, A. Kontopoulos, Mechanisms of dissolution of iron oxides in aqueous oxalic acid solutions, Hydrometallurgy 42(2) (1996) 257-265.

[155] J. Cai, M.M. Rahman, S. Zhang, M. Sarker, X. Zhang, Y. Zhang, X. Yu, E.H. Fini, Review on aging of bio-oil from biomass pyrolysis and strategy to slowing aging, Energy & Fuels 35(15) (2021) 11665-11692.

[156] J. Meng, A. Moore, D. Tilotta, S. Kelley, S. Park, Toward understanding of bio-oil aging: accelerated aging of bio-oil fractions, ACS Sustainable Chemistry & Engineering 2(8) (2014) 2011-2018.

[157] R. Hell, U.W. Stephan, Iron uptake, trafficking and homeostasis in plants, Planta 216 (2003) 541-551.

[158] J. Jeong, A. Merkovich, M. Clyne, E.L. Connolly, Directing iron transport in dicots: regulation of iron acquisition and translocation, Current opinion in plant biology 39 (2017) 106-113.

[159] G.W. Huber, A. Corma, Synergies between bio‐ and oil refineries for the production of fuels from biomass, Angewandte Chemie International Edition 46(38) (2007) 7184-7201.

[160] J.A. Melero, J. Iglesias, A. Garcia, Biomass as renewable feedstock in standard refinery units. Feasibility, opportunities and challenges, Energy & environmental science 5(6) (2012) 7393-7420.

[161] M.S. Talmadge, R.M. Baldwin, M.J. Biddy, R.L. McCormick, G.T. Beckham, G.A. Ferguson, S. Czernik, K.A. Magrini-Bair, T.D. Foust, P.D. Metelski, A perspective on oxygenated species in the refinery integration of pyrolysis oil, Green Chemistry 16(2) (2014) 407-453.

[162] A. Eschenbacher, T. Myrstad, N. Bech, J.Ø. Duus, C. Li, P.A. Jensen, U.B. Henriksen, J. Ahrenfeldt, U.V. Mentzel, A.D. Jensen, Co-processing of wood and wheat straw derived pyrolysis oils with FCC feed—Product distribution and effect of deoxygenation, Fuel 260 (2020) 116312.

[163] C. Wang, R. Venderbosch, Y. Fang, Co-processing of crude and hydrotreated pyrolysis liquids and VGO in a pilot scale FCC riser setup, Fuel Processing Technology 181 (2018) 157-165.

[164] S. van Dyk, J. Su, J.D. Mcmillan, J. Saddler, Potential synergies of drop‐in biofuel production with further co‐processing at oil refineries, Biofuels, Bioproducts and Biorefining 13(3) (2019) 760-775.

[165] G. Fogassy, N. Thegarid, Y. Schuurman, C. Mirodatos, From biomass to bio-gasoline by FCC co-processing: effect of feed composition and catalyst structure on product quality, Energy & Environmental Science 4(12) (2011) 5068-5076.

[166] T.N. Pham, T. Sooknoi, S.P. Crossley, D.E. Resasco, Ketonization of carboxylic acids: mechanisms, catalysts, and implications for biomass conversion, Acs Catalysis 3(11) (2013) 2456-2473.

[167] M. Gliński, J. Kijeński, A. Jakubowski, Ketones from monocarboxylic acids: Catalytic ketonization over oxide systems, Applied Catalysis A: General 128(2) (1995) 209-217.

[168] A. Grosvenor, B. Kobe, M.C. Biesinger, N. McIntyre, Investigation of multiplet splitting of Fe 2p XPS spectra and bonding in iron compounds, Surface and Interface Analysis: An International Journal devoted to the development and application of techniques for the analysis of surfaces, interfaces and thin films 36(12) (2004) 1564-1574.

[169] P.M. Hallam, M. Gómez-Mingot, D.K. Kampouris, C.E. Banks, Facile synthetic fabrication of iron oxide particles and novel hydrogen superoxide supercapacitors, Rsc Advances 2(16) (2012) 6672-6679.

[170] A. Lappas, S. Bezergianni, I. Vasalos, Production of biofuels via co-processing in conventional refining processes, Catalysis Today 145(1-2) (2009) 55-62.

[171] G. Fogassy, N. Thegarid, G. Toussaint, A.C. van Veen, Y. Schuurman, C. Mirodatos, Biomass derived feedstock co-processing with vacuum gas oil for second-generation fuel production in FCC units, Applied Catalysis B: Environmental 96(3-4) (2010) 476-485.

[172] F. de Miguel Mercader, M. Groeneveld, S. Kersten, N. Way, C. Schaverien, J. Hogendoorn, Production of advanced biofuels: Co-processing of upgraded pyrolysis oil in standard refinery units, Applied Catalysis B: Environmental 96(1-2) (2010) 57-66.

[173] A. Dimitriadis, D. Liakos, U. Pfisterer, M. Moustaka-Gouni, D. Karonis, S. Bezergianni, Impact of hydrogenation on miscibility of fast pyrolysis bio-oil with refinery fractions towards bio-oil refinery integration, Biomass and Bioenergy 151 (2021) 106171.

[174] M. Bertero, U. Sedran, Coprocessing of bio-oil in fluid catalytic cracking, Recent advances in thermo-chemical conversion of biomass, Elsevier2015, pp. 355-381.

[175] N. Sharma, K.K. Jaiswal, V. Kumar, M.S. Vlaskin, M. Nanda, I. Rautela, M.S. Tomar, W. Ahmad, Effect of catalyst and temperature on the quality and productivity of HTL bio-oil from microalgae: A review, Renewable Energy 174 (2021) 810-822.

[176] R. Ghadge, N. Nagwani, N. Saxena, S. Dasgupta, A. Sapre, Design and scale-up challenges in hydrothermal liquefaction process for biocrude production and its upgradation, Energy Conversion and Management: X (2022) 100223.

[177] A. Farooq, H. Shafaghat, J. Jae, S.-C. Jung, Y.-K. Park, Enhanced stability of bio-oil and diesel fuel emulsion using Span 80 and Tween 60 emulsifiers, Journal of environmental management 231 (2019) 694-700.

[178] M.D.G. de Luna, L.A.D. Cruz, W.-H. Chen, B.-J. Lin, T.-H. Hsieh, Improving the stability of diesel emulsions with high pyrolysis bio-oil content by alcohol co-surfactants and high shear mixing strategies, Energy 141 (2017) 1416-1428.

[179] R. Kumar, V. Strezov, Thermochemical production of bio-oil: A review of downstream processing technologies for bio-oil upgrading, production of hydrogen and high value-added products, Renewable and Sustainable Energy Reviews 135 (2021) 110152.

[180] J.A. Martin, C.A. Mullen, A.A. Boateng, Maximizing the stability of pyrolysis oil/diesel fuel emulsions, Energy & fuels 28(9) (2014) 5918-5929.

[181] B.-J. Lin, W.-H. Chen, W.M. Budzianowski, C.-T. Hsieh, P.-H. Lin, Emulsification analysis of bio-oil and diesel under various combinations of emulsifiers, Applied energy 178 (2016) 746-757.

[182] M.G. Kassem, A.-M.M. Ahmed, H.H. Abdel-Rahman, A.H. Moustafa, Use of Span 80 and Tween 80 for blending gasoline and alcohol in spark ignition engines, Energy Reports 5 (2019) 221-230.

[183] A. Cid, Synthesis of NPs by microemulsion method, Microemulsion-a Chemical Nanoreactor, IntechOpen2018.

[184] Y. Dini, M. Becerra, J.M. Shaw, Phase behavior and thermophysical properties of Peace River bitumen+ propane mixtures from 303 K to 393 K, Journal of Chemical & Engineering Data 61(8) (2016) 2659-2668.

[185] H. Wang, J.M. Shaw, Z. Jin, Discontinuous Displacement at Solvent–Immobile Hydrocarbon Interfaces, Energy & Fuels 34(8) (2020) 9392-9400.

Appendix

Appendix A. Bio-oil (BO) Phase Separation Experiments
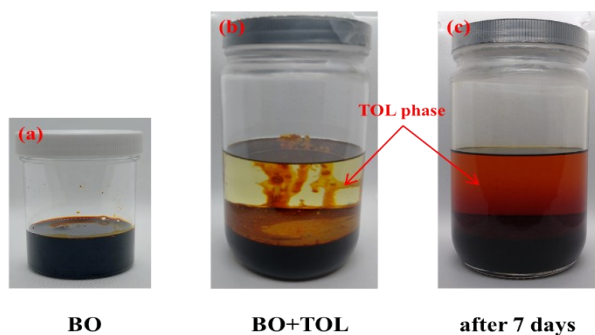
Fig. A1. Bio-oil (BO) separation experiments by toluene (TOL): (a) BO; (b) BO+TOL (just made); and (c) BO+TOL (after 7 days).
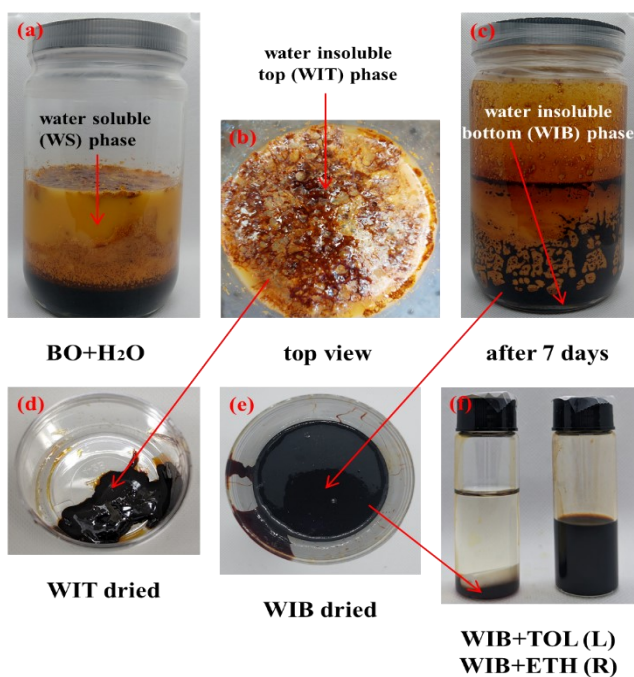
Fig. A2. BO separation experiments by water (H_2O): (a) BO+H_2O (just made); (b) BO+H_2O top view; (c) BO+H_2O (after 7 days); (d) water-insoluble top (WIT) phase dried; (e) water-insoluble bottom (WIB) phase dried; and (f) WIB+TOL (left) and WIB+ethanol (ETH) (right).
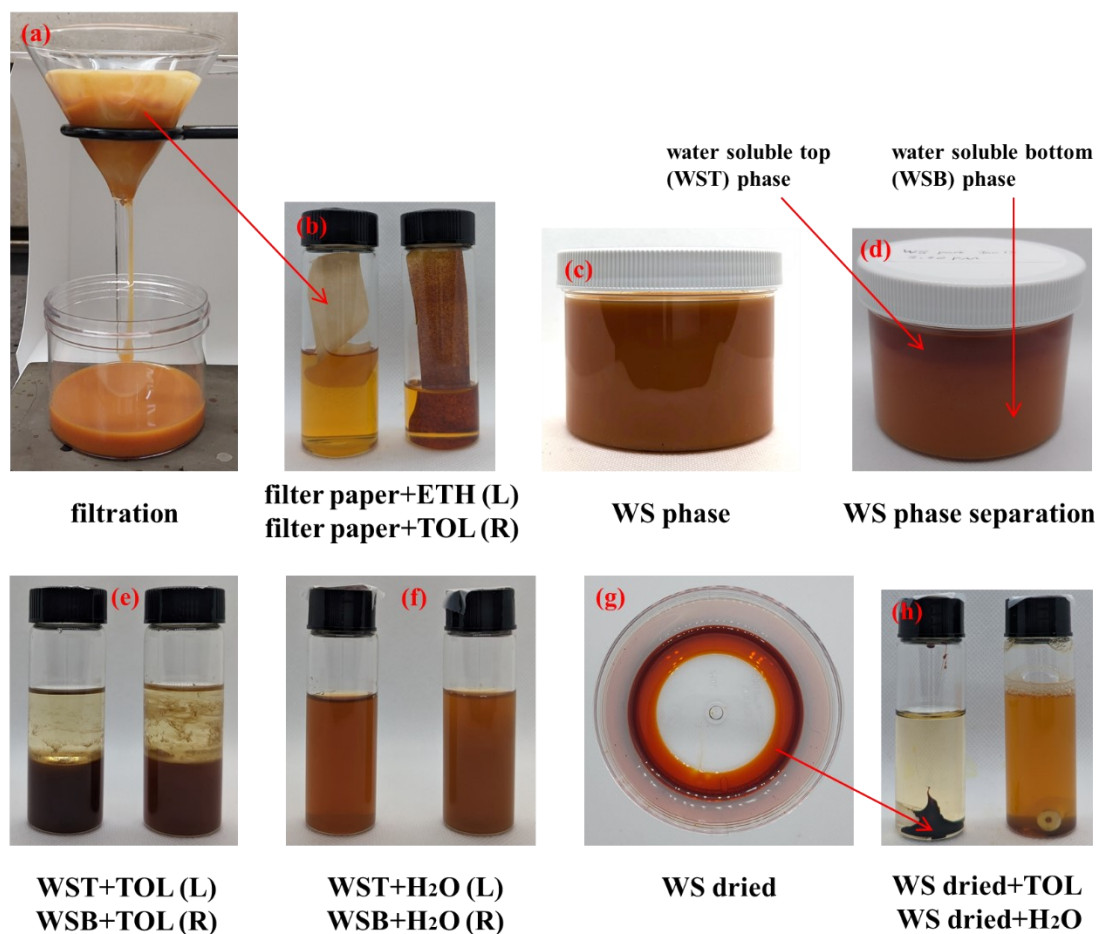
Fig. A3. Water soluble (WS) phase characterization: (a) WS filtration; (b) filter paper+ETH (left) and filter paper+TOL (right); (c) WS phase; (d) WS phase-separated into water-soluble top (WST) phase and water-soluble bottom (WSB); (e) WST+TOL (left) and WSB+TOL (right); (f) WST+H$_2$O (left) and WSB+H$_2$O (right); (g) WS dried; and (h) WS dried+TOL and WS dried+H$_2$O.
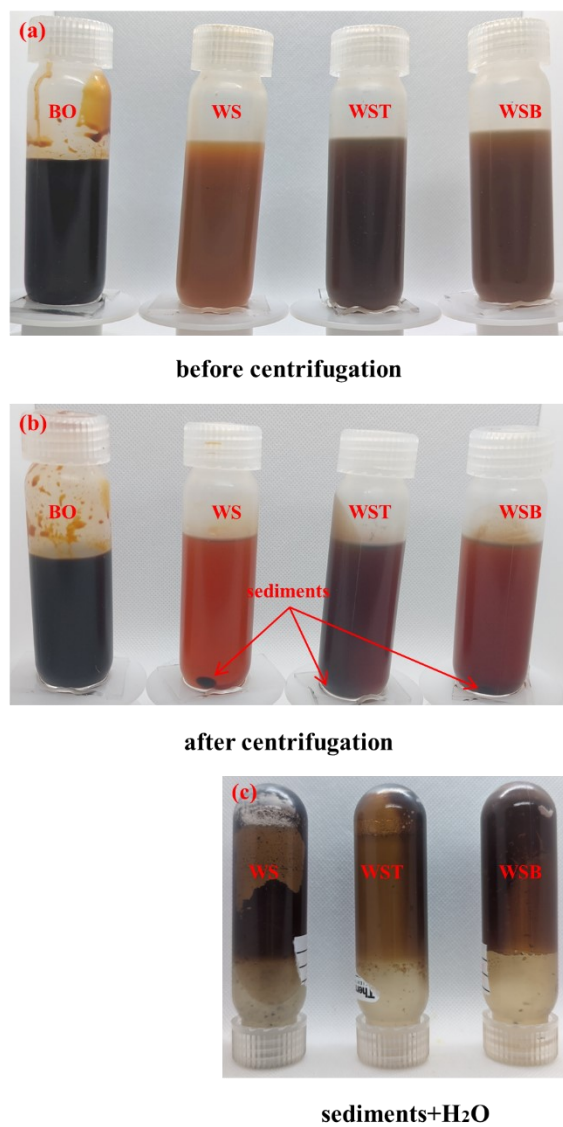
Fig. A4. Centrifugation for BO, WS, WST, and WSB phases: (a) before centrifugation; (b) after centrifugation; and (c) WS sediment+H_2O (left), WST sediment+H_2O (middle), and WSB sediment+H_2O (right).
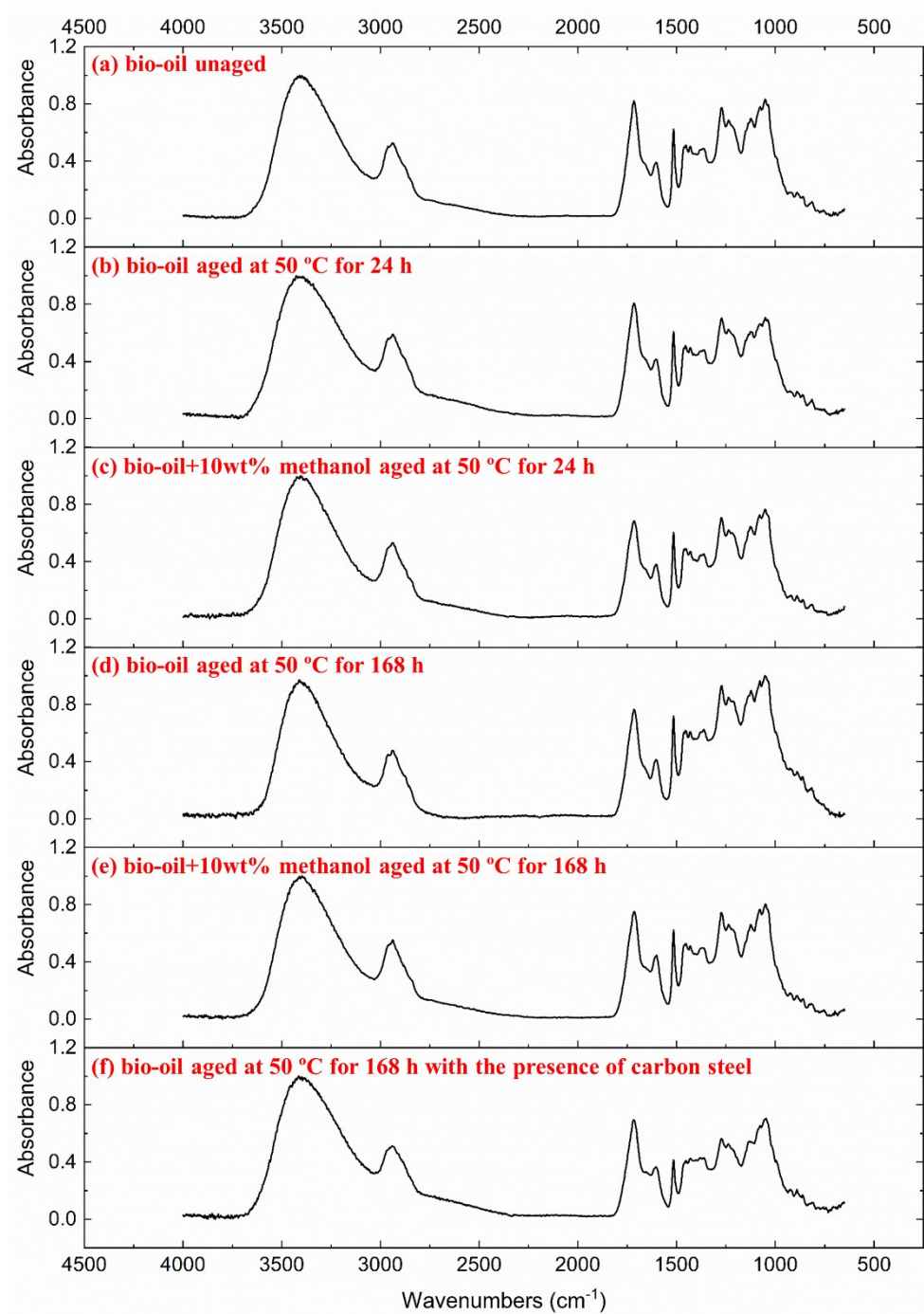
Fig. A5. FT-IR spectra of BO samples before and after aging and immersion experiments.

Table A1. FT-IR data for BO.

Wave # (cm⁻¹)	Absorbance	Wave # (cm⁻¹)	Absorbance	Wave # (cm⁻¹)	Absorbance	Wave # (cm⁻¹)	Absorbance
650	0.039	1498	0.179	2366	0.009	3215	0.431
669	0.021	1518	0.435	2386	0.008	3234	0.474
688	0.009	1537	0.062	2405	0.012	3253	0.507
708	0.012	1556	0.060	2424	0.015	3273	0.552
727	0.005	1576	0.113	2443	0.020	3292	0.587
746	0.021	1595	0.256	2463	0.023	3311	0.625
766	0.022	1614	0.268	2482	0.028	3331	0.664
785	0.032	1633	0.219	2501	0.032	3350	0.687
804	0.050	1653	0.261	2521	0.035	3369	0.721
823	0.068	1672	0.292	2540	0.041	3388	0.727
843	0.054	1691	0.398	2559	0.045	3408	0.743
862	0.104	1711	0.592	2578	0.048	3427	0.732
881	0.114	1730	0.512	2598	0.053	3446	0.703
901	0.104	1749	0.347	2617	0.057	3466	0.661
920	0.126	1768	0.188	2636	0.060	3485	0.603
939	0.119	1788	0.079	2656	0.064	3504	0.514
958	0.165	1807	0.019	2675	0.065	3523	0.430
978	0.239	1826	0.003	2694	0.070	3543	0.339
997	0.316	1846	0.001	2713	0.076	3562	0.241
1016	0.413	1865	0.003	2733	0.080	3581	0.170
1036	0.590	1884	0.002	2752	0.085	3601	0.112
1055	0.613	1903	0.002	2771	0.087	3620	0.073
1074	0.577	1923	0.001	2791	0.095	3639	0.045
1093	0.529	1942	0.001	2810	0.109	3658	0.020
1113	0.495	1961	0.002	2829	0.143	3678	0.007
1132	0.497	1981	0.001	2848	0.195	3697	-0.001
1151	0.448	2000	0.001	2868	0.243	3716	-0.003
1171	0.338	2019	0.002	2887	0.275	3735	-0.010
1190	0.386	2038	0.002	2906	0.315	3755	-0.007
1209	0.466	2058	0.005	2926	0.367	3774	-0.007
1228	0.489	2077	0.002	2945	0.381	3793	-0.005
1248	0.477	2096	0.001	2964	0.364	3813	-0.006
1267	0.560	2116	0.002	2983	0.296	3832	-0.010
1286	0.474	2135	0.002	3003	0.227	3851	-0.001
1306	0.320	2154	0.000	3022	0.204	3870	-0.005
1325	0.286	2173	0.000	3041	0.203	3890	-0.002
1344	0.295	2193	-0.002	3061	0.213	3909	-0.002
1363	0.360	2212	-0.001	3080	0.222	3928	-0.002
1383	0.349	2231	-0.001	3099	0.243	3948	0.000
1402	0.329	2251	-0.001	3118	0.268	3967	-0.001
1421	0.339	2270	0.000	3138	0.290	3986	0.006
1441	0.342	2289	0.003	3157	0.320	3697	-0.001
1460	0.366	2308	0.001	3176	0.358	3716	-0.003

Table A2. Changes in viscosity, density, water content, and pH value of BO and BO/methanol

(ME) mixtures after aging at 50 ºC.

ME (wt%)	Aging time (h)	Viscosity (cP)	Density (g/mL)	Water content (wt%)	pH value
0	0	171.5	1.2004	24.7	2.83
	24	173.5	1.2073	24.6	2.86
	96	198.0	1.2156	23.9	2.74
	168	227.5	1.2168	24.1	2.80
5	0	79.5	1.1815	24.0	3.00
	24	90.0	1.1881	23.6	3.04
	96	93.3	1.1925	23.2	2.94
	168	136.3	1.1990	23.6	3.02
10	0	48.5	1.1597	23.1	3.13
	24	51.5	1.1655	22.8	3.24
	96	51.3	1.1688	22.3	3.14
	168	60.3	1.1696	23.0	3.22
15	0	28.8	1.1363	21.8	3.27
	24	32.6	1.1403	21.7	3.42
	96	29.8	1.1431	21.3	3.38
	168	35.6	1.1454	22.3	3.40
20	0	20.0	1.1131	20.3	3.42
	24	22.8	1.1164	20.3	3.57
	96	20.6	1.1219	20.1	3.56
	168	26.0	1.1282	21.5	3.56

Table A3. Changes in viscosity, density, water content, and pH value of BO and BO/ME

mixtures after aging at 80 ºC.

ME (wt%)	Aging time (h)	Viscosity (cP)	Density (g/mL)	Water content (wt%)	pH value
0	0	171.5	1.2004	24.7	2.83
	24	310.0	1.2151	23.3	3.02
	96	1855.0	1.2395	22.0	3.13
	168	2125.0	1.2437	22.3	3.09
5	0	79.5	1.1815	24.0	3.00
	24	166.0	1.1937	22.6	3.19
	96	610.0	1.2225	21.0	3.30
	168	770.0	1.2278	21.0	3.25
10	0	48.5	1.1597	23.1	3.13
	24	77.5	1.1730	21.4	3.42
	96	290.0	1.1989	19.5	3.53
	168	530.0	1.2082	20.0	3.50
15	0	28.8	1.1363	21.8	3.27
	24	53.2	1.1508	20.0	3.64
	96	105.3	1.1787	17.7	3.69
	168	219.0	1.1845	19.0	3.65
20	0	20.0	1.1131	20.3	3.42
	24	46.6	1.1292	18.4	3.79
	96	66.0	1.1564	16.1	3.90
	168	98.0	1.1649	18.0	3.80

Appendix B. Immersion Experiments
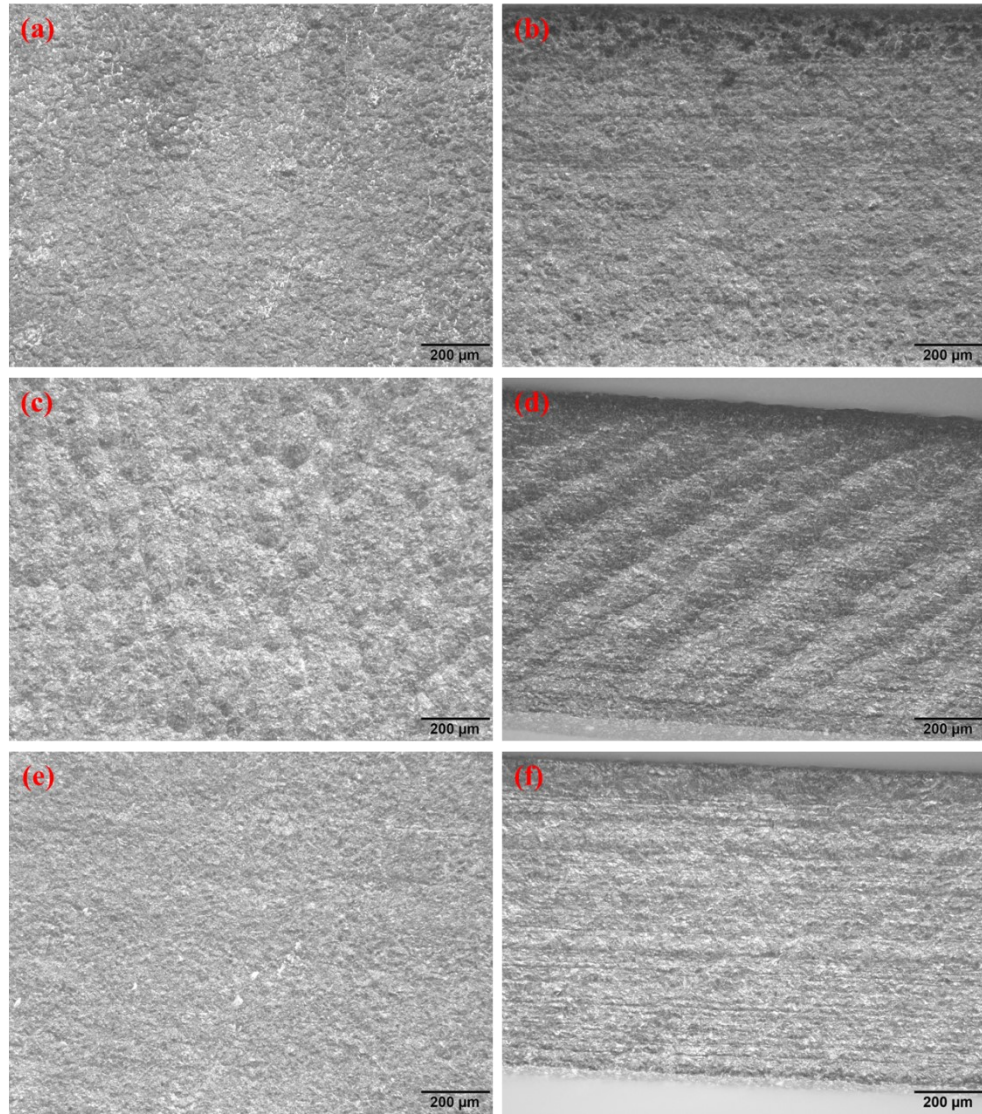
Fig. B1. Optical micrographs of carbon steel (CS) specimens after immersion experiments at 50 °C for 24h: (a) front image in BO; (b) cross-sectional image in BO; (c) front image in BO+10wt% ME; (d) cross-sectional image in BO+10wt% ME; (e) front image in BO+20wt% ME; (f) cross-sectional image in BO+20wt% ME.
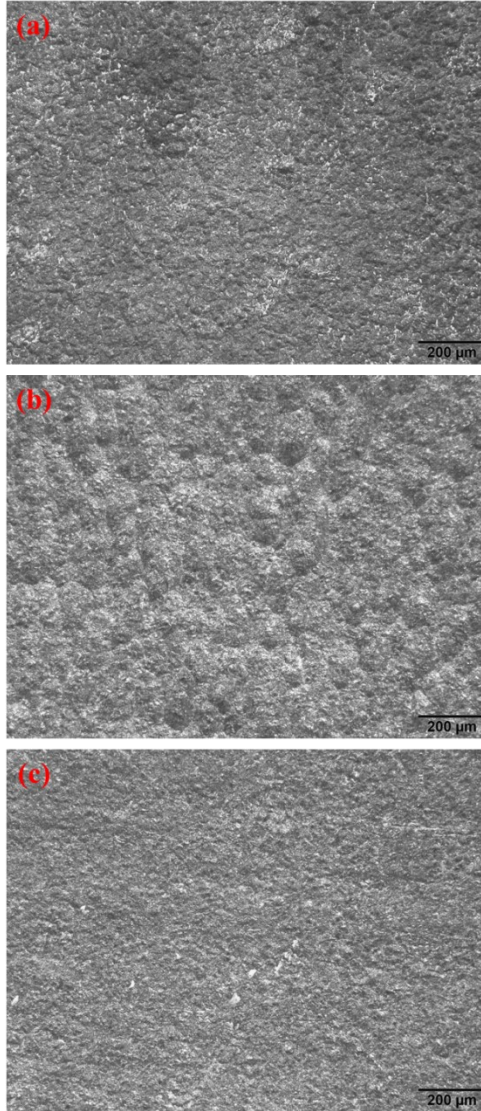
Fig. B2. Optical micrographs of CS specimens after immersion experiments at 80 °C for 24h: (a) in BO; (b) in BO+10wt% ME; (c) in BO+20wt% ME.
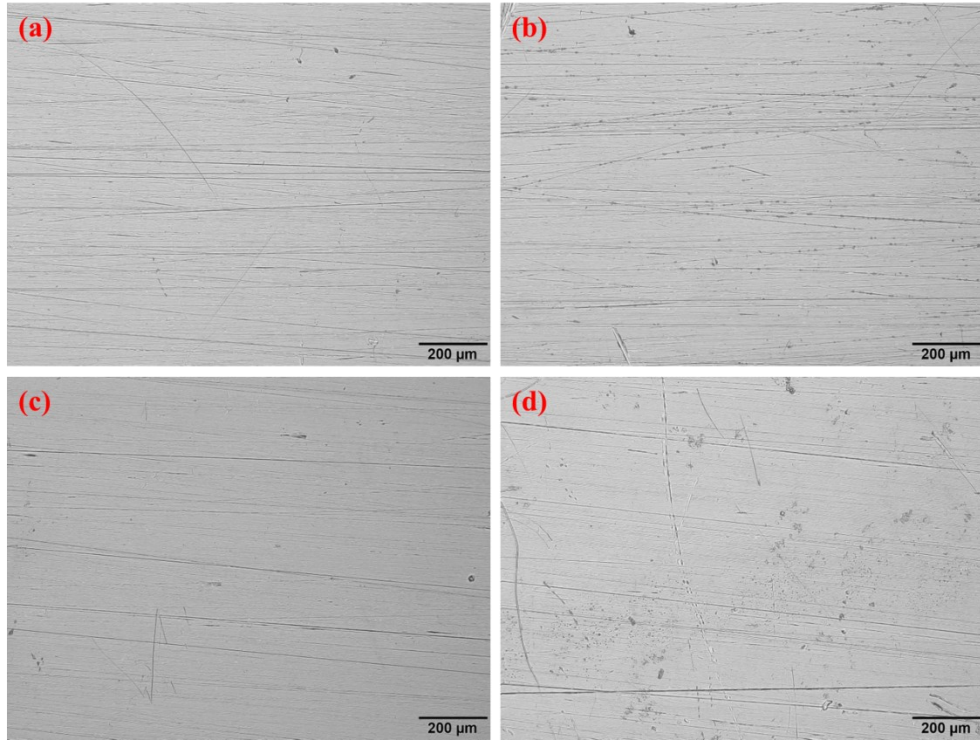
Fig. B3. Optical micrographs of stainless steel (SS) specimens after 24h immersion experiments in BO: (a) SS 304L at 50 °C (a) SS 304L at 80 °C; (b) SS 316L at 50 °C; (c) SS 316L at 80 °C.
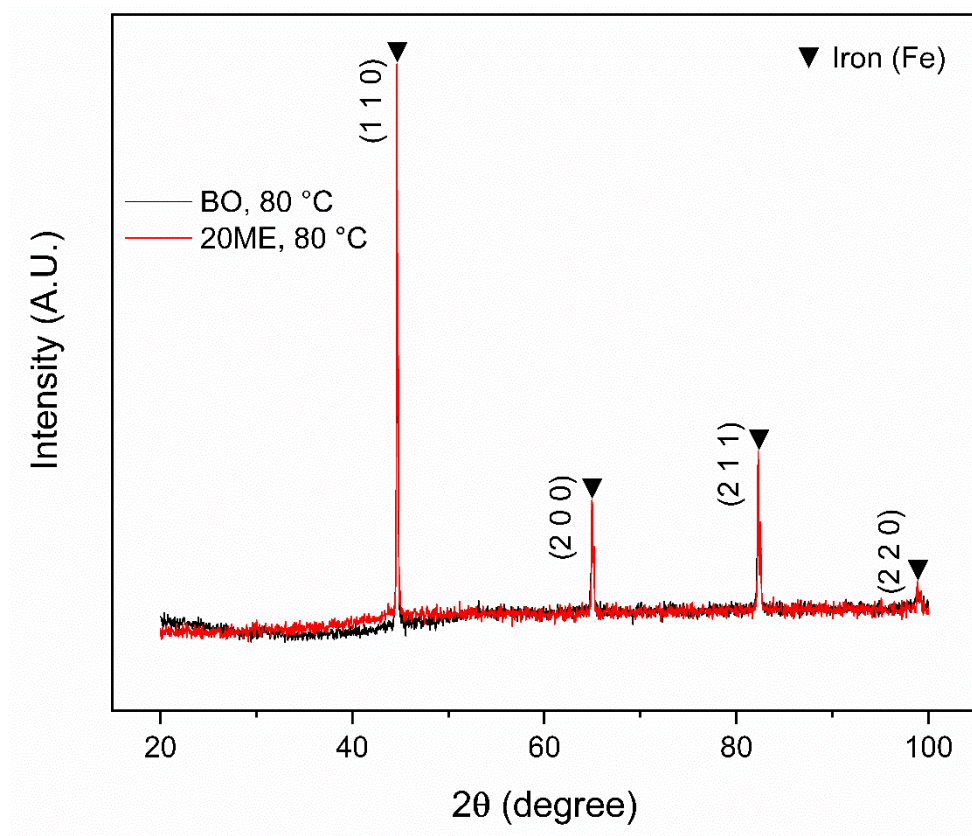
Fig. B4. XRD analysis results of CS coupons after immersion experiments in BO and BO+20wt% ME (20ME) at 80 °C for 24h.
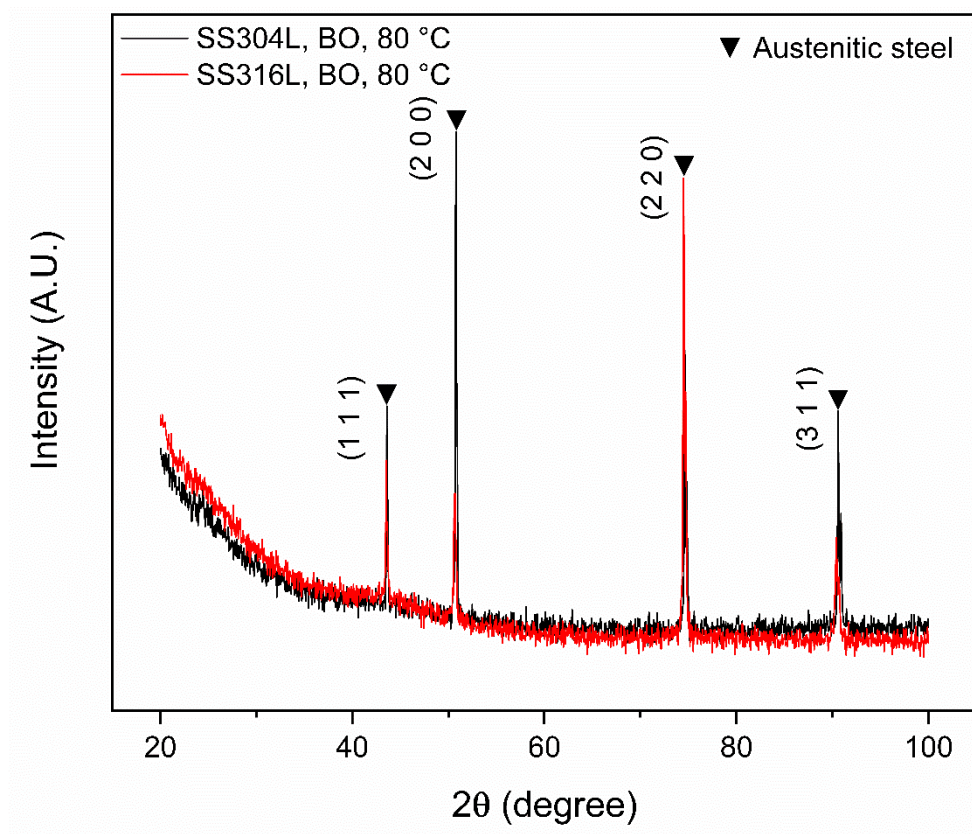
Fig. B5. XRD analysis results of SS 304L and SS 316L coupons after immersion experiments in BO at 80 °C for 24h.

Table B1. Summary of corrosion rate data for CS and SS in BO and BO/ME mixtures at 50 and 80 °C immersed for 24h.

ME wt%	CS corrosion rate (mm/y)		SS 304L corrosion rate (mm/y)		SS 316L corrosion rate (mm/y)	
	50 ºC	80 ºC	50 ºC	80 ºC	50 ºC	80 ºC
0	1.509	7.208	nil	0.781	nil	0.077
5	1.648	7.940	nil	0.543	nil	0.005
10	1.852	8.094	nil	0.432	nil	0.002
15	1.934	7.653	nil	0.178	nil	0.001
20	2.027	6.794	nil	0.002	nil	0.000

Table B2. TGA data for BO.

Temperature (ºC)	TG (wt%)	Temperature (ºC)	TG (wt%)	Temperature (ºC)	TG (wt%)	Temperature (ºC)	TG (wt%)
30.0	100.0	209.2	48.5	387.6	21.8	573.3	15.7
35.3	99.2	214.6	47.2	398.8	21.0	578.8	15.6
40.8	98.1	220.1	45.9	404.6	20.7	590.1	15.5
46.3	96.9	225.3	44.6	410.4	20.4	595.5	15.4
51.8	95.5	230.8	43.3	416.0	20.1	601.1	15.3
57.4	93.9	236.2	42.1	421.6	19.8	606.6	15.3
62.9	92.2	241.6	40.9	427.4	19.5	612.3	15.2
68.5	90.5	247.0	39.7	433.1	19.2	618.1	15.2
74.2	88.7	252.4	38.5	438.7	19.0	623.7	15.1
79.7	86.7	257.9	37.4	444.3	18.8	629.3	15.0
85.3	84.8	263.4	36.3	450.0	18.6	634.9	15.0
90.8	82.9	268.9	35.3	455.7	18.4	640.6	14.9
96.2	81.0	274.5	34.3	461.4	18.2	645.9	14.9
101.5	79.1	280.2	33.3	467.1	18.0	651.2	14.8
106.8	77.3	285.7	32.4	472.7	17.9	656.4	14.8
112.2	75.5	291.5	31.6	478.3	17.7	661.6	14.7
117.6	73.8	297.1	30.8	483.9	17.6	666.8	14.7
123.0	72.1	302.8	30.0	489.5	17.4	672.2	14.6
128.4	70.4	308.5	29.2	495.2	17.3	677.6	14.6
133.9	68.9	314.1	28.5	500.8	17.1	682.6	14.6
139.3	67.3	320.0	27.8	506.5	17.0	687.9	14.5
144.7	65.8	325.6	27.2	512.2	16.9	693.3	14.5
150.2	64.2	331.3	26.6	518.0	16.7	699.0	14.4
155.6	62.7	337.0	26.0	523.7	16.6	705.0	14.4
160.9	61.3	342.7	25.4	529.4	16.5	710.7	14.3
166.2	59.8	348.4	24.9	535.1	16.4	716.7	14.3
171.5	58.4	354.2	24.4	540.7	16.3	722.5	14.3
177.0	56.9	359.9	23.9	546.3	16.2	728.5	14.2
182.4	55.5	365.2	23.5	551.9	16.1	734.6	14.2
187.7	54.1	370.8	23.0	557.5	16.0	740.8	14.1
193.0	52.6	376.2	22.6	563.0	15.8	746.7	14.1
198.4	51.2	382.0	22.2	567.6	15.8	750.0	14.0

Appendix C. Electrochemical Measurements

Table C1. PDP data for CS in BO at 20 °C.

Current density (A/cm^2)	Potential (V)	Current density (A/cm^2)	Potential (V)	Current density (A/cm^2)	Potential (V)	Current density (A/cm^2)	Potential (V)
4.87E-05	-0.586	2.08E-05	-0.511	1.95E-06	-0.435	3.20E-05	-0.359
4.63E-05	-0.585	2.03E-05	-0.509	1.35E-06	-0.432	3.32E-05	-0.357
4.51E-05	-0.582	1.98E-05	-0.507	7.49E-07	-0.431	3.45E-05	-0.355
4.41E-05	-0.581	1.93E-05	-0.505	9.22E-08	-0.428	3.57E-05	-0.353
4.31E-05	-0.578	1.88E-05	-0.502	4.99E-07	-0.427	3.69E-05	-0.351
4.21E-05	-0.577	1.83E-05	-0.501	1.24E-06	-0.424	3.81E-05	-0.348
4.13E-05	-0.574	1.78E-05	-0.499	1.87E-06	-0.423	3.94E-05	-0.347
4.04E-05	-0.573	1.73E-05	-0.497	2.58E-06	-0.421	4.06E-05	-0.344
3.96E-05	-0.570	1.68E-05	-0.495	3.28E-06	-0.419	4.18E-05	-0.343
3.88E-05	-0.569	1.63E-05	-0.493	3.99E-06	-0.417	4.31E-05	-0.340
3.81E-05	-0.566	1.59E-05	-0.491	4.73E-06	-0.415	4.43E-05	-0.339
3.73E-05	-0.565	1.54E-05	-0.489	5.48E-06	-0.413	4.55E-05	-0.336
3.66E-05	-0.563	1.49E-05	-0.487	6.29E-06	-0.411	4.68E-05	-0.335
3.58E-05	-0.561	1.44E-05	-0.485	7.06E-06	-0.409	4.80E-05	-0.332
3.51E-05	-0.559	1.40E-05	-0.482	7.87E-06	-0.406	4.92E-05	-0.331
3.44E-05	-0.557	1.35E-05	-0.481	8.75E-06	-0.405	5.05E-05	-0.328
3.37E-05	-0.555	1.30E-05	-0.478	9.57E-06	-0.402	5.17E-05	-0.327
3.30E-05	-0.552	1.26E-05	-0.477	1.05E-05	-0.401	5.29E-05	-0.325
3.24E-05	-0.551	1.21E-05	-0.474	1.14E-05	-0.398	5.42E-05	-0.323
3.18E-05	-0.549	1.16E-05	-0.473	1.22E-05	-0.397	5.54E-05	-0.321
3.11E-05	-0.547	1.12E-05	-0.470	1.31E-05	-0.394	5.66E-05	-0.319
3.04E-05	-0.544	1.07E-05	-0.469	1.40E-05	-0.393	5.78E-05	-0.317
2.98E-05	-0.543	1.02E-05	-0.467	1.50E-05	-0.390	5.91E-05	-0.314
2.92E-05	-0.540	9.74E-06	-0.465	1.59E-05	-0.389	6.03E-05	-0.313
2.86E-05	-0.539	9.28E-06	-0.463	1.68E-05	-0.387	6.15E-05	-0.311
2.80E-05	-0.536	8.81E-06	-0.461	1.78E-05	-0.385	6.27E-05	-0.309
2.74E-05	-0.535	8.33E-06	-0.459	1.87E-05	-0.383	6.39E-05	-0.306
2.68E-05	-0.532	7.82E-06	-0.457	1.98E-05	-0.381	6.51E-05	-0.305
2.62E-05	-0.531	7.34E-06	-0.455	2.08E-05	-0.378	6.63E-05	-0.303
2.57E-05	-0.528	6.85E-06	-0.453	2.18E-05	-0.377	6.75E-05	-0.301
2.51E-05	-0.527	6.33E-06	-0.451	2.29E-05	-0.374	6.87E-05	-0.298
2.45E-05	-0.524	5.82E-06	-0.449	2.40E-05	-0.373	6.99E-05	-0.297
2.40E-05	-0.523	5.32E-06	-0.447	2.51E-05	-0.371	7.11E-05	-0.294
2.34E-05	-0.520	4.79E-06	-0.444	2.62E-05	-0.369	7.23E-05	-0.293
2.29E-05	-0.519	4.24E-06	-0.443	2.74E-05	-0.367	7.35E-05	-0.290
2.23E-05	-0.517	3.66E-06	-0.440	2.85E-05	-0.365	7.47E-05	-0.289
2.18E-05	-0.515	3.08E-06	-0.439	2.97E-05	-0.363	7.50E-05	-0.288
2.13E-05	-0.513	2.54E-06	-0.436	3.08E-05	-0.361	7.53E-05	-0.288

Table C2: Bode plot data for CS in BO at 20 °C after 11h.

Freq. (HZ)	|Z|_msd (ohm cm^2)	|Z|_cal (ohm cm^2)	Angle_msd (degree)	Angle_cal (degree)	Freq. (HZ)	|Z|_msd (ohm cm^2)	|Z|_cal (ohm cm^2)	Angle_msd (degree)	Angle_cal (degree)
1000.0	2088	2092	1.10	0.26	8.9	2310	2309	10.46	10.45
891.3	2092	2092	1.09	0.29	7.9	2337	2338	11.26	11.24
794.3	2092	2093	1.10	0.32	7.1	2368	2370	12.08	12.05
707.9	2092	2093	1.05	0.35	6.3	2411	2407	12.88	12.89
631.0	2091	2093	0.93	0.39	5.6	2448	2448	13.72	13.74
562.3	2096	2094	0.92	0.42	5.0	2494	2495	14.54	14.60
501.2	2099	2094	0.99	0.46	4.5	2546	2547	15.41	15.46
446.7	2096	2095	0.89	0.51	4.0	2606	2605	16.23	16.29
398.1	2099	2095	1.07	0.56	3.5	2667	2669	17.01	17.10
354.8	2106	2096	1.06	0.61	3.2	2740	2740	17.85	17.86
316.2	2087	2097	1.15	0.67	2.8	2817	2819	18.51	18.57
281.8	2095	2097	0.98	0.74	2.5	2903	2904	19.17	19.19
251.2	2102	2098	1.06	0.81	2.2	2991	2997	19.71	19.73
223.9	2104	2099	1.10	0.89	2.0	3090	3097	20.14	20.17
199.5	2103	2100	1.20	0.98	1.8	3200	3203	20.52	20.49
177.8	2099	2102	1.44	1.07	1.6	3314	3316	20.72	20.70
158.5	2107	2103	1.43	1.18	1.4	3432	3434	20.87	20.77
141.3	2110	2104	1.33	1.29	1.3	3558	3556	20.79	20.71
125.9	2104	2106	1.47	1.42	1.1	3685	3682	20.64	20.53
112.2	2112	2108	1.59	1.56	1.0	3817	3810	20.24	20.21
100.0	2111	2110	1.96	1.71	0.9	3932	3938	19.83	19.78
89.1	2125	2112	1.80	1.87	0.8	4062	4066	19.25	19.23
79.4	2118	2115	2.10	2.05	0.7	4192	4192	18.66	18.59
70.8	2104	2117	2.15	2.25	0.6	4318	4315	17.82	17.86
63.1	2074	2120	2.30	2.46	0.6	4438	4432	17.01	17.07
56.2	2138	2124	2.80	2.70	0.5	4550	4544	16.14	16.21
50.1	2149	2128	3.20	2.95	0.4	4654	4650	15.19	15.32
44.7	2139	2132	3.69	3.23	0.4	4746	4748	14.25	14.40
39.8	2140	2137	3.54	3.53	0.4	4828	4838	13.32	13.46
35.5	2141	2143	4.13	3.86	0.3	4910	4921	12.33	12.53
31.6	2140	2149	4.25	4.22	0.3	4982	4995	11.43	11.61
28.2	2151	2157	4.60	4.61	0.3	5042	5060	10.52	10.70
25.1	2166	2165	4.70	5.02	0.2	5115	5118	9.78	9.83
22.4	2173	2174	5.66	5.48	0.2	5167	5168	8.93	8.99
20.0	2185	2184	6.00	5.97	0.2	5210	5211	8.14	8.20
17.8	2188	2196	6.26	6.49	0.2	5247	5248	7.45	7.46
15.8	2204	2209	7.02	7.06	0.1	5286	5278	6.78	6.77
14.1	2221	2225	7.68	7.66	0.1	5323	5304	6.14	6.13
12.6	2243	2242	8.18	8.30	0.1	5352	5325	5.61	5.55
11.2	2259	2262	8.90	8.98	0.1	5368	5342	5.02	5.03
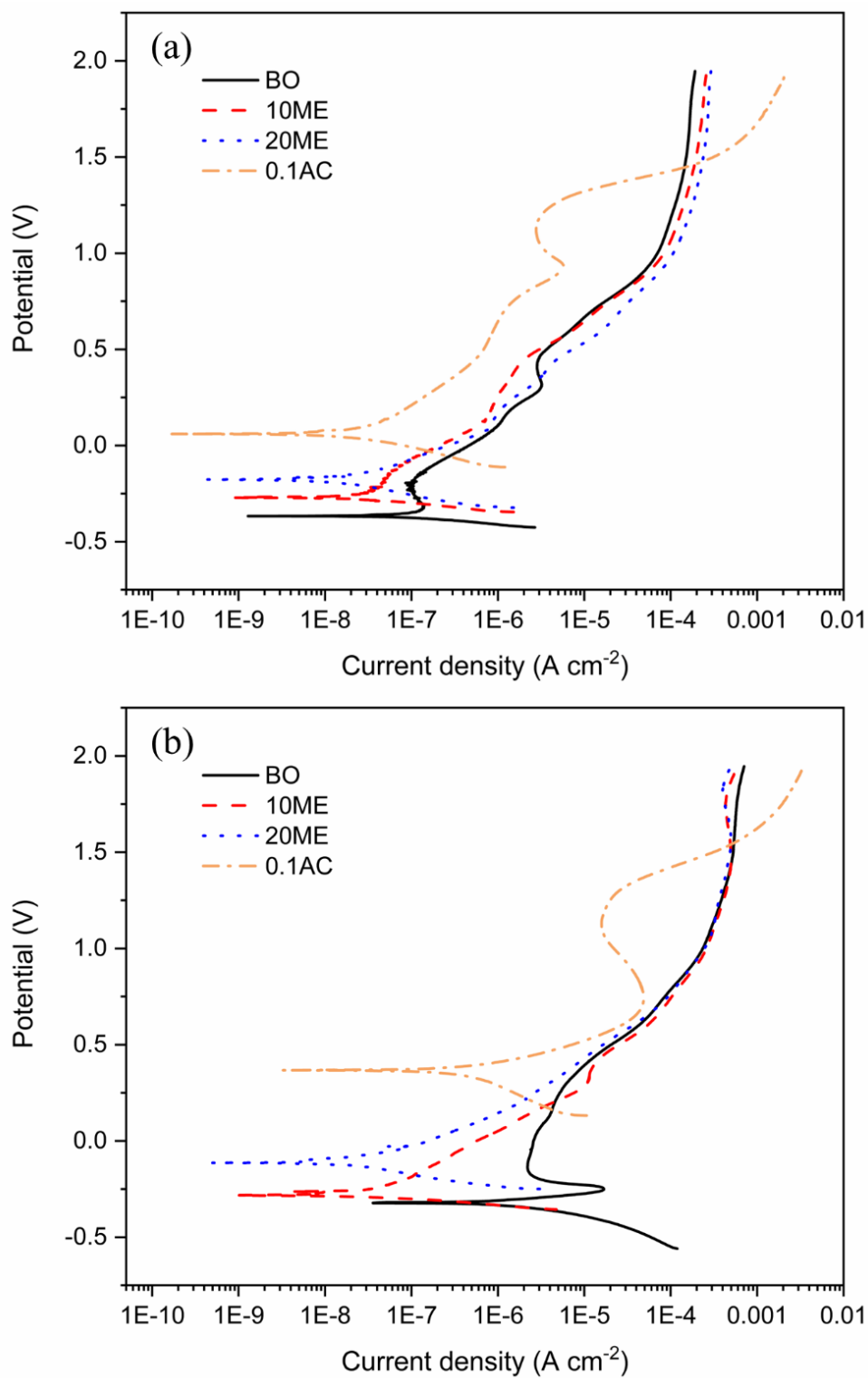
Fig. C1. PDP curves for SS 304L in BO, 10ME, 20ME, and 0.1AC environments at: (a) 20 ºC; and (b) 50 ºC.
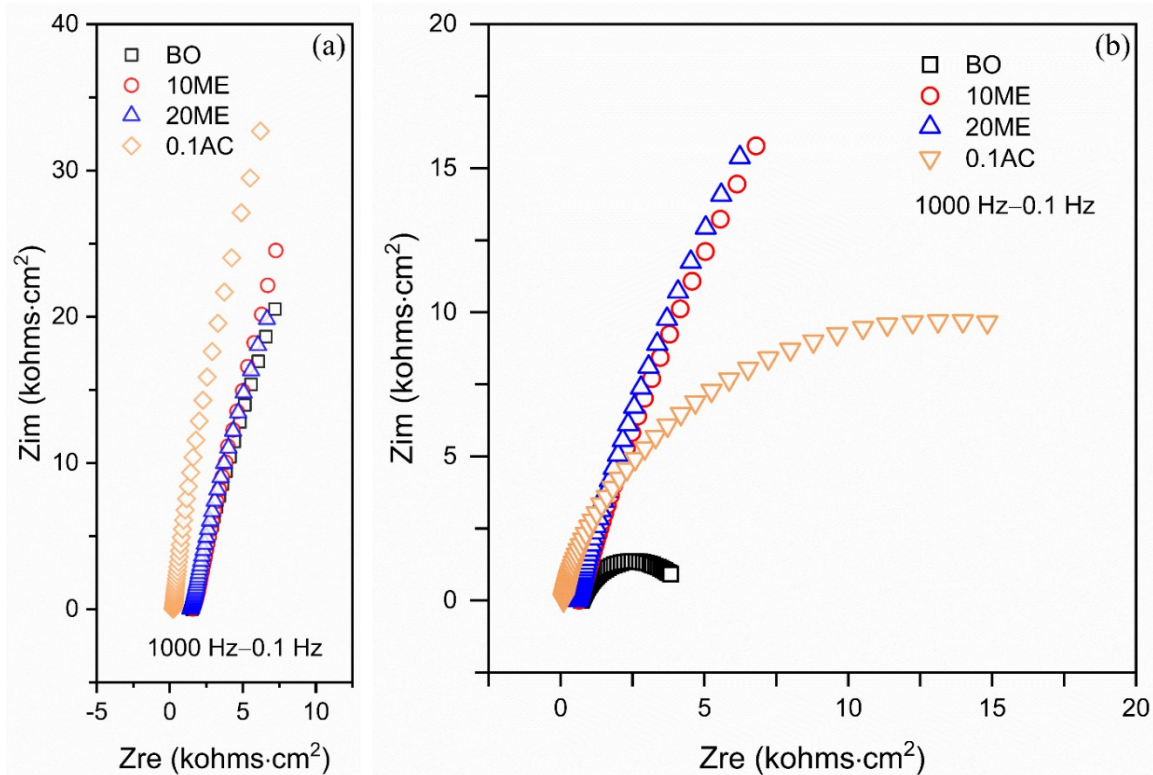
Fig. C2. Nyquist plots for SS 304L in BO, 10ME, 20ME, and 0.1 AC Environments after 11 h: (a) at 20 ºC; and (b) at 50 ºC.
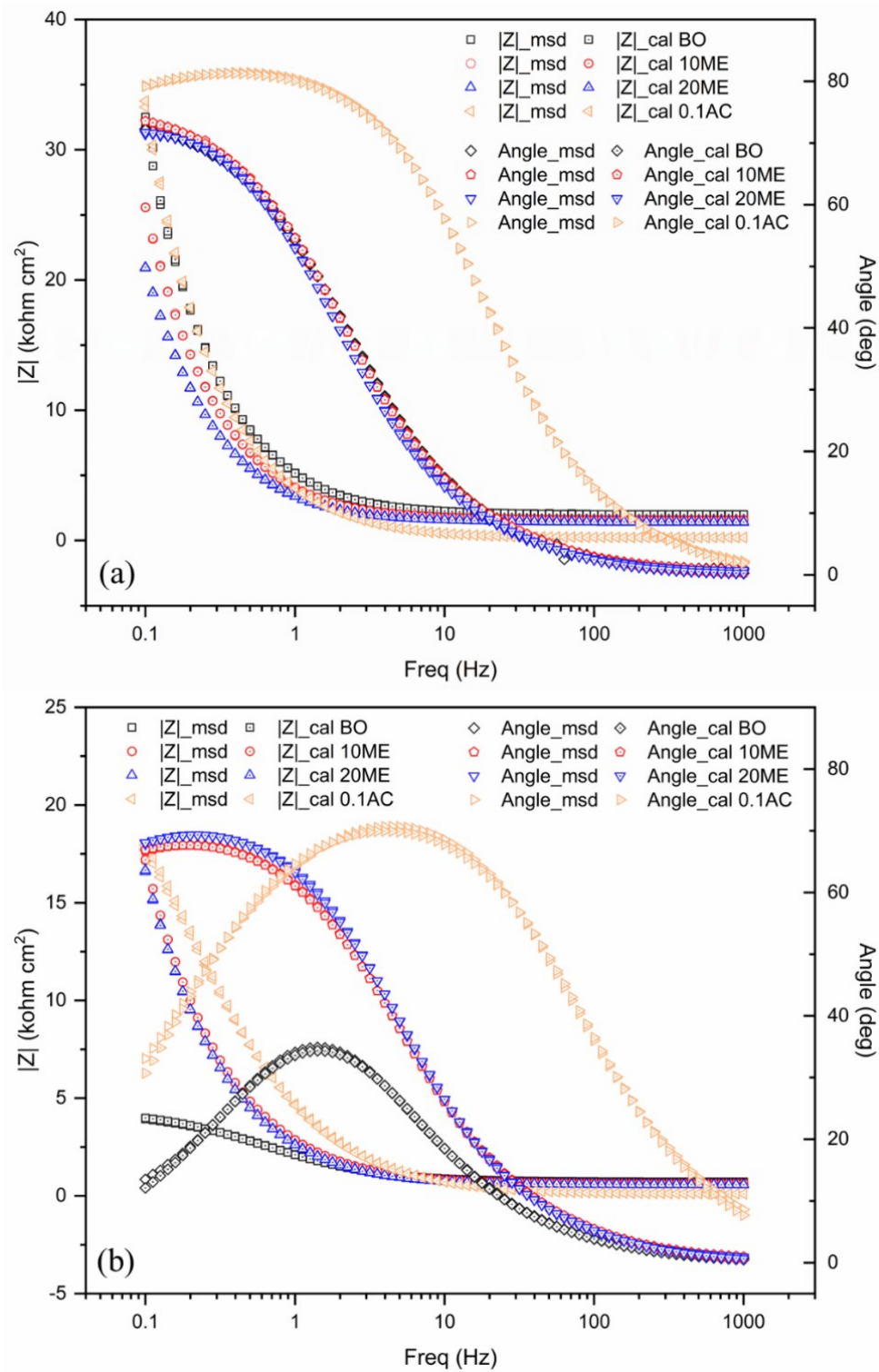
Fig. C3. Bode plots for SS 304L after 11 h: (a) at 20 ºC; and (b) at 50 ºC. The ECM used for fitting the EIS data is $R_s(CR_f(QR_{ct}))$.
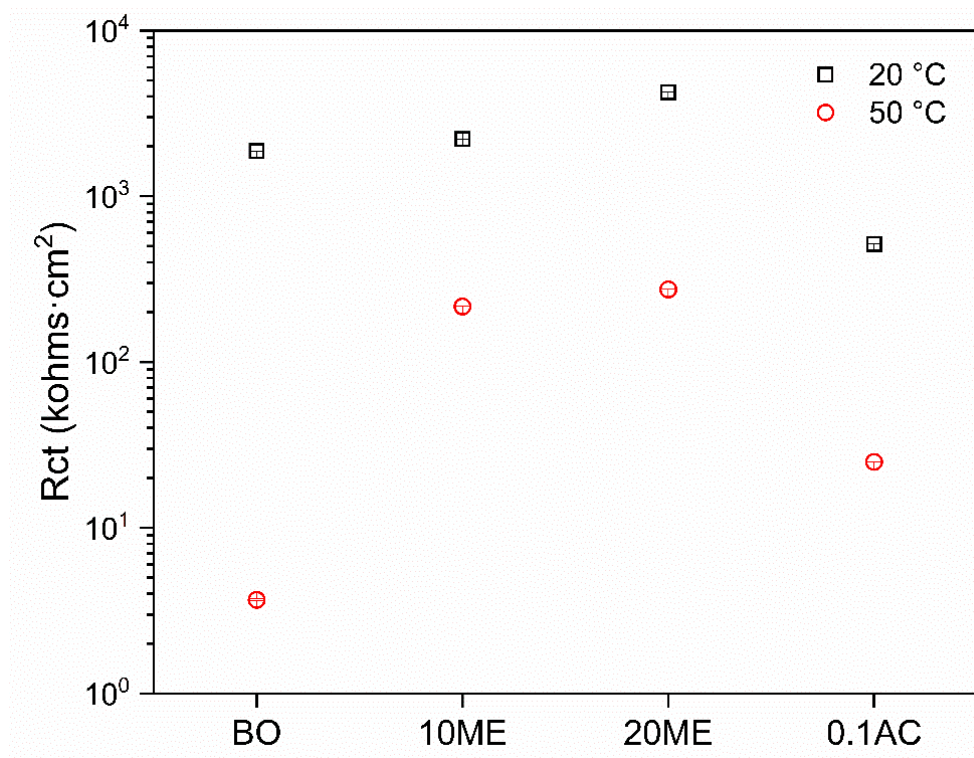
Fig. C4. A summary of R_{ct} values for SS 304L at 20 and 50 ºC obtained from EIS fittings.
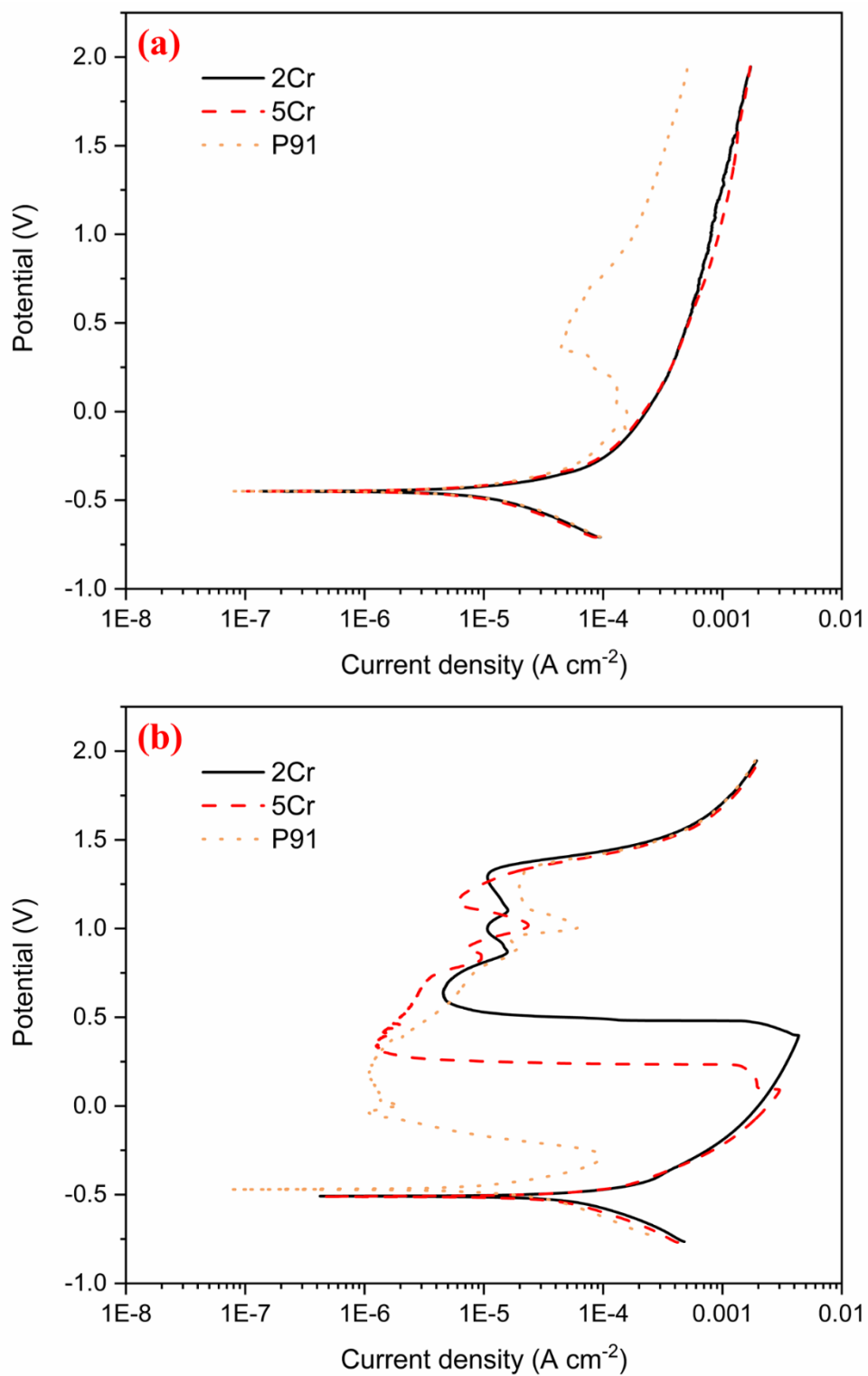
Fig. C5. PDP curves for 2Cr, 5Cr, and P91 steels at 20 °C: (a) in BO; and (b) in 0.1AC.
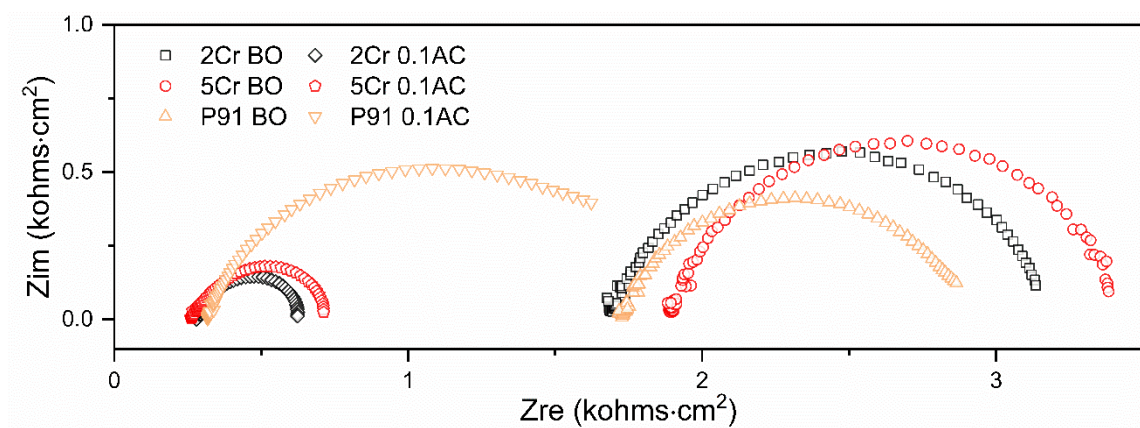
Fig. C6. Nyquist plots for 2Cr, 5Cr, and P91 steels at 20 °C after 11h.

163

Appendix D. Bio-oil (BO)/Vacuum Gas Oil (VGO) Emulsions

1:4:0.1SP

(a)	(b)	(c)
0 min	40 min	120 min

1:4:0.1SP:0.1ME

(d)	(e)	(f)
0 min	70 min	120 min
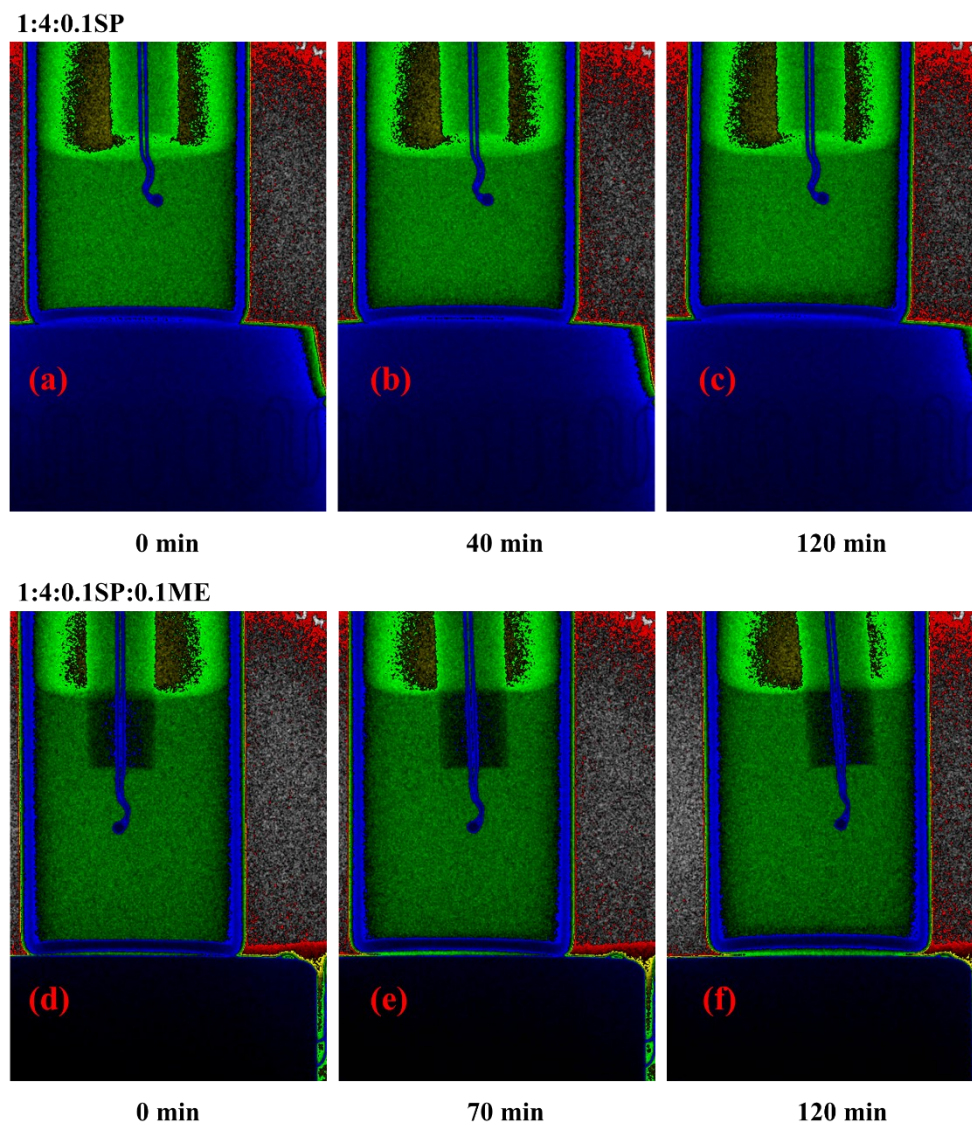
Fig. D1. X-ray images of 1:4:0.1SP emulsion at 50 °C: (a) just made; (b) starting phase separation at 40 min; and (c) after 120 min. X-ray images of 1:4:0.1SP:0.1ME emulsion at 50 °C: (d) just made; (e) starting phase separation at 70 min; and (f) after 120 min.
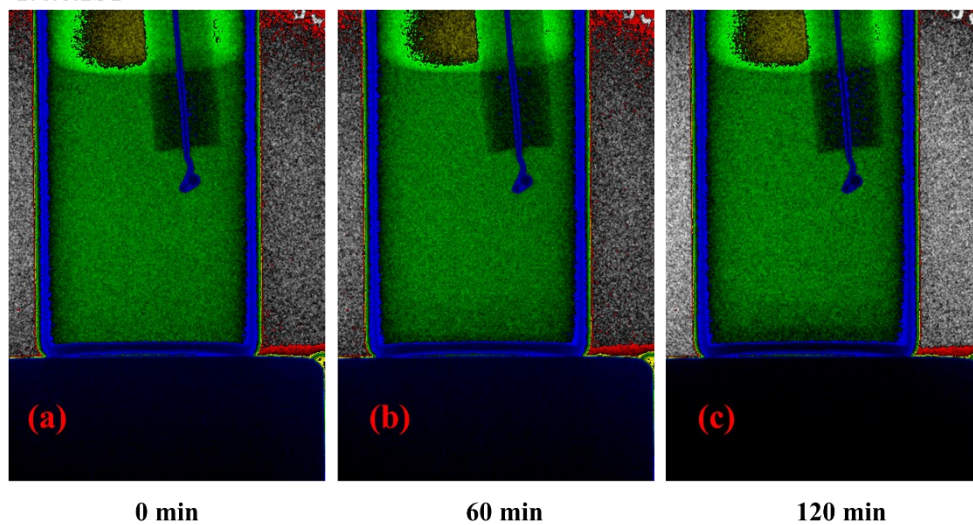
Fig. D2. X-ray images of 1:4:0.1ST emulsion at 50 °C: (a) just made; (b) starting phase separation at 60 min; and (c) after 120 min.

1:4:0.1TW

(a) 0 min (b) 20 min (c) 120 min

1:4:0.1TW:0.1ME

(d) 0 min (e) 40 min (f) 120 min
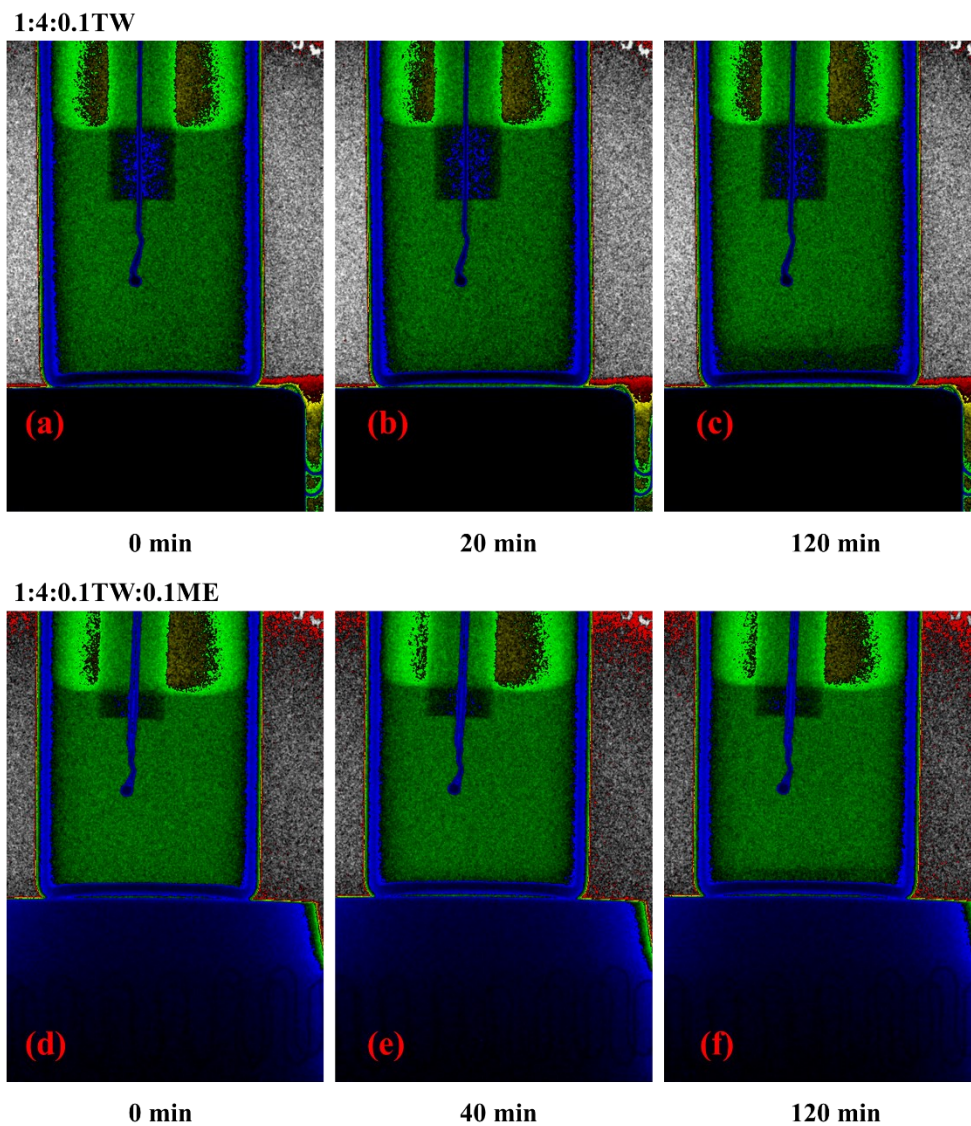
Fig. D3. X-ray images of 1:4:0.1TW emulsion at 50 °C: (a) just made; (b) starting phase separation at 20 min; and (c) after 120 min. X-ray images of 1:4:0.1TW:0.1ME emulsion at 50 °C: (d) just made; (e) starting phase separation at 40 min; and (f) after 120 min.

Table D1. FTIR data for vacuum gas oil (VGO).

Wave # (cm⁻¹)	Absorbance	Wave # (cm⁻¹)	Absorbance	Wave # (cm⁻¹)	Absorbance	Wave # (cm⁻¹)	Absorbance
644	0.000	1473	0.076	2341	-0.001	3190	-0.004
663	0.000	1493	0.019	2360	-0.001	3209	-0.003
683	0.008	1512	0.008	2380	-0.004	3228	-0.004
702	0.011	1531	0.003	2399	-0.005	3248	-0.002
721	0.037	1551	0.002	2418	-0.004	3267	-0.002
741	0.028	1570	0.006	2438	-0.006	3286	-0.001
760	0.026	1589	0.011	2457	-0.006	3305	-0.004
779	0.018	1608	0.013	2476	-0.007	3325	-0.001
798	0.021	1628	0.005	2495	-0.007	3344	-0.003
818	0.027	1647	0.001	2515	-0.008	3363	-0.002
837	0.014	1666	0.000	2534	-0.006	3383	0.000
856	0.013	1686	-0.001	2553	-0.006	3402	-0.005
876	0.017	1705	-0.002	2573	-0.005	3421	-0.006
895	0.007	1724	-0.003	2592	-0.005	3440	-0.001
914	0.004	1743	-0.003	2611	-0.004	3460	-0.005
933	0.006	1763	-0.003	2630	-0.002	3479	-0.003
953	0.007	1782	-0.004	2650	-0.003	3498	-0.004
972	0.007	1801	-0.005	2669	-0.001	3518	-0.008
991	0.007	1821	-0.004	2688	-0.004	3537	-0.005
1011	0.007	1840	-0.003	2708	-0.003	3556	-0.007
1030	0.012	1859	-0.004	2727	0.001	3575	-0.006
1049	0.007	1878	-0.004	2746	-0.001	3595	-0.005
1068	0.010	1898	-0.002	2765	0.001	3614	-0.006
1088	0.006	1917	-0.003	2785	0.005	3633	-0.004
1107	0.005	1936	-0.003	2804	0.019	3653	-0.008
1126	0.007	1955	-0.004	2823	0.057	3672	-0.006
1146	0.009	1975	-0.004	2843	0.262	3691	-0.005
1165	0.009	1994	-0.005	2862	0.378	3710	-0.003
1184	0.008	2013	-0.005	2881	0.261	3730	-0.005
1203	0.009	2033	-0.004	2900	0.414	3749	-0.006
1223	0.008	2052	-0.004	2920	0.725	3768	-0.008
1242	0.010	2071	-0.005	2939	0.519	3788	-0.004
1261	0.012	2090	-0.003	2958	0.446	3807	-0.004
1281	0.013	2110	-0.004	2978	0.136	3826	-0.004
1300	0.020	2129	-0.004	2997	0.044	3845	-0.003
1319	0.020	2148	-0.004	3016	0.033	3865	-0.002
1338	0.024	2168	-0.004	3035	0.025	3884	-0.004
1358	0.027	2187	-0.005	3055	0.022	3903	-0.002
1377	0.098	2206	-0.003	3074	0.009	3923	-0.004
1396	0.019	2225	-0.003	3093	0.003	3942	-0.006
1416	0.024	2245	-0.002	3113	-0.002	3961	-0.006
1435	0.080	2264	-0.002	3132	-0.002	3980	-0.001
1454	0.179	2283	-0.003	3151	-0.001	4000	0.000

Table D2. TGA data for VGO.

Temperature (ºC)	TG (wt%)	Temperature (ºC)	TG (wt%)	Temperature (ºC)	TG (wt%)	Temperature (ºC)	TG (wt%)
29.9	100.0	230.1	78.5	405.6	0.3	580.8	0.3
36.7	100.0	234.3	76.1	409.8	0.3	585.0	0.3
42.7	100.0	238.5	73.5	413.9	0.3	589.2	0.3
48.4	100.1	242.7	70.8	418.1	0.3	593.3	0.3
53.8	100.1	246.9	68.0	422.2	0.3	597.5	0.3
59.2	100.1	251.1	65.1	426.4	0.3	601.7	0.3
64.7	100.2	255.2	62.2	430.6	0.3	605.9	0.3
70.1	100.2	259.5	59.1	434.8	0.3	610.0	0.3
75.4	100.2	263.6	56.0	438.9	0.3	614.2	0.3
80.6	100.2	267.8	52.8	443.1	0.3	618.3	0.3
85.7	100.2	272.1	49.7	447.3	0.3	622.5	0.3
90.9	100.2	276.2	46.5	451.4	0.3	626.6	0.3
96.0	100.2	280.5	43.4	455.6	0.3	630.8	0.3
100.9	100.1	284.5	40.3	459.9	0.3	635.0	0.3
105.9	100.1	288.7	37.2	464.0	0.3	639.1	0.3
110.7	100.0	292.9	34.2	468.2	0.3	643.2	0.3
115.6	100.0	297.1	31.3	472.4	0.3	647.4	0.3
120.3	99.9	301.2	28.5	476.6	0.3	651.6	0.3
125.1	99.8	305.4	25.8	480.7	0.3	655.8	0.3
129.7	99.7	309.6	23.2	484.9	0.3	660.0	0.3
134.3	99.6	313.8	20.7	489.0	0.3	664.2	0.3
139.0	99.4	317.9	18.4	493.2	0.3	668.4	0.3
143.6	99.2	322.1	16.3	497.3	0.3	672.6	0.3
148.0	99.0	326.2	14.2	501.5	0.3	676.7	0.3
152.6	98.8	330.4	12.4	505.8	0.3	680.9	0.3
157.1	98.5	334.6	10.6	509.9	0.3	685.1	0.3
161.5	98.1	338.8	8.9	514.0	0.3	689.2	0.3
166.0	97.7	343.0	7.5	518.2	0.3	693.3	0.3
170.3	97.2	347.1	6.1	522.3	0.3	697.5	0.3
174.7	96.7	351.3	4.8	526.5	0.3	701.6	0.3
179.0	96.0	355.5	3.7	530.7	0.3	705.8	0.3
183.3	95.3	359.7	2.7	534.8	0.3	710.0	0.3
187.7	94.5	364.0	1.8	539.0	0.3	714.2	0.3
192.0	93.5	368.1	1.1	543.2	0.3	718.3	0.3
196.3	92.4	372.3	0.6	547.4	0.3	722.5	0.3
200.5	91.2	376.4	0.4	551.5	0.3	726.7	0.3
204.8	89.9	380.6	0.3	555.7	0.3	730.8	0.3
209.0	88.4	384.7	0.3	559.9	0.3	735.0	0.3
213.2	86.7	388.9	0.3	564.1	0.3	739.2	0.3
217.5	84.9	393.1	0.3	568.3	0.3	743.3	0.3
221.6	82.9	397.3	0.3	572.5	0.3	747.5	0.3
225.8	80.8	401.4	0.3	576.7	0.3	750.1	0.3

Table D3. TGA data for the BO:VGO 1:4 emulsion.

Temperature (°C)	TG (wt%)	Temperature (°C)	TG (wt%)	Temperature (°C)	TG (wt%)	Temperature (°C)	TG (wt%)
30.0	100.0	163.1	88.0	278.6	30.2	392.2	1.9
34.6	99.6	166.1	87.4	281.4	28.5	395.0	1.9
38.8	99.3	169.2	86.8	284.3	26.9	397.8	1.9
42.8	98.9	172.1	86.2	287.1	25.3	400.7	1.8
46.6	98.6	175.1	85.5	290.0	23.7	403.5	1.8
50.3	98.4	178.0	84.8	292.8	22.3	406.4	1.8
53.9	98.2	180.9	84.1	295.7	20.8	409.2	1.8
57.5	98.0	183.9	83.3	298.5	19.4	412.0	1.8
61.2	97.8	186.8	82.4	301.3	18.1	414.8	1.8
64.9	97.6	189.7	81.5	304.2	16.8	417.6	1.7
68.6	97.5	192.6	80.5	307.0	15.6	420.5	1.7
72.2	97.3	195.6	79.4	309.8	14.4	423.4	1.7
75.7	97.2	198.5	78.3	312.7	13.3	426.3	1.7
79.3	97.0	201.3	77.1	315.5	12.2	429.0	1.7
82.8	96.8	204.2	75.9	318.4	11.1	431.8	1.7
86.2	96.7	207.1	74.6	321.2	10.1	434.7	1.7
89.7	96.5	210.0	73.2	324.0	9.2	437.5	1.6
93.3	96.3	213.0	71.8	326.9	8.3	440.3	1.6
96.7	96.1	215.8	70.3	329.8	7.4	443.2	1.6
100.1	95.9	218.6	68.7	332.6	6.5	446.0	1.6
103.4	95.6	221.5	67.1	335.4	5.8	448.9	1.6
106.7	95.4	224.4	65.4	338.3	5.0	451.7	1.6
110.1	95.1	227.3	63.7	341.2	4.3	454.6	1.6
113.4	94.9	230.1	62.0	344.0	3.7	457.4	1.6
116.6	94.6	233.0	60.2	346.8	3.2	460.2	1.6
119.9	94.3	235.8	58.4	349.7	2.8	463.0	1.6
123.1	93.9	238.7	56.5	352.5	2.5	465.9	1.6
126.3	93.6	241.6	54.6	355.3	2.3	468.7	1.6
129.4	93.3	244.4	52.7	358.2	2.2	471.6	1.6
132.6	92.9	247.3	50.8	361.0	2.2	474.4	1.6
135.7	92.5	250.2	48.9	363.9	2.2	480.1	1.6
138.8	92.0	253.1	46.9	366.7	2.1	483.0	1.6
141.9	91.6	255.9	45.0	369.5	2.1	485.8	1.6
145.0	91.1	258.7	43.1	372.3	2.1	487.4	1.6
148.1	90.6	261.6	41.2	375.1	2.0	587.0	1.6
151.1	90.1	264.4	39.3	378.0	2.0	687.1	1.6
154.1	89.6	267.3	37.4	380.8	2.0	750.1	1.6
157.2	89.1	270.1	35.6	383.7	2.0	392.2	1.9
160.1	88.6	272.9	33.7	386.5	1.9	395.0	1.9